ResearchGate

See discussions, stats, and author profiles for this publication at: https://www.researchgate.net/publication/283624265

Two-Dimensional Metal-Organic Networks as a New Class of Electrocatalysts

Article · January 2015

CITATION
1

READS
2,556

1 author:

Benjamin Wurster
Max Planck Institute for Solid State Research
7 PUBLICATIONS **366** CITATIONS

SEE PROFILE

All content following this page was uploaded by Benjamin Wurster on 10 June 2016.

The user has requested enhancement of the downloaded file.

Two-Dimensional Metal-Organic Networks as a New Class of Electrocatalysts

THÈSE N^{O} 6783 (2015)

PRÉSENTÉE LE 24 SEPTEMBRE 2015

À LA FACULTÉ DES SCIENCES DE BASE
LABORATOIRE DE SCIENCE À L'ÉCHELLE NANOMÉTRIQUE
PROGRAMME DOCTORAL EN PHYSIQUE

ÉCOLE POLYTECHNIQUE FÉDÉRALE DE LAUSANNE

POUR L'OBTENTION DU GRADE DE DOCTEUR ÈS SCIENCES

PAR

Benjamin WURSTER

acceptée sur proposition du jury:

Prof. M. Q. Tran, président du jury
Prof. K. Kern, directeur de thèse
Dr P. Broekmann, rapporteur
Dr M. Lackinger, rapporteur
Prof. M. Grätzel, rapporteur

ÉCOLE POLYTECHNIQUE
FÉDÉRALE DE LAUSANNE

Suisse
2015

To Anna and Amaru

Abstract

This thesis deals with the electrocatalytic properties of two-dimensional metal-organic coordination networks (2D-MOCNs) self-assembled on electrode surfaces and catalytic activity of 2D-MOCNs is demonstrated for the first time. The low-coordinated metal centers within these supramolecular structures resemble the catalytically active sites of metallo-enzymes. The activity of the metal centers is determined by the type of the metal and the coordination environment; both parameters can be carefully adjusted in 2D-MOCNs.

In order to study and correlate electrocatalytic properties with the atomic structure of 2D-MOCNs, a scanning tunnelling microscope operating in ultra-high vacuum (UHV) was combined with an electrochemical (EC) setup. Sample preparation and scanning tunneling microscopy (STM) were conducted under UHV conditions. By STM the composition and structure of the networks were controlled and characterized prior to EC experiments. A transfer system between UHV and EC instrumentation was constructed to keep the sample at all times in a clean and controlled environment.

It is demonstrated that the mechanism of the oxygen reduction reaction (ORR) can be influenced by the type of the metal center in the network. The networks formed by benzene-tricarboxylic acid (TMA) with either Fe or Mn atoms are structurally identical, but their electrochemical signal differs significantly. Both networks catalyze the reduction of O_2 to H_2O, but on different pathways. These results emphasize the key role of the unsaturated metal centers in the electrocatalytic reduction.

The electrocatalytic response in the ORR can also altered by the distinct coordination environment; this is shown for Fe atoms nitrogen-coordinated by either tetracyanoquinodimethane (TCNQ), bis-pyridyl-bipyrimidine (PBP) or phythalocyanine (Pc). Depending on the specific coordination environment formed by the different ligands the the final product (H_2O_2 or H_2O) and the mechanism of the ORR is changed.

Abstract

In the last part of this thesis the two metal binding sites of 5,10,15,20-tetra(4-pyridyl)porphyrin (TPyP) are used to selectively incorporate different metal centers in a fixed organic environment and create homo- and hetero-bimetallic networks. The coupling of the two metals centers promoted by the organic environment modifies the electrocatalytic response. The correct combination of two metal centers in the right positioning makes an efficient catalyst. In the ORR the peak and onset potential is varied depending on the metal combination. In the case of the oxygen evolution reaction a non-linearly increased catalytic activity by the cooperative bimetallic effect is obtained.

The results presented in this thesis demonstrate the high potential of 2D-MOCNs for heterogeneous catalytic chemical conversions. Engineering of the network structure and the distinct coordination environment of the metal centers offers the possibility to tune their catalytic activity. This opens up a new route for the design of a new class of nanocatalyst materials.

Keywords: electrocatalysis, scanning tunneling microscopy, metal-organic coordination, molecular self-assembly, oxygen reduction, oxygen evolution, bimetallic

Kurzfassung

Diese Arbeit befasst sich mit elektrokatalytischen Eigenschaften von selbst-assemblierten zwei-dimensionalen metall-organischen Koordinations-Netzwerken (two-dimensional metal-organic coordination networks, 2D-MOCNs) auf Elektroden Oberflächen und katalytische Wirkung von 2D-MOCNs wird zum Ersten mal gezeigt. Die niedrig-koordinierten Metallzentren innerhalb dieser supramolekularen Strukturen gleichen den katalytisch aktiven Zentren von Metalloenzymen. Die Aktivität der Metallzentren wird durch die Art des Metalls und dessen Koordinationsumgebung bestimmt; beide Parameter können in 2D-MOCNs sorgfältig angepasst werden.

Um die elektrokatalytischen Eigenschaften zu untersuchen und sie in Beziehung mit der atomaren Struktur der 2D-MOCNs zu setzen, wurde ein Rastertunnelmikroskop im Ultrahochvakuum (UHV) mit einem elektrochemischen (EC) Aufbau kombiniert. Probenpräparation und Rastertunnelmikroskopie (scanning tunneling microscopy, STM) wurden unter UHV Bedingungen durchgeführt. Mittels STM wurden die Zusammensetzung und die Struktur der Netzwerke vor den elektrochemischen Experimenten kontrolliert und charakterisiert. Ein Transfersystem zwischen UHV und EC Bereich wurde konstruiert um die Probe jederzeit in einer sauberen und kontrolierten Umgebung zu halten.

Es wird gezeigt, dass der Mechanismus der Sauerstoffreduktionsreaktion (oxygen reduction reaction, ORR) durch die Art des Metallzentrums in den Netzwerken beeinflusst werden kann. Die von Benzoltricarbonsäure gebildeten Netzwerke mit entweder Fe oder Mn Atomen sind strukturell identisch, aber ihre elektrochemischen Signale unterscheiden sich deutlich. beide Netzwerke katalysieren die Reduktion von O_2 zu H_2O, jedoch auf unterschiedlichen Reaktionswegen. Diese Ergebnisse heben die Schlüsselrolle der niedrig-koordinierten Metallzentren in der elektrokatalytischen Reduktion hervor.

Das elektrokatalytische Verhalten in der ORR kann auch durch die Koordinationsumgebung verändert werden; dies wird für Fe Atomen, die entweder von Tetracyanochinodimethan (TCNQ), Bis-pyridyl-bipyrimidin (PBP) oder Phythalocyanin (Pc)

koordinert werden, gezeigt. Abhängig von den verschiedenen Koordinationsumgebungen der verschiedenen Liganden ändert sich das Endprodukt (H_2O_2 oder H_2O) und der Mechanismus der ORR.

Im letzten Teil dieser Arbeit werden die zwei Metallbindungsstellen von 5,10,15,20-tetra(4-pyridyl)porphyrin (TPyP) benutzt um selektiv verschiedene Metallzentren in einer vorgegeben organischen Umgebung einzubinden und homo- und hetero-bimetallische Netzwerke zu erstellen. Die Wechselwirkung beider Metallzentren über die organische Umgebung modifiziert das elektrokatalytische Verhalten. Die korrekte Kombination zweier Metallzentren in der richtigen Positionierung ergibt einen effizienten Katalysator. In der ORR verändert sich das Peak- und Anfangspotential je nach Metallkombination. Im Falle der Sauerstoffentwicklungsreaktion wird eine nichtlineare Erhöhung der katalytischen Wirkung durch den kooperativen bimetallischen Effekt erzielt

Die in dieser Arbeit präsentierten Ergebnisse zeigen das hohe Potential von 2D-MOCNs für heterogene katalytische chemische Konversionen. Anpassen der Netwerkstruktur und der Koordinationsumgebung der Metallzentren bietet die Möglichkeit ihre katalytische Wirkung einzustellen. Dies eröffnet einen neuen Weg für die Entwicklung einer neuen Klasse von nanokatalytischen Materialen.

Schlüsselwörter: Elektrokatalyse, Rastertunnelmikroskopie, Metal-organisch Koordination, molekulare Selbstassemblierung, Sauerstoff Reduktion, Sauerstoff Entwicklung, bimetallisch

Abbreviations

BDA	Biphenyl-4,4'-dicarboxylic acid
CE	Counter Electrode
CV	Cyclic Voltammogram
DOS	Density Of States
EC	Electrochemical
EDL	Electrical Double Layer
HOMO	Highest Occupied Molecular Orbital
IHP	Inner Helmholtz Plane
LDOS	Local Density Of States
LUMO	Lowest Unoccupied Molecular Orbital
MOCN	Metal-Organic Coordination Network
MOF	Metal-Organic Framework
MPc	Metallo-phthalocyanine (M = Fe, Co, Ni, Cu)
MTPP	Metallo-tetraphenylporphyrin (M = Co, Ni)
MTPyP	Metallo-tetra(4-pyridyl)porphyrin (M = Fe, Co, Cu)
OER	Oxygen Evolution Reaction
OHP	Outer Helmholtz Plane
ORR	Oxygen Reduction Reaction
PBP	5,5'-Bis(4-pyridyl)(2,2'-bipyrimidine)
RE	Reference Electrode
STM	Scanning Tunneling Microscopy
STS	Scanning Tunnelling Spectroscopy
TCNQ	7,7,8,8-tetracyanoquinodimethane
TMA	Benzene-1,3,5-tricarboxylic acid
UHV	Ultra-High Vacuum
WE	Working Electrode

Contents

Introduction

The growing worldwide demand for energy and climate change became one of the most important challenges attracting the common interest of science, engineering and society. The majority of energy generated comes from burning fossil fuels, even though it is environmentally unfriendly and there is a limited supply. Moreover the efficiency is quite low and a large amount of energy is wasted during today's standard energy conversion routes. New technologies are needed not only for energy generation, but also for energy conversion and storage. Increasing the efficiency is a major opportunity [1]. In this important field, electrochemistry provides a bridge for efficient inter-conversion of chemical to electrical energy. Fuel cells are promising candidates, since they are not Carnot Cycle limited. However, fuel cells based on the oxidation of hydrogen and reduction of oxygen need an electrocatalyst surface, since they are not simple electrode reactions and show a strong dependence on the nature of the of the electrode material [2]. In particular, the oxygen reduction reaction (ORR) limits the efficiency and to find an effective, inexpensive and stable catalyst replacing platinum is an ongoing challenge [3]. Another challenging problem is the production of hydrogen by electrochemical splitting of water; in this case, the major limitation is the large overpotential required to proceed the oxygen evolution reaction (OER) [4, 5]. The development of materials that can catalyze these electrochemical reactions is highly important and oxygen electrochemistry will play a crucial role in creating sustainable energy solutions for the future [6].

Nanotechnology allows controlled manipulation and characterization of matter at the nanometer scale (atomic, molecular, and macromolecular scale) to produces structures, devices, and systems with at least one novel/superior characteristic or property. This highly interdisciplinary field, which includes chemistry, physics, materials science and biology, attracted wide interest from both fundamental and technological points of view and promises breakthroughs in many areas like advanced

materials, sustainable energy, information technology, medicine and biotechnology. Interfaces and surfaces are highly important in this development and thus surface science play a major role. Scanning tunnelling microscopy (STM) with its unique capability to image and manipulate individual molecules and atoms [7, 8], has become a key tool in this regard. Furthermore scanning tunnelling spectroscopy (STS) allows chemical and electronic information on the atomic scale to be obtained [9,10]. The application of the STM technique has be demonstrated by a vast amount of studies comprising topology of supramolecular structures and molecular conformations [11–15], chiral specificity [16–18], pathways of chemical reactions [19–21] and catalytic functionality [22–24].

The fabrication of nanostructures on surfaces is divided into the top-down and the bottom-up conceptual approaches. Top-down fabrication comprises methods such as lithography, writing or stamping [25]. The bottom-up approach utilizes self-organized growth and self-assembly at surfaces to build up complex systems [26]. The principles applied in these processes originate from supramolecular chemistry; the chemistry beyond the single molecule that allows the construction of complex functional structures from relatively simple molecular building blocks by a hierarchical assembly scheme [27, 28]. The self-assembly of a particular system depends on the structure and the functional groups of the building blocks that influence the specific interactions between them. On surfaces, one must also consider the interaction between the molecular components and the surface, which can lead to electronic modifications on both sides of the interface. Hence, concepts from solution-based chemistry needs to be modified for the on-surface self-assembly of supramolecular nanostructures. The non-covalent intermolecular interactions in the self-assembly process comprise hydrogen bonding, metal coordination, van der Waals interactions, electrostatic forces, etc. As these intermolecular forces are, in general, weaker than covalent bonds, their benefit lies in their flexibility and reversibility. Annealing can heal structural errors to obtain thermodynamic equilibrium.

One of the most widely used strategies to build up supramolecular architectures is based on the coordination of metal atoms with organic ligands [27, 29, 30]. The concepts of coordination chemistry were developed more than a century ago [31]. Nowadays it has evolved to be a powerful tool to engineer supramolecular coordination complexes and allowed synthesis of coordination structures with extraordinary properties. Compared to hydrogen bonding, metal-ligand interactions are more rigid, selective and directional, which makes them highly important for the rational

crystal engineering in solid state chemistry. In order to mimic and understand enzymatic proteins containing transition metal complexes, a wide range of catalytic metal-organic materials have been developed and theoretically studied [32, 33]. Under these aspects the investigation of metal-organic coordination structures on surfaces is of great interest, especially for catalytic applications. Furthermore, scanning probe techniques grant direct access to structural information of coordination complexes at surfaces.

The coordination of metal atoms or clusters with organic ligands allows the synthesis of complex three-dimensional highly porous structures, called metal-organic frameworks (MOFs). The high porosity of MOFs yields large internal surface areas that facilitate their catalytic reactivity. The application of MOFs in organic catalysis has been demonstrated for a vast amount of reactions [34–36]. In recent years the application of MOFs in the electrochemical field has received growing interest; redox activity has been demonstrated for the metal and the ligand [37] and catalytic activity for hydrogen evolution [38] and oxygen reduction was observed [39]. The low intrinsic electrical conductivity of MOFs is an impediment in their application in electrochemistry. Just recently, MOFs with highly enhanced electrical conductivity has been developed [40, 41]. Charge transport can also induced by a redox hopping mechanism in metallo-porphyrin based MOFs [42]. In another study, graphene sheets acted as a conductive platform and a graphene–porphyrin MOF composite for ORR was synthesized [43]. Two-dimensional metal-organic coordination networks (2D-MOCNs), on the other hand, are directly prepared on conductive surfaces, which makes them readily accessible for electrochemical investigations. Moreover, unusual coordination configurations can also be achieved on surfaces.

2D-MOCNs consist of arrays of organic ligands coordinated with metal atoms self-assembled on surfaces and are prepared under well-controlled ultra-high vacuum (UHV) conditions. A particular and unique feature of 2D-MOCNs is the presence of low-coordinated metal centers. Due to their similarity to catalytically active sites in biological systems and classical inorganic catalyst [44,45] they are considered to have promising properties in catalysis. In metallo-enzymes, transition metal atoms are embedded in an organic matrix to catalyze important processes like water oxidation, oxygen reduction, photosynthesis and respiration [46, 47]. The active site can comprise mono- or dinuclear centers of the same or different types of metal. Functional groups of the amino acid side chains form a specific coordination environment, determining the enzymes activity towards certain reactions [48–51]. Thus, it is possible

to effectively mimic the active sites of enzymes by 2D-MOCNs. The electronic structure and the chemical properties of the metal center in the network are determined by the type of the metal and the coordination environment, which can be tuned by the number and geometry of the coordinating molecular functional groups, the electron affinity of the organic molecules, and the supporting metal surface. The organic ligands also ensure the separation of the reactive metal centers, similar to bulky protein chains that sufficiently separate the active sites, preventing site overlap and catalytic deactivation [52]. This thesis provides a proof of concept that 2D-MOCNs exhibit catalytic activity and have a high potential for heterogeneous catalytic chemical conversions.

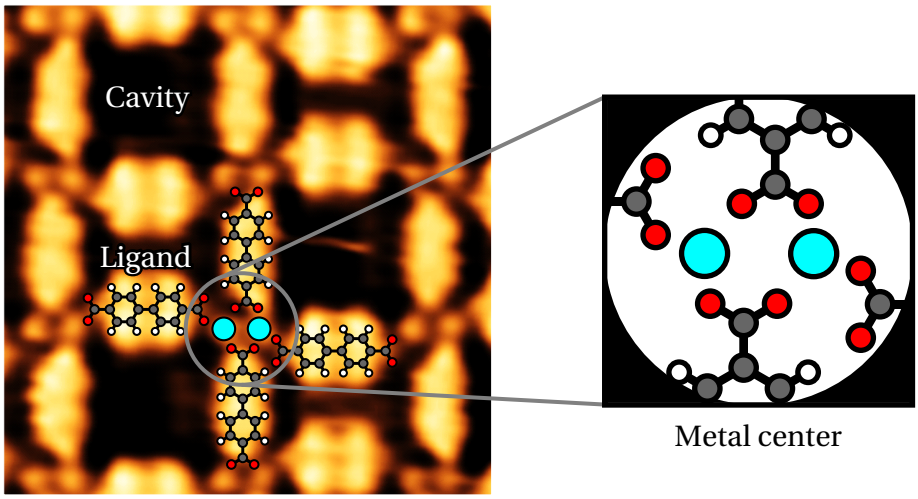

Figure 0.1: STM image of 2D-MOCN of Fe-biphenyl-dicarboxylic acid on Cu(100). The main features of 2D-MOCNs are indicated: organic ligand, metal center and cavity [53]. Zoom: coordination environment for Fe.

Figure 0.1 shows a STM image of a 2D-MOCN composed of biphenyl-4,4'-dicarboxylic acid (BDA) and iron atoms on Cu(100) as an example. The extended and periodic 2D coordination polymer is formed by the coordination of the two terminal carboxylate groups of BDA to iron dimers. The network presents open cavities where the underlying substrate is exposed. Each network node consists of two coordinatively unsaturated Fe centers with each atom being threefold coordinated to carboxylate oxygen atoms. The hybridization of the metal centers with the surface is significantly reduced due to the coordination; the electronic configurations for the Fe ions is atomic-like as found for isolated metal–organic complexes, which is in contrast to the metallic character of uncoordinated metal adatoms on surfaces [54].

A wide variety of 2D-MOCNs can be prepared; the organic ligand can be varied by changing the molecular backbone and by several functional groups (carboxylic acid, pyridyl, cyano and hydroxyl end groups), several metal centers (Mn, Fe, Co, Ni and Cu) can be used, and different noble metal substrates like Au, Ag, Cu or highly ordered pyrolytic graphite are possible [26, 55–57]. This allows engineering of the network structure with complete control of the separation and coordination geometry of the metal centers as well, as the size of the generated cavities [53, 58].

Until now the most explored application of 2D-MOCNs is the accommodation of guest molecules inside the generated cavities [15, 59]. The aim of this thesis is to explore the properties of the unique feature of MOCNs the low-coordinated metal centers by electrochemical methods and to study their electrocatalytic activities for the ORR and the OER. Initial experiments with oxygen adsorbed from the gas phase demonstrate reactivity of the metal centers and indicate the high potential of 2D-MOCNs as tailor-made heterogeneous electrocatalysts [60]. Engineering of the network structure and the specific coordination environment of the metal centers offers the possibility to design surface confined MOCNs as novel catalytic materials for applications in energy conversion and fuel production.

Most fuel cells currently use platinum or its alloys as electrocatalysts for ORR. But Pt is expensive and in limited supply. A lot of research effort is focused on replacing Pt by catalysts composed of inexpensive and earth-abundant elements. The physical and economic requirements of low-overpotential, long-term stability, pH working conditions and being non-toxic, and so impose severe boundaries on the usable material combinations.

In the field of non-precious-metal-based catalysts, nitrogen-coordinated Fe in a carbon matrix (referred to as Fe/N/C or Fe–N_x/C) attracted great interest for ORR [61]. These materials can be prepared in an inert atmosphere by high-temperature pyrolysis of either Fe–N_4 chelate complexes, or simple precursors consisting of an Fe salt, a nitrogen source (aromatic and aliphatic ligands or other nitrogen-rich small molecules) and a carbon support. In this way highly active or stable iron-based catalysts have successfully been synthesized [62, 63]. However, the structure and chemical nature of the catalytically active sites are unclear [64–66] and their determination is an ongoing process [67–69]. This uncertainty and difficulty in analyzing and controlling the exact structure of the active sites makes their further development challenging. In 2D-MOCNs coordinated transition metals are also present, but STM

allows direct access to structural information of the network; the coordination environment of the metal center is well-defined and can easily be tuned. The catalytic activities of different nitrogen-coordinated Fe-based networks are compared in this thesis, to study the effect of the distinct coordination environment formed by the varying ligands.

Another approach demonstrated recently to enhance the catalytic activity is to couple two or more metals of different types [70–75], which includes enzymes, organic catalyst such as siamese-twin porphyrins [76] or mixed porphyrins [77], core/shell nanoparticles [78], well defined bimetallic surfaces [79], etc.. The combination of two metal centers for catalytic purposes is well-known from metallo-enzymes, in which redox active metal ions are connected by bridging organic ligands with carboxylate or pyridine functionalities. The modular approach in the synthesis of 2D-MOCNs allows one to combine different metals and the preparation of bimetallic networks has been already shown [80, 81]. Thus, the electrochemical investigation of MOCNs can also contribute in the field of bimetallic catalysis. The bottom-up synthesis procedure enables positioning of redox centers in a well-defined geometric arrangement, which, especially in inorganic catalysts, is hard to achieve. The two different metal binding sites of a tetrapyridyl functionalized porphyrin are used in this thesis to create homo- and hetero-bimetallic networks. It is demontrated, that the incorporation of a second metal modifies the electrocatalytic response.

In this thesis a STM operating in UHV is combined with a suitable electrochemical (EC) setup in order to study and correlate electrocatalytic properties with the atomic structure of 2D-MOCNs. For a direct combination of UHV and EC instrumentation, an appropriate transfer system providing a clean and controlled transfer between both environments was realized. Sample preparation and STM characterization were conducted under UHV conditions. By STM the composition and structure of the networks were controlled and characterized prior to EC experiments. This thesis presents strategies to influence the catalytic activity of 2D-MOCNs by the investigation of different 2D-MOCNs. The thesis is organized as follows:

- Chapter 1 gives a brief introduction into the theoretical background of the experimental techniques. The principles of STM are described and some basic concepts and methods of electrochemistry are presented.

- In Chapter 2 the experimental setup is described and experimental details, concerning sample preparation and electrochemical experiments, are given.
- Chapter 3 comments on transfer systems for combined UHV-EC studies and discusses the transfer system realized in this thesis. The transfer between UHV and EC environment in both directions is demonstrated for a clean Au(111) surface, and STM characterization of PBP–Fe after electrochemistry is shown.
- Chapter 4 reports on the results of the TMA–Fe and TMA–Mn networks, pointing out the key role of the unsaturated metal centers and that the mechanism of the ORR can be influenced by the type of the metal center in the network.
- In Chapter 5 three different iron-based nitrogen-coordinated metal-organic structures are compared: TCNQ–Fe, PBP–Fe and FePc. The specific coordination environments of the different ligands alters the electrocatalytic response in the ORR.
- Chapter 6 uses the two metal-binding sites of TPyP to selectively incorporate different metals and create bimetallic networks. The cooperative bimetallic effect in the ORR and OER are demonstrated.

A final chapter summarizes the findings presented in this thesis and considerations for experimental improvements for future experiments are given.

Chapter 1

Theoretical and Experimental Basics

This chapter gives a brief introduction into the theoretical background of the experimental techniques employed in this thesis. Section 1.1 describes the principles of scanning tunneling microscopy. In section 1.2 some basic concepts and methods of electrochemistry are presented.

1.1 Scanning Tunneling Microscopy

STM was invented by Binning and Rohrer in 1981 [82, 83] and is the ultimate technique to investigate in real space structural and electronic properties of (semi-)conducting surfaces at the atomic scale at the air, vacuum or liquid interface. It is possible to obtain spectroscopic information (STS) [9, 10] and is a tool to manipulate matter at the single atom level [8]. Many other scanning probe techniques evolved from it later, including the atomic force microscope and scanning near field optical microscope [84–86].

STM is based on tunneling, a quantum mechanical phenomenon; it allows electrons to tunnel through an insulating barrier between two electrodes. The quantity of interest is the tunneling current I, which flows between the electrodes, when they are biased at a voltage V. The tunneling current I depends strongly on the density of states (DOS) of the electrodes, and thus carries information about the electronic structure of both electrodes.

STM takes advantage of the strong distance dependency of the tunneling current and uses a tip shaped electrode. This tip is moved in three dimensions relative to the second electrode. The working principle is sketched in Figure 1.1. The tip, usually a sharpened metallic wire, is placed a few Å above the surface of the conductive (or semi-conductive) sample. At this small distance the wavefunctions of tip and sample overlap and by applying a bias, electrons can tunnel through the gap between tip and sample. The tunneling current mainly flows through the last atoms at the very apex of the tip, because it exponentially depends on the tip-sample distance s. This leads to a high localization of the tunnel current and, consequently, to the high resolution of STM.

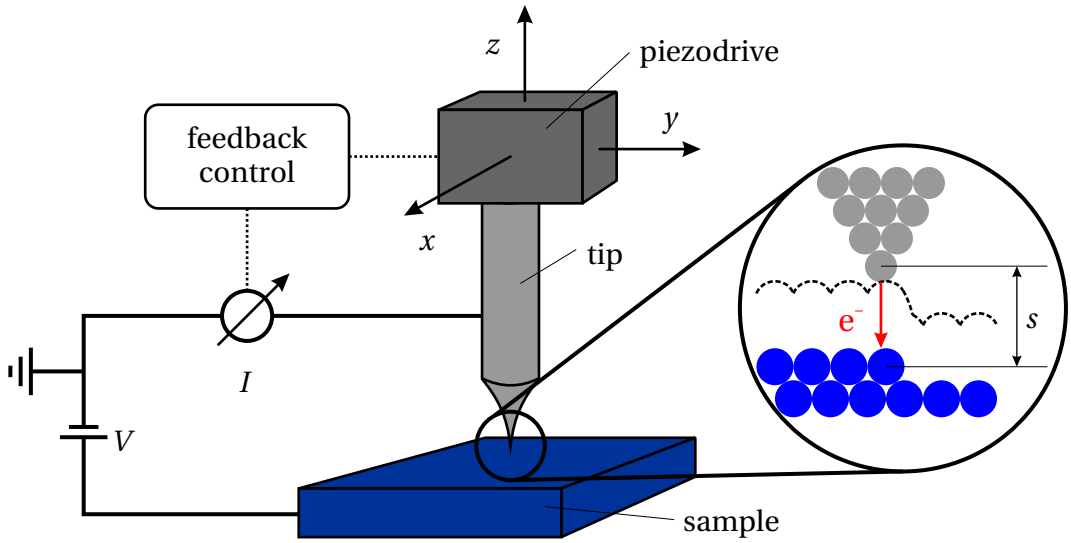

Figure 1.1: Working principle of a STM operating in constant current mode. The tip is scanned in the x-y plane above the surface and the feedback keeps the tunneling current constant by regulating the z-piezo.

The precise movement of the tip (or sample) is controlled by applying voltage signals to piezoelectric devices. During measuring the tip is scanned in the x-y plane above the surface. In the constant height mode the tunneling current I is monitored as function of the x-y-position of the tip. In the more common constant current mode, an electronic feedback readjusts the height of the tip during scanning to keep the tunneling current constant [87]. In this case the z-displacement is recorded as function of the lateral tip position. All STM images in this thesis are measured in the constant current mode.

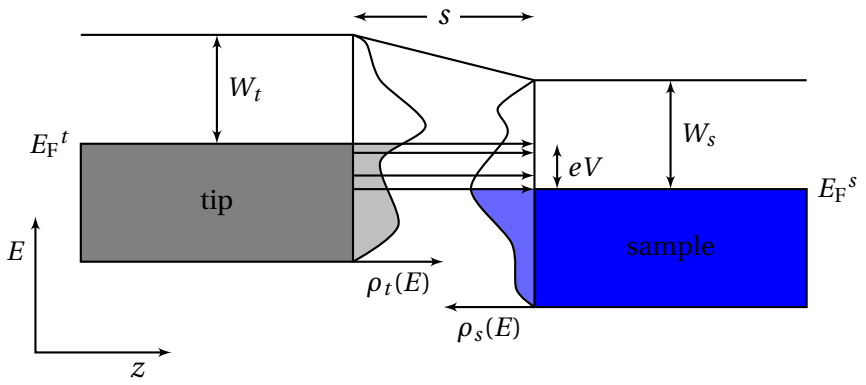

Figure 1.2: Potential energy diagram of tip and sample for a positively biased sample. Electrons tunnel from occupied states of the tip into unoccupied states of the sample.

As already mentioned, the tunneling current depends on the local density of states (LDOS) of tip and sample (ρ_t and ρ_s, respectively). With a positively biased sample electrons tunnel from occupied states of the tip to unoccupied states of the sample (Fig. 1.2). To calculate the tunneling current, the electronic structure of the tip is required, which is usually not possible to obtain. Tersoff and Hamann [88,89] assumed the tip to be a s-wavefunction and applied this approximation to Bardeen's tunneling theory [90], leading to [91,92]

$$I(V,T,x,y,s) \propto \int_{-\infty}^{\infty} \rho_s(E,x,y)\rho_t(E-eV)\tau(E,V,s)[f(E-eV,T)-f(E,T)]\mathrm{d}E, \tag{1.1}$$

with the lateral sample positions x and y, the tip-sample distance s, the Fermi distribution functions of tip and sample $f(E-eV,T)$ and $f(E,T)$ at an energy E and temperature T and the applied bias V. The tunneling transmission factor $\tau(E,V,s)$ is given by [92]

$$\tau(E,V,s) = \exp\left(-2s\sqrt{\frac{m_e}{\hbar^2}}\sqrt{W_s+W_t-2E+eV}\right), \tag{1.2}$$

with the electron mass m_e and the work functions of tip and sample W_t and W_s.

At low bias voltages $V \ll W_s, W_t$ the bias and energy dependence of the transmission

factor can be disregarded and equation 1.2 can be simplified to

$$\tau(s) = \exp\left(-2s\sqrt{\frac{m_e}{\hbar^2}}\sqrt{W_s + W_p}\right). \tag{1.3}$$

For low temperatures the Fermi distribution reduces to a step function, which yields for equation 1.1:

$$I(V,x,y,s) \propto \tau(s)\int_0^{eV} \rho_s(E,x,y)\rho_t(E-eV)\mathrm{d}E. \tag{1.4}$$

This simple model is only valid for weak coupling between the electrodes and in the case of low temperatures and low bias voltages, but it shows the exponential distance dependency ($\tau(s)$) of the tunneling current and the contribution of the LDOS of tip and sample (ρ_t and ρ_s). Thus, STM images are a convolution of the topography and electronic structure of both tip and sample.

1.2 Electrochemistry

The origin of electrochemistry goes back to the experiments of Volta and Galvani [93, 94] at the end of the 18th century connecting, for the first time, chemistry and electricity. Throughout the ages the meaning and scope of electrochemical science has varied [95] and since the 1980s the field of electrochemistry has evolved substantially. The textbook definition reads *"Electrochemistry is the branch of chemistry concerned with the interrelation of electrical and chemical effects. A large part of this field deals with the study of chemical changes caused by the passage of an electric current and the production of electrical energy by chemical reactions. In fact, the field of electrochemistry encompasses a huge array of different phenomena..."* [96]. Because of the wide breadth of the electrochemical (EC) field this section will be limited to a few underlying concepts and methods.

1.2.1 The Electrical Double Layer

Many EC experiments are carried out at the interface between chemical phases, typically an electronic conductor (the electrode) and an ionic conductor (the electrolyte). The electrode usually is a metal and the electrolyte a liquid solution of a salt, acid or base in water. At the interface, the properties of the two neighboring phases differ significantly from those of the bulk. The processes at the interface are of central interest and depend on the potential drop across the interface.

In general, the metal surface carries an excess charge, which is compensated by ions of opposite charge on the solution side of the interface. This means there is an excess or deficiency of electrons on the electrode surface and an excess of either cations or anions in the solution in the vicinity of the electrode surface. This can be viewed as a capacitor. The charge in the electrode resides in a surface region about 1 Å thick. In the solution the charge carrier concentration is lower than in a metal. Thus, the charge in the solution extends over a larger region of space, typically 5–20 Å thick. The resulting charge distribution (two narrow regions of equal and opposite charge) is known as the electrical double layer (EDL) and is a central issue in electrochemistry.

Figure 1.3 shows the structure and the potential distribution of the metal/electrolyte interface schematically for the case of a positively charged metal surface. The solution side of the double layer consists of several layers. The layer closest to the surface consists of ions that have partially lost their solvation shell and are in contact with the surface. They are held in place by chemical interactions with the surface and are referred to as "specifically adsorbed". They form the inner Helmholtz plane (IHP) at a distance x_1. Anions usually have a weak solvation shell and can absorb specifically. Most cations and some anions have a stronger solvation shell, which they retain upon adsorption. Solvated ions can approach the surface only to a distance x_2. Their interaction with the surface is purely electrostatic, thus essentially independent of the chemical properties of the ions. They are called "nonspecifically" adsorbed and form the outer Helmholtz plane (OHP) at x_2. From the OHP the diffuse layer extends into the bulk of the solution. In this three-dimensional region the nonspecifically adsorbed ions are distributed by an interplay of electrostatic interactions and thermal motion. The thickness of the diffuse layer depends on the ionic strength of the solution and the applied potential to the electrode.

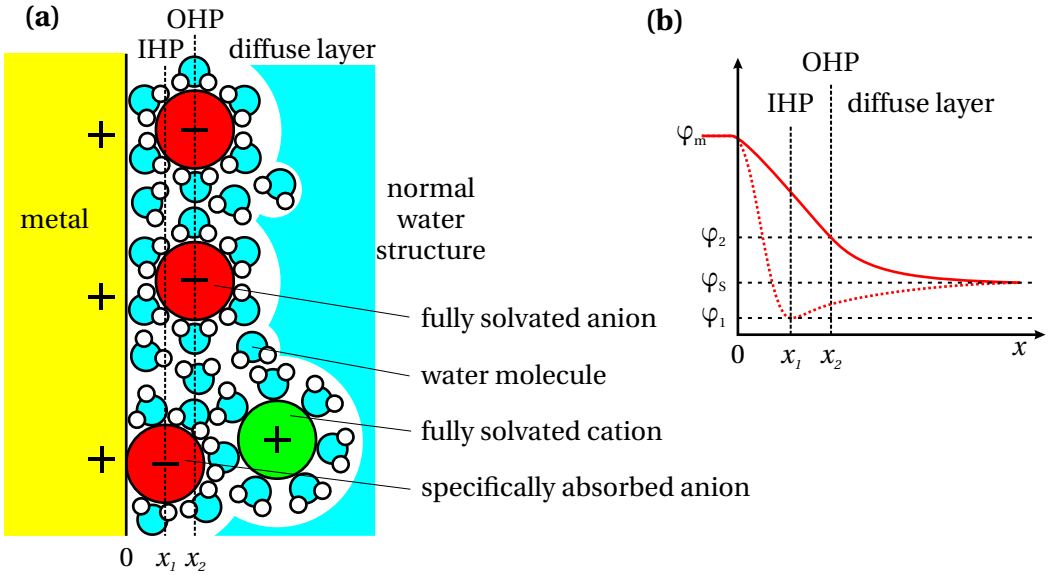

Figure 1.3: **(a)** Model of the metal-electrolyte interface (IHP: inner Helmholtz plane; OHP: outer Helmholtz plane). **(b)** Potential distribution across the electrical double layer for nonspecifically adsorbed anions (solid line) and specifically adsorbed anions (dotted line). Adapted from reference [97].

The potential profile across the double-layer region is shown in Figure 1.3b in the absence (solid line) and presence (dotted line) of specific adsorbing ions. For only nonspecifically adsorbing ions the potential drop between the metal surface and the OHP is generally assumed to be linear, as for a plate capacitor. This potential does not drop completely to the solution value φ_S, but only to some residual value φ_2. Across the diffuse layer the potential drops in an almost exponential form to φ_S. In the case of specifically adsorbed ions more charge is accumulated at the surface than required by electrostatics. This overcharging leads to a steeper potential gradient and the potential at the IHP φ_1 drops below the solution value. For charge compensation countercharge is brought into the double layer.

1.2.2 Electrochemical Cell

Experimentally, it is not possible to deal with an isolated interface, at least two electrodes separated by one (or more) electrolyte phases are needed. This is the simplest version of a socalled EC cell. In an EC cell either a chemical reaction generates an electrical current (Galvanic cell) or an electrical current is driving a chemical reaction (electrolytic cell). The overall reaction of an EC cell is split into two half-reactions,

reduction and oxidation at the cathode and anode, respectively. In contrast to "conventional" oxidation-reduction reactions, in EC systems oxidation and reduction are spatially separated and the actual exchange of electrons occurs at the electrodes.

Most EC experiments are performed in a three-electrode cell; the three electrodes are called working electrode (WE), reference electrode (RE) and counter electrode (CE). On the WE the processes and reactions under investigation take place. The current flows between the WE and CE and the potential of the WE is measured with respect to that of the RE. With only two electrodes (WE and CE) the potential between them would include contributions from the CE/electrolyte interface and the electrolyte itself. The third electrode allows separation of the potential and current measurements and investigation of the current voltage characteristics of the WE only. The RE is made up of phases with a fixed composition to establish a stable and well-known potential as a reference point. This allows one to determine the potential of the WE itself (with respect to the RE). To avoid in the potential measurement any overpotential contribution of the RE, no significant current must pass through it. This can be achieved with a high impedance voltmeter, forcing all current to flow between the WE and the CE. The CE is usually made of an inert material and does not participate in the EC reaction. The precise control and measurement of the potential of WE vs. RE and the current between WE and CE is realized with an instrument called potentiostat. A schematic picture of a three-electrode cell connected to a potentiostat is shown in Figure 1.4. The potentiostat can be viewed as an active element driving the required current through the WE in order to achieve the desired potential at any

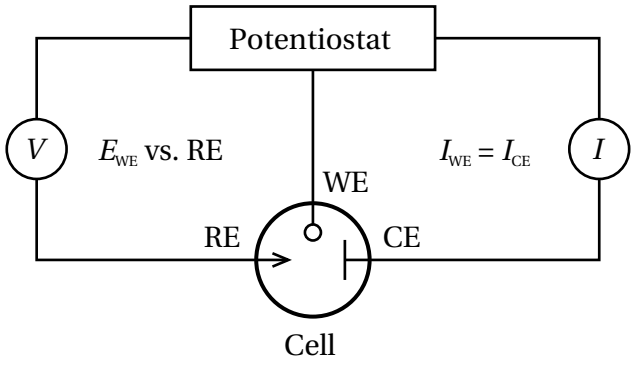

Figure 1.4: Scheme of a three-electrode electrochemical cell and potentiostat. In a three-electrode cell potential and current measurements are separated into a RE and a CE loop. The potential of the working electrode (WE) is measured with respect to the reference electrode (RE). The input of the RE has a high-impedance forcing all current to flow through the counter electrode (CE).

time. The potentiostat allows one to perform different EC experiments, which are classified according to the parameters held constant, controlled and measured.

1.2.3 Electrode Processes

At electrodes two type of process can occur. Adsorption/desorption and the formation of the EDL are processes where no charge is transferred across the metal-solution interface and are called nonfaradaic processes. Even though no charge crosses the interface, external currents can flow, when the potential or solution composition changes (cf. charging of a capacitor). Processes where charges are transferred across the metal-solution interface are called faradaic processes. The electron transfer causes oxidation or reduction to occur, which are reactions governed by Faraday's law. Thus, the flowing current is directly proportional to the reaction rate. The electrode potential allows the control of the rate and the direction of the interfacial electron transfer.

1.2.4 Electrode Reactions

The potentials at which electron transfer occur are related to the standard potentials E^0 of the specific chemical species in the system. The electrode potential under standard conditions of a given half-reaction

$$\mathrm{Ox} + ne^- \rightleftharpoons \mathrm{Red} \tag{1.5}$$

(where n is the number of transferred electrons) is called the standard potential of the Ox/Red couple $E^0_{\mathrm{Ox/Red}}$. By convention these electrode potentials are referred to the normal hydrogen electrode, which has by definition an electrode potential of zero.

The Nernst equation describes the dependence of the equilibrium potential E_{eq} of the Ox/Red electrode on the thermodynamic activities a_i of the components:

$$E_{\mathrm{eq}} = E^0_{\mathrm{Ox/Red}} + \frac{RT}{nF} \ln \frac{a_{\mathrm{Ox}}}{a_{\mathrm{Red}}} \tag{1.6}$$

with the universal gas constant R, the temperature T and the Faraday constant F.

For practical reasons the thermodynamic activities can be replaced by concentrations c_i and equation 1.6 transforms to give

$$E_{\mathrm{eq}} = E^{0'} + \frac{RT}{nF} \ln \frac{c_{\mathrm{Ox}}}{c_{\mathrm{Red}}} \tag{1.7}$$

where $E^{0'}$ is the experimental determined formal potential and can be described with activity coefficients γ_i as

$$E^{0'} = E^0 + \frac{RT}{nF} \ln \frac{\gamma_{\mathrm{Ox}}}{\gamma_{\mathrm{Red}}}. \tag{1.8}$$

$E^{0'}$ varies from medium to medium, because the ionic strength affects the activity coefficients.

The electroreduction and -oxidation of a species A in solution is schematically shown in Figure 1.5. The energy of the electrons in the electrode can be raised or lowered by bringing the electrode to more negative or positive potentials. For a sufficiently high negative potential electrons can be transferred from the electrode into the lowest unoccupied molecular orbital (LUMO) of A in the electrolyte. A is reduced to A^- and a reduction current flows. By definition the electrode where the reduction takes place is called the cathode, which is why the current is also referred as cathodic. If the potential is positive enough that electrons can be transferred from the highest occupied molecular orbital (HOMO) of A to the electrode, A is oxidized to A^+. In this case, the electrode is referred as the anode and the current as anodic.

In most cases electrode reactions are multistage processes and the electron transfer is only one step in the mechanism. Other steps, like mass transfer and chemical reactions, which precede or follow the electron transfer, influence the electrode reaction as well. The overall rate of a reaction (the current through the electrode) depends on the rate constants of these processes. The rate constants of some processes (e. g., electron transfer at the electrode surface) depend on the applied potential. Information about an electrode reaction are often obtained by measuring the current i as a function of the potential E (i-E-curves).

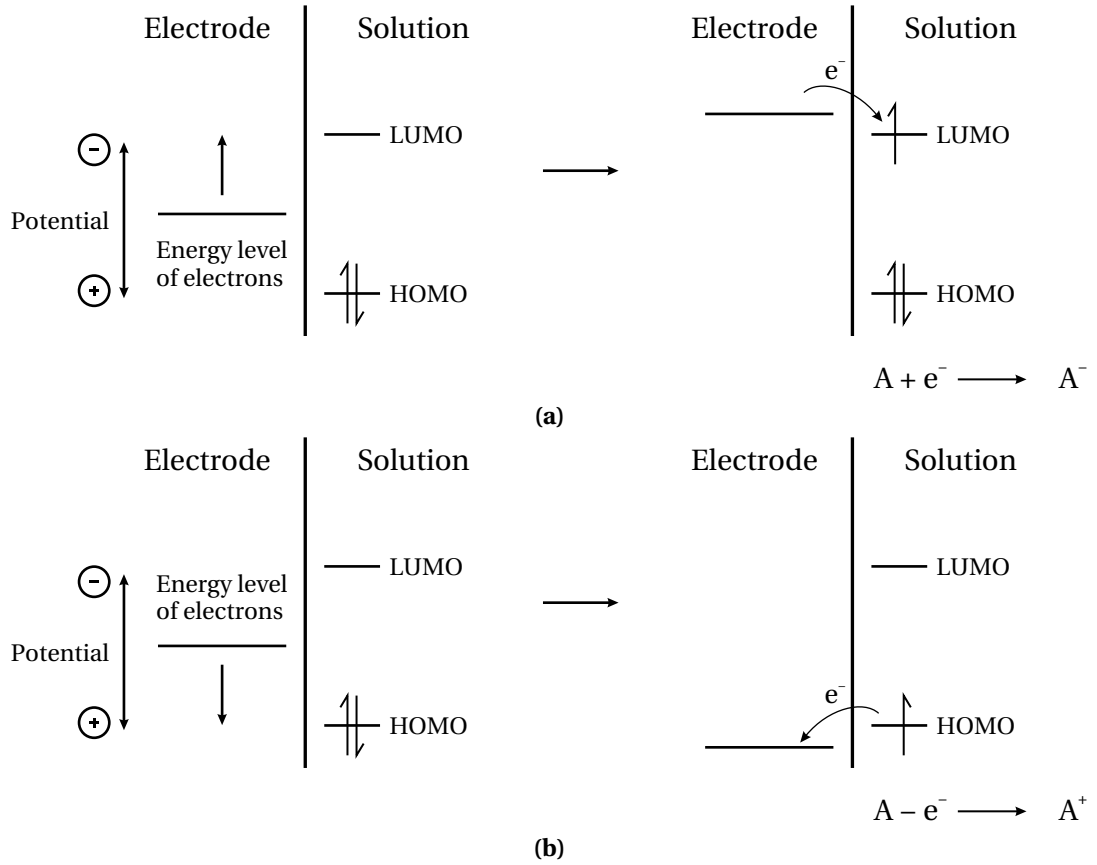

Figure 1.5: Representation of (a) reduction and (b) oxidation process of a species A in solution. Depending on the electrode potential the electron can either transferred into the lowest unoccupied molecular orbital (LUMO) or taken from the highest occupied molecular orbital (HOMO). HOMO and LUMO correspond in an approximate way to the standard potentials E^0s of the A/A^- and A^+/A couples, respectively.

1.2.5 Electrochemical Experiments

EC experiments are classified according to the parameters held constant, controlled and measured. Only linear sweep voltammetry and cyclic voltammetry are discussed here. These are techniques where the potential is constantly varied with time and the resulting current i is recorded as a function of the potential. In both techniques the potential is changed with a constant rate $\nu = \mathrm{d}E/\mathrm{d}t$. In cyclic voltammetry the potential is continuously ramped between an upper and lower value (Figure 1.6a). The first ramp of cyclic voltammetry to the return potential E_λ is equivalent to linear sweep voltammetry, where the potential is scanned once from an initial value to a final one. The resulting i-E-curves of cyclic voltammetry are called cyclic voltammograms (CVs). For linear sweep voltammetry the curves are called polarization curves.

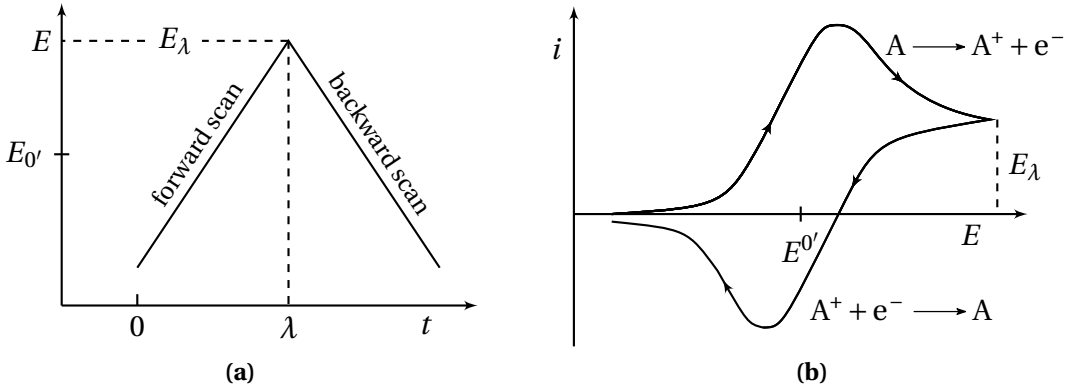

Figure 1.6: Cyclic voltammetry of a simple electron transfer reaction, where a species A in solution is oxidized to A^+ and subsequently reduced back to A. (a) single potential sweep and (b) resulting cyclic voltammogram (CV).

Figure 1.6b shows the CV of a redox-active species A in solution. The starting potential is negative of $E^{0'}$, the formal potential of the A^+/A couple. During scanning the potential towards more positive values, first only a nonfaradaic current flows. When the electrode potential E approaches $E^{0'}$, oxidation of A starts and a faradaic current begins to flow ($A \longrightarrow A^+ + e^-$). The resulting concentration gradient leads to diffusion of A from the bulk towards the surface. As the potential continues to become more positive, the surface concentration of A drops, which increases the flux to the surface (and the current). As the potential passes $E^{0'}$ the surface concentration of A drops nearly to zero and mass transfer of A to the surface reaches a maximum rate. The continued flux of A leads to an expansion of the depletion zone. Thus, the slope of the concentration profile at the surface declines and the current decreases. The result is a peak in the voltammogram (Fig.1.6b). After reaching the return potential E_λ the sweeping direction is reversed. Now in the vicinity of the electrode is a large concentration of the generated A^+. During this backward scan of the potential the EC balance at the surface becomes more and more favorable toward the neutral A species. A^+ is reduced and a cathodic current flows ($A^+ + e^- \longrightarrow A$). Again a peak is observed, essentially for the same reasons.

1.2.6 Electrocatalysis

EC reactions at a particular electrode material often either do not take place close to the thermodynamic potential of the system or take place only at a very small rate. Unlike homogeneous reactions, which have a constant rate at a given temperature,

in heterogeneous electron-transfer reactions the rate constant is a function of the applied potential. To drive the reaction at a measurable rate (flow of a faradaic current) considerably higher electron energies (higher potentials) must be applied than one would predict from thermodynamics. This additional potential needed to drive a reaction at a certain rate is called the overpotential η and is the energy difference between the electrode potential and its equilibrium value E_{eq} (the thermodynamic requirement):

$$\eta = E - E_{\mathrm{eq}} \tag{1.9}$$

In electrocatalysis the overpotential is of central interest. By lowering the overpotential the efficiency of a EC reaction can be greatly increased. The overpotential strongly depends on the electrode material and its structure. By using different materials or modifying the electrode surface the reaction rate can be significantly increased. If the surface itself is not consumed or irreversibly altered during the EC process, the activating surface is termed a catalyst. The catalytic activity can be caused by various effects, like an altered electronic structure of the electrode or an increased interaction with a reactant or intermediate state. An electrocatalyst can also change the pathway of a reaction.

Factors for a good electrocatalyst are a low overpotential (fast reaction kinetics) and a high current density (high reaction rate). The activity of an electrode is always compared to other systems; hence electrocatalysis is based on relative data. This is due to the fact that it is not really feasible possible to speak of a non-catalyzed reaction, because such a pathway would have to exist in the absence of an electrode surface.

1.2.7 Oxygen Reduction Reaction

The electrochemistry of oxygen is of great technological importance. Oxygen reduction takes place in fuel cells and batteries and oxygen evolution occurs in water electrolysis. Both oxygen reduction and evolution are slow processes and require large overpotentials, in the order of several 100 mV, to proceed, which makes any device using one of these reactions inefficient. The development of effective, inexpensive and stable catalyst is highly important for future energy conversion technologies.

ORR is a multi-electron reaction with a complicated mechanism and two parallel reaction pathways are observed. O_2 can either directly reduced to H_2O or on an indirect pathway via intermediate H_2O_2. The reduction may also stop at H_2O_2. A simplified scheme of the ORR mechanism is shown in Figure 1.7. The direct and indirect pathways are competing processes and the rate constants k_i of the different reactions determine which pathway is dominating.

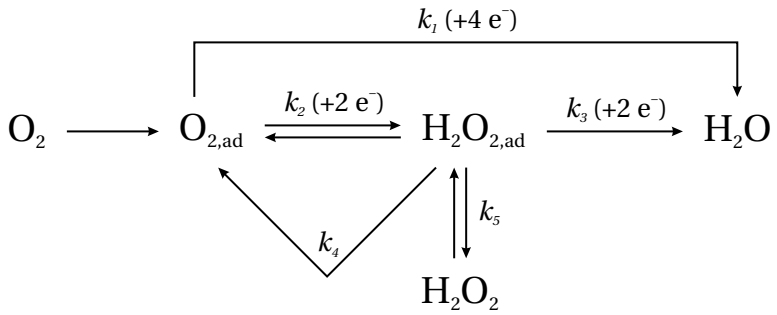

Figure 1.7: Simplified mechanism of the oxygen reduction reaction. [98] The direct (k_1: $4e^-$ mechanism) and indirect ($k_2 + k_3$: $(2+2)e^-$ mechanism) pathways are competing processes.

The complete reduction of O_2 to H_2O (OH^- in basic media) involves four electrons (e^-). In the direct pathway (k_1) this occurs via a $4e^-$ mechanism according to the following equation:

$$O_2 + 2H_2O + 4e^- \longrightarrow 4\,OH^- \tag{1.10}$$

The stepwise reduction of O_2 to H_2O in the indirect pathway ($k_2 + k_3$) occurs via a $(2+2)e^-$ mechanism. O_2 is first reduced (k_2) to H_2O_2 ($HO_2{}^-$ in basic media) on a $2e^-$ pathway according to the following equation:

$$O_2 + H_2O + 2e^- \longrightarrow HO_2{}^- + OH^- \tag{1.11}$$

The adsorbed hydrogen peroxide ($H_2O_{2,ad}$) can be chemically decomposed on the electrode surface (k_4)

$$2H_2O_2 \longrightarrow O_2 + 2H_2O, \tag{1.12}$$

desorbed into the electrolyte solution (k_5), and/or further reduced to water (k_3). The reduction of H_2O_2 to H_2O ($HO_2{}^-$ to OH^- in basic media) occurs on a $2e^-$ pathway

according to the following reaction:

$$HO_2^- + H_2O + 2e^- \longrightarrow 3\,OH^- \tag{1.13}$$

In fuel cells the direct $4e^-$ pathway is highly preferred since it allows one to obtain the maximum energy capacity. The indirect pathway leads to a lower energy conversion efficiency and the intermediate H_2O_2 can further convert to harmful free radical species and causes the degradation of the catalytic sites. Pt and its alloys are known to promote the $4e^-$ ORR pathway.

Chapter 2

Experimental Setup and Details

This chapter is a description of the experimental setup used during this thesis. In section 2.1 the experimental setup is presented. Experimental details are given in section 2.2, concerning sample holder and sample preparation, as well as EC experiments.

2.1 Experimental Setup

In this thesis all sample preparation and STM characterization was performed under UHV conditions. The EC measurements were performed in an EC cell at ambient pressure. To combine UHV and EC environment in one setup, a transfer chamber was placed between the main UHV chamber and the EC cell, which allows one to transfer the sample between both environments in a clean, controlled and effective way. The transfer system will be further discussed in chapter 3. This section deals with the experimental details of the complete setup.

An experiment starts with the sample preparation (section 2.2.2). Using STM, the network formation is checked, the structure determined and the coverage analyzed. Then, the sample is brought via the transfer chamber to the EC cell to perform the EC measurements. Afterwards the sample is brought back to UHV through the transfer chamber. STM then allows one to check for the stability of the networks and study possible structural changes due to the EC measurements.

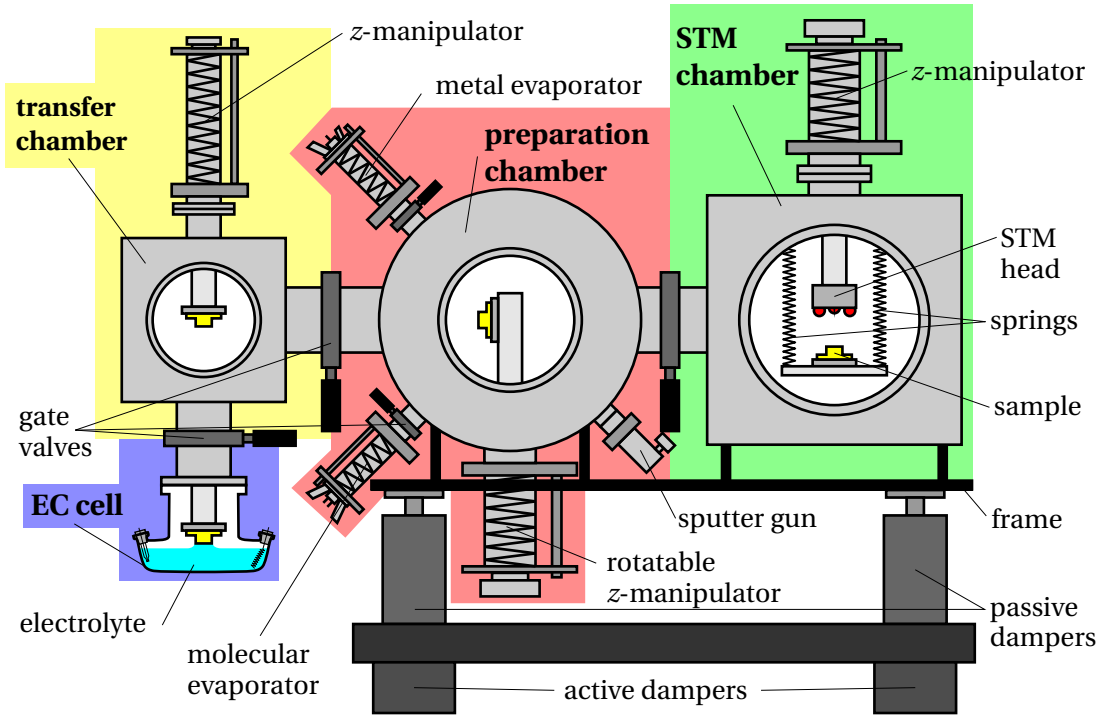

Figure 2.1: Schematic drawing of the experimental setup. The EC cell, transfer, preparation and STM chamber are highlighted with different colors. To obtain high stability for STM measurements three different damping stages are used (active and passive dampers and spring suspensions).

The complete setup consists of two UHV chambers, the transfer chamber and the EC cell. A schematic drawing is shown in Figure 2.1. Photographs of the system can be seen in Figure 2.2. The preparation and STM chambers are kept under UHV conditions at all times. The STM chamber is separated from the preparation chamber by a gate valve to keep the pressure in the STM chamber always as low as possible, even during sample preparation or sample transfer to the transfer chamber. The transfer chamber is placed between the preparation chamber and the EC cell, separated from each with a gate valve. The EC cell is located below the transfer chamber and allows one to work in a controlled atmosphere.

The preparation chamber has a base pressure of around $3 \cdot 10^{-10}$ mbar. Several pump types are attached; a turbomolecular, an ion getter and a titanium sublimation pump. Furthermore, it is equipped with a quadrupole mass spectrometer to analyze residual gases, an ion gun for sputtering and a sample storage. In addition, a load-lock allows one to transfer samples and tips between ambient and UHV conditions. The sample is attached to a manipulator, which can be rotated and moved up and down to bring

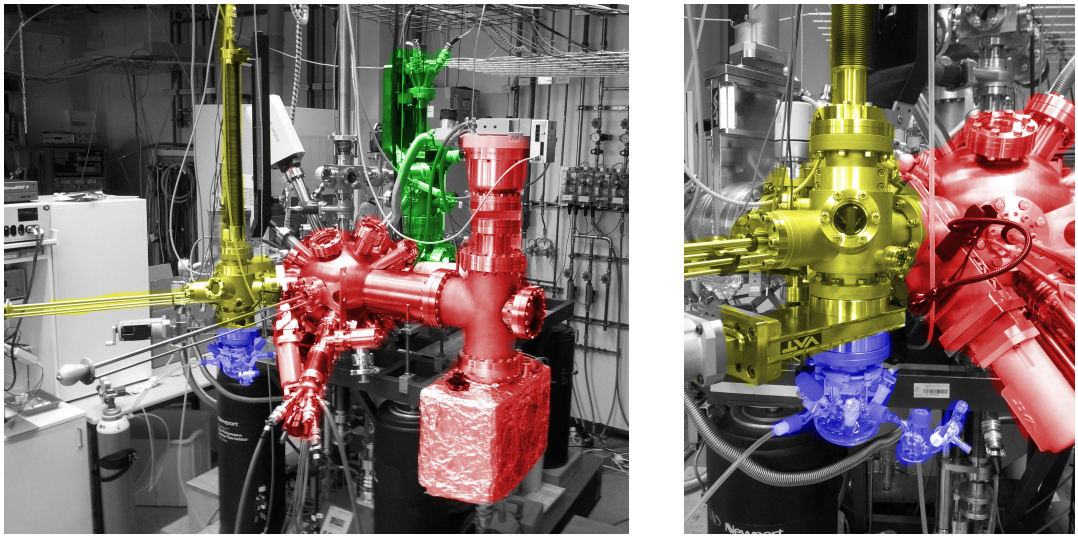

(a) **(b)**

Figure 2.2: Photographs of the experimental setup with false colors highlighting preparation chamber (red), STM chamber (green), transfer chamber (yellow) and EC cell (blue).

the sample to the different preparation positions. The molecule and metal evaporators can be separated from the main chamber with small gate valves to exchange the loaded materials without breaking the vacuum in the main chamber. The sample is transferred with a wobble stick to the STM chamber.

The base pressure of the STM chamber is below $1 \cdot 10^{-10}$ mbar. Again, a combination of turbomolecular, ion getter and titanium sublimation pump is used. The sample faces upwards and placed in a basis hanging on four metal springs. The STM head is lowered with a z-manipulator and placed above the sample. The STM head can be positioned above any place of the sample surface. The coarse tip approach is realized with a commercial linear z-piezomotor (attocube systems AG). Scanning is performed at room temperature and conducted with a single tube scanner. Besides the actual STM, the chamber also hosts a tip storage with seven slots, which allows one to exchange the tip *in-situ*.

The sample is brought from UHV to the EC cell via the transfer chamber to keep it in a clean and controlled environment at all times. The transfer chamber is pumped by a turbomolecular pump and has a base pressure of around $2 \cdot 10^{-8}$ mbar. The transfer chamber can be either pumped down to UHV or filled with ultra pure argon gas to atmospheric pressure without affecting the vacuum in the main UHV chamber. Using a wobble stick, the sample is placed on a linear z-manipulator, which transports

it down to the EC cell.

The EC cell is a conventional three-electrode setup, with the sample as the working electrode. A schematic drawing of the EC cell is shown in Figure 2.3. The cell is made of glass and has four ground joints; for the reference and counter electrode, to fill the cell with electrolyte and a device to bubble gases into the solution or maintain a gas flow above it. Working methods from the Schlenk techniques are adapted to obtain a controlled atmosphere in the cell. For this purpose, the cell is equipped with two teflon taps; one to evacuate the cell and fill it with clean gases while the other serves as an outlet. The sample faces down and the EC measurements are performed in the hanging meniscus configuration [99, 100]. To establish the hanging meniscus, first the sample surface is wetted with a hanging droplet of water, then it is brought in contact with the electrolyte surface. This procedure minimizes the risk of wetting other parts of the sample or sample holder. To wet the sample surface a device (called a drop-maker) with a specially shaped pipette is employed. After EC measurements the sample surface is rinsed with another drop-maker with milliQ water. The sample is brought back into UHV via the transfer chamber.

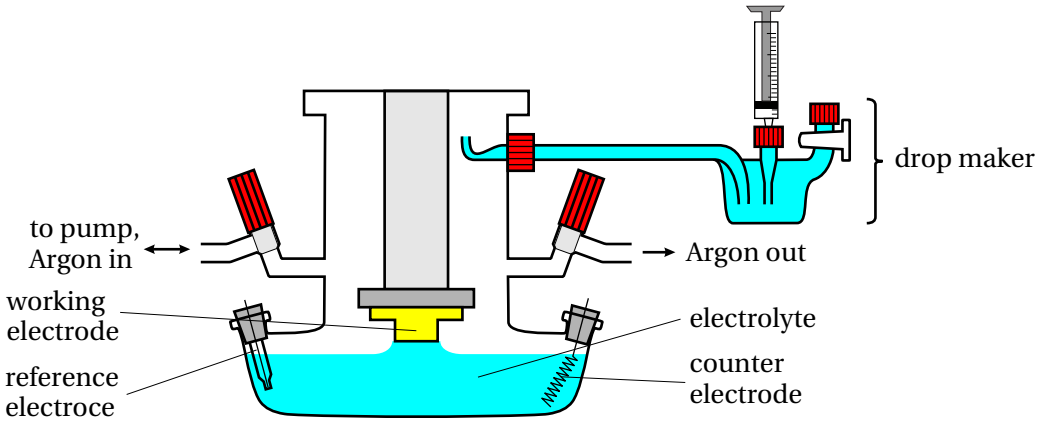

Figure 2.3: Schematic drawing of the EC cell. Two more ground joints are omitted for clarity. One is used to fill the cell with electrolyte, the other for a device to bubble gases into the solution or maintain a gas flow above it.

2.1.1 Mechanical Vibrations and Electrical Noise

A crucial part in STM is the isolation of the system against mechanical vibrations and preventing of electrical noise. To reduce mechanical vibrations the turbomolecular pumps are stopped during STM measurements. The ion getter pumps have no moving parts and stay switched on to maintain the UHV conditions of preparation and STM chamber.[1] Also, all other sources of mechanical noise, e. g. the air ventilation of the fume hoods in the laboratory, are shut down during this time if possible. The high stability necessary for STM is obtained by three different damping stages (Fig. 2.1).

The whole setup is placed on an optical table, which is decoupled from the floor by four active dampers. The UHV chambers are mounted on a frame, which sits on four passive dampers. During STM measuring the passive dampers are filled with compressed air to decouple the frame and optical table. The backing pump system is placed on the optical table and the tubing to the turbomolecular pumps connects it to the chambers. To reduce vibration transmission between this two damping stages flexible metal tubes are used. Most of the electrical cabling to the chambers is guided along a grid suspended from the ceiling to make the connections as flexible as possible. Rigid cables, such as from the titanium sublimation pump, are unplugged from the chamber during STM measurements. The last damping stage is located inside the STM chamber. Sample and STM head are placed on a basis, which is freely hanging on four metal springs.

Prevention of electrical noise that couples to the tunneling current is another important task and proper grounding plays a major role. Therefore the whole setup is separated from the ground of the power supply system during STM measuring and a "clean ground" is provided for the used electronics.

All electronic equipment not necessary for STM is unplugged from the power supply system during measuring (except the ion getter pump controllers). The water cooling tubes are even removed, because they are grounding the setup in the MΩ regime. Cabling found to generate electronic noise (e. g. the cable from the metal evaporator) is disconnected from the chamber. Isolation transformers are used to power the STM electronics, the measuring computer and the ion getter pump controller, but keep them separated from the power ground. The switch providing the network connection for the computer is powered by an isolation transformer as well.

[1] The transfer chamber remains under static vacuum during this time period.

The whole setup is grounded via a cable running from a "clean ground" in the laboratory to a copper plate serving as common ground. The copper plate is mounted on the STM chamber and the current amplifier of the STM directly on this copper plate. The STM electronics are grounded by the cables running to the STM chamber. The ion getter pump controllers are directly connected to the copper plate with a cable grounding them.

2.2 Experimental Details

2.2.1 Sample Holder

To fulfill the requirements for sample preparation, STM and EC measurements a special sample holder was designed. A photograph and a schematic drawing of the sample holder are shown in Figure 2.4. The crystal is placed on a tantalum interface, which can be heated from the back by electron bombardment in the preparation manipulator. The sapphire ring reduces heat transfer to the base plate and the thermocouple allows temperature reading. The crystal is well fixed in the sample holder for high mechanical stability during STM. The crystal surface is the highest point of the whole assembly, so that in the hanging-meniscus configuration no other parts get wet.

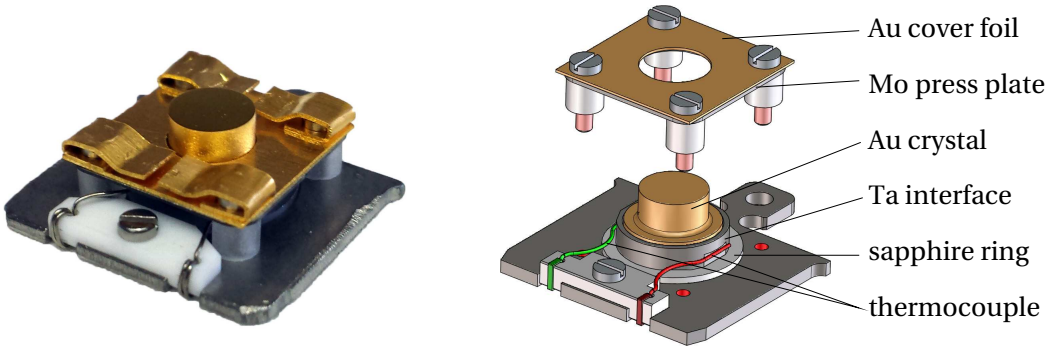

Figure 2.4: (a) Photograph and (b) schematic drawing of the sample holder.

A crucial point is the covering of the top parts with high-purity gold foil. During sputtering the ion beam also hits the sample holder itself, which can lead to deposition of material from the sample holder to the side faces of the crystal. These contami-

nations usually do not affect the surface, but in the hanging meniscus configuration small parts of the side faces of the crystal are wetted, which may cause unexpected effects in electrochemical experiments [99]. To avoid this unwanted sputter deposition of foreign metals, the molybdenum press plate and the screw heads are covered with gold foil.

2.2.2 Sample Preparation

In this thesis all MOCNs have been prepared *in-situ* under UHV conditions on a single crystal Au(111) surface. The sample preparation started with cleaning of the crystal surface, then the molecules were deposited, followed by metal evaporation and subsequent annealing. The substrate temperature during molecule and metal deposition and annealing varied depending on the different molecules. Details are given in the corresponding sections.

The single crystals (supplier: MaTecK GmbH and Surface Preparation Laboratory) were hat shaped with a polished surface of 5 mm diameter. They were cleaned under UHV conditions by repeated cycles of sputtering with Ar^+ ions and subsequent annealing. The ion beam for sputtering had an energy of 1 keV and an incidence angle of 45°, resulting in a current on the sample of about 10 μA. The sample was sputtered for 10 min at temperatures below 375 K. During annealing at 825 K for 10 min the pressure usually was below $3 \cdot 10^{-9}$ mbar.[2] After an electrochemical experiment two cleaning cycles were used to again obtain an atomically clean and flat surface with regions with terrace widths of around 100 nm.

The molecules were deposited by an organic molecular beam epitaxy source (Dodecon Nanotechnology GmbH) from a resistively heated quartz crucible. The sublimation temperatures (T_{Sub}) are listed in table 2.1. The deposition rates varied from 0.01–0.1 monolayer per minute. Before deposition the molecules were carefully degassed 10–20 K below the sublimation temperature.

Metal atoms were deposited by electron beam heated evaporators (EFM 3, Omicron GmbH). Fe and Co were evaporated from a rod and Mn from flakes in a molybdenum crucible. The flux was typically below 0.01 of a monolayer per minute. The metal evaporators were degassed before use.

[2] During the first annealing after an electrochemical experiment the pressure was higher.

Molecule	Chemical Name	T_{Sub}	Supplier
TMA	Benzene-1,3,5-tricarboxylic acid	465 K	Sigma-Aldrich
TCNQ	7,7,8,8-tetracyanoquinodimethane	385 K	Sigma-Aldrich
PBP	5,5'-Bis(4-pyridyl)(2,2'-bipyrimidine)	470 K	synthesized*
FePc	Iron(II)-phthalocyanine	663 K	Alfa Aesar
H_2TPyP	5,10,15,20-Tetra(4-pyridyl)-porphyrin	663 K	Frontier Scientific, Inc.
CuTPyP	Copper(II) 5,10,15,20-tetra(4-pyridyl) porphyrin	683 K	Frontier Scientific, Inc.
FeTPyPCl	Iron(III) 5,10,15,20-tetra(4-pyridyl) porphyrin chloride	748 K	Frontier Scientific, Inc.
CoTPyPCl	Cobalt(III) 5,10,15,20-tetra(4-pyridyl) porphyrin chloride	683 K	Frontier Scientific, Inc.

Table 2.1: Sublimation temperatures T_{Sub} of the different molecules used in this thesis. *PBP was provided by the group of Professor Mario Ruben (Karlsruhe Institute of Technology, Institute of Nanotechnology, Karlsruhe, Germany).

2.2.3 Electrochemical Experiments

The EC experiments were performed in a conventional three-electrode cell using an Autolab potentiostat (PGSTAT302N, Eco Chemie). Silver/silver chloride (3 M KCl) was used as reference electrode. All potentials are referred to the Ag/AgCl/(3 M KCl) reference electrode. Usually a coiled platinum wire served as counter electrode, but in case of hydrogen peroxide addition a coiled gold wire was used. The 0.1 M sodium hydroxide solution was prepared using NaOH pellets from Sigma-Aldrich (99.99 % trace metals basis) and milliQ water (18.2 MΩ). Oxygen and Argon gases were of N5.0 purity and were bubbled for 30 min into the solution to saturate in the solution.

All glassware was cleaned prior to first use in a two-step procedure. First the glassware is soaked in a sodium hydroxide and potassium permanganate solution over

night. Permanganate is a strong oxidizing agent and reacts with organic contaminations, generating a brown precipitate (MnO_2). After rinsing the glassware with deionized water a solution of sulfuric acid and hydrogen peroxide is used to reduce MnO_2 to water soluble Mn^{2+}. This step takes around 1 h. Afterward the glassware is thoroughly rinsed first with deionized, then milliQ water. After an electrochemical experiment the glassware was rinsed with deionized and milliQ water.

Chapter 3

Transfer between Ultra-High Vacuum and Electrochemistry Environments

This chapter gives a brief introduction to the developed transfer system for combining UHV and electrochemistry environments (Section 3.1). A detailed description and discussion of the transfer system realized in this thesis is given in section 3.2. The transfer between UHV and EC environments in both directions is demonstrated for a clean Au(111) surface (3.2.1) and the STM characterization of a metal-organic coordination network after electrochemistry is shown (3.2.2).

3.1 Transfer systems

The combination of UHV and EC methods started in the late 1970s; on the one hand to employ UHV analysis techniques on samples coming from a liquid environment, on the other hand to study the EC behavior of well-defined UHV prepared samples. EC techniques are powerful methods to study many phenomena at the solid-liquid interface as they are very sensitive to any change in the interface composition, but they do not, however, give direct information at the molecular or atomic level. Therefore, EC studies were combined with surface-sensitive characterization techniques in UHV to obtain structural information of the interface (LEED: low energy electron diffraction) and to determine the chemical composition and the oxidation state of surface components (XPS: x-ray photoelectron spectroscopy; AES: Auger electron

spectroscopy). Working in UHV also offered the advantage of rigorously control over the sample preparation by means of sputtering-annealing cycles and by LEED, XPS and AES. This allowed one to electrochemically study well-defined and tailored single crystal surfaces serving as model electrodes.

The first samples were simply transferred in air, which lead to uncontrolled surface contamination or post-oxidation. Since the 1980s, fully controlled UHV-based transfer systems were developed in order to keep the sample at all times in a clean and controlled environment. Depending on the requirements of different systems and employed techniques, as well as the geometry of the UHV chamber, several approaches and various designs exist [99, 101]. Instead of venting the main UHV chamber, preferably the sample is brought into an external compartment, that can be filled with ultra pure gases without affecting the vacuum in the main UHV chamber. This external compartment is called an antechamber or transfer chamber. The EC experiments can be performed within the vented antechamber, using special designed EC cells introduced via a gate valve either from below or from the side. Another possibility is to have the EC cell outside the transfer chamber.

3.2 Transfer System realized in this Thesis

We followed designs where the EC cell is located outside the transfer chamber or, more precisely, underneath it [102–104]. This configuration with the EC cell outside the transfer chamber offers many advantages. From the EC point of view it is the best option: As the design of the cell is much closer to conventional cells, one can work with the usual volumes of liquid in a well-established configuration. It offers more flexibility in the cell design and different cells depending on the type of experiments can be realized (e. g. double walled cells for temperature control of the solution). Additionally, it allows easy visual control of the hanging meniscus and the cell can be easily removed for thoroughly cleaning. In the case that other parts of the sample or sample holders are wetted by the electrolyte, it is quite simple to take the sample out of the manipulator for rinsing with milliQ water and to introduce it back into the system. In our cell design, reference and counter electrode are inserted into the EC cell through ground joints, which allows to exchange them within a few seconds.

Figure 3.1 shows a schematic drawing of the transfer system realized in this thesis. A photograph of the setup can be seen in Figure 2.2. The transfer chamber is at the same horizontal level as the the preparation chamber and placed directly next to it. With the wobble stick the sample can transferred between the two manipulators in the transfer and preparation chambers. With the z-manipulator in the transfer chamber the sample can be brought down to the EC cell, which is located below the transfer chamber. The complete sequence, to bring a sample controlled out of UHV, perform an EC experiment and bring the sample back to UHV is described in the following.

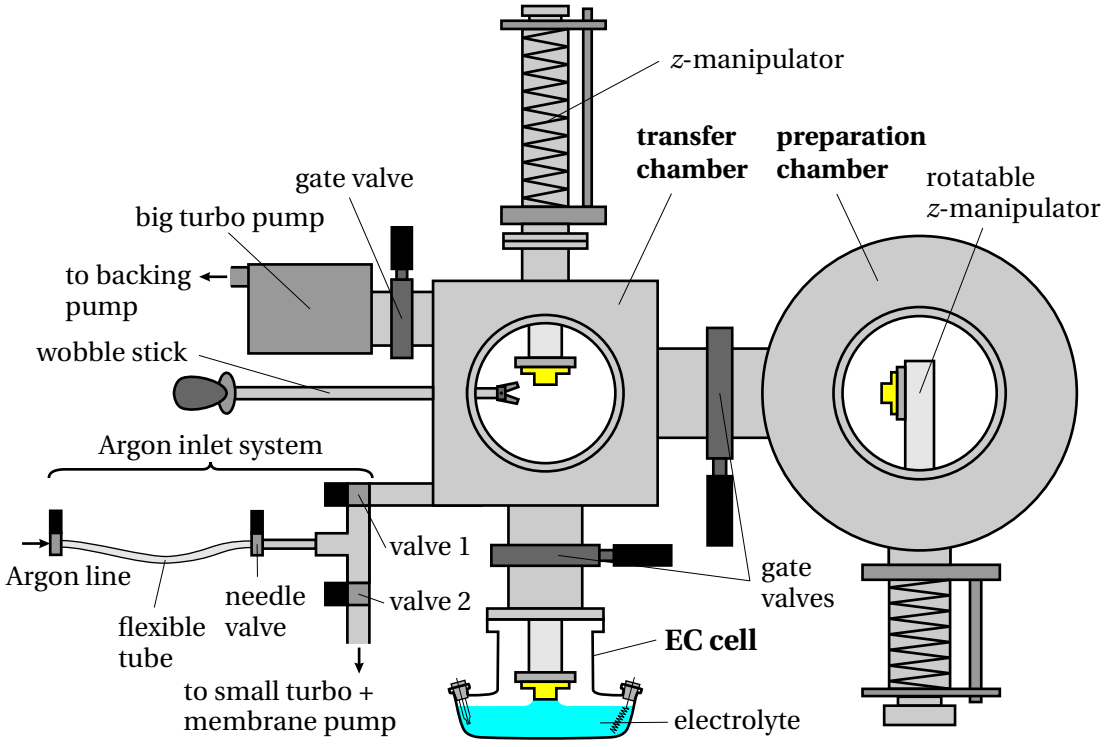

Figure 3.1: Schematic drawing of the transfer system realized in this thesis. Several valves are used in the Ar inlet system to have maximum control of the whole transfer process.

The starting point is a sample in the preparation chamber and the transfer chamber is at its base pressure of around $2 \cdot 10^{-8}$ mbar. All valves are closed, besides the one between the transfer chamber and the turbo pump. The EC cell is prepared in advance; first it is pumped, then filled with Ar, subsequently the electrolyte is introduced and a stable and controlled atmosphere maintained. Thus, electrochemistry can be started directly after the transfer.

Before the sample is brought to the transfer chamber the Ar inlet system is pumped by opening valve 2 to an external pumping station[1] and the needle valve. It should be pumped for at least several minutes, but preferably longer. Then, the gate valve to the preparation chamber is opened, the sample grabbed with the wobble stick, brought to the transfer chamber and the gate valve immediately closed again. The time period where this valve is open is very short (less than 30 seconds), therefore the effect on the vacuum in the preparation chamber is really little. After that the needle valve is closed (in the closed position it still allows a small flow through it), valve 1 to the transfer chamber is opened and valve 2 to the extra pumping station is closed. The Ar line is slowly opened and as soon as an Ar flow starts, the gate valve to the turbo is closed. Then the needle valve is fully opened to increase the Ar flux and it takes 7–8 minutes to bring the transfer chamber to atmospheric pressure. After that the gate valve to the EC cell is opened and the sample lowered into it. During EC experiments a slight Ar overpressure is applied to the transfer chamber and the EC cell to prevent air contamination.

The sequence of how the different valves are opened and closed has several aims. One reason is to purge the inlet system by pumping it and to reduce pressure differences when valves are opened to prevent potential damage on them. The main objective is to keep the transfer chamber pumped by the big turbo pump for as long as possible to ensure the cleanliness. Just before the Ar line is opened the big turbo pump is still pumping the transfer chamber and a situation is obtained with differential pressure stages and a stepwise reduction of the diameter of the intake system to the Ar line. The valve to the turbo is not closed until the Ar flow to the chambers sets in.

The complete sequence to bring a sample out of UHV to the EC cell is rather complicated and one needs to take care to follow the right order. However, it allows full control over of the whole process and ensures high cleanliness of the transfer. It takes only about 10 minutes from the sample being in UHV to the start of the EC experiment, which is a sufficient time period for our requirements. The longest step is the actual filling of the chamber, limited by the maximum flow through the needle valve. It was intentionally chosen to be small for a slow filling process in order to have maximum control, especially in the beginning. If one would like to speed up the filling an additional bypass valve allowing a higher flow could be used.

[1] This pumping station is completely separated from the backing pumps system of the UHV chambers.

After the EC experiment the sample surface is rinsed with milliQ water, the sample brought back in the transfer chamber and the gate valve to the EC cell closed. After closing the Ar line, valve 2 is opened and the transfer chamber is pumped with the membrane pump and then the small turbo is started. In an early design the valves 1 and 2 and the connectors between them had a quite small diameter (6 mm outer diameter) and it took 15–20 minutes before the pressure in the transfer chamber was low enough to open the gate valve to the big turbo pump. The valves and connections in between were changed and valve 1 has now a CF16 flange and valve 2 a KF16 flange, allowing a much faster initial pump down. With the new valves the pressure in the transfer chamber is below $1 \cdot 10^{-1}$ mbar within a few minutes allowing one to open the gate valve to the big turbo and close valve 1 between the chamber and the inlet system. It takes around 1 h until the pressure is below $1 \cdot 10^{-6}$ mbar and the sample can be transferred back to the preparation chamber. Again, the gate valve to the preparation chamber is only opened for as short a time as possible. Directly after the transfer the pressure is slightly higher in the preparation chamber, but recovers within 5–10 minutes. The effect on the pressure in the preparation chamber is smaller with lower pressures in the transfer chamber before transferring the sample back, and thus it is preferred to wait a bit longer than the minimum time of 1 h to obtain a better pressure in the transfer chamber.

In our design, the gate valve between transfer chamber and EC cell has to stay open during the EC experiments, because the manipulator arm is blocking it. Water vapor from the electrolyte enters the transfer chamber and adsorbs on the inside walls. During pumping down, of the transfer chamber, this water slowly desorbs and it takes several hours to reach again the 10^{-8} mbar range, the value before transferring the sample out of UHV. However, after around 1 h the pressure is already low enough to transfer the sample back, without affecting the pressure in the preparation chamber significantly. It is possible to realize a faster transfer by using two transfer chambers [104], but we wanted to keep the design more simple. A possibility to accelerate the pump-down of the existing system could be the implementation of a cryopump to pump more efficiently the water vapor. Hwever, the effect may be small as the water molecules still need to desorb from the inside walls and hit the cryopanel.

The Ar inlet system is also used for a secondary purpose. An additional valve (omitted in the drawing in Figure 3.1 for clarity) is goes the EC cell and used for the preparation of the EC cell. It allows to pump the cell and fill it with Ar to obtain a controlled atmosphere in it. Another valve is omitted as well, which leads to an outlet to prevent

to high overpressures on the transfer chamber. Furthermore the transfer chamber is equipped with a pressure burst disc as an additional precaution.

Usually STM measurements are performed directly before the EC experiments and therefore in the daily lab routine first the backing pump system and the turbo pumps of the UHV chambers are started. During STM, the transfer chamber is under static vacuum and it takes some time until the pressure is low enough to transfer the sample out of the preparation chamber. This time is used for all preparing steps before the actual transfer. In our design the time period between retracting the STM tip and starting the EC experiment is less than 1 h and most of this time the sample is still under UHV.

The transfer system realized in this thesis provides a clean and controlled transfer of samples between UHV and EC environment in a reasonable time period. To demonstrate the efficacy and cleanliness of the process STM and EC measurements of a bare Au(111) surface were performed and typical results were obtained. STM measurements of MOCNs after EC experiments were more difficult to perform, but could be shown for the PBP–Fe network.

3.2.1 Test System Au(111)

The transfer system was tested with a clean Au(111) surface, because it is a rather simple system, easy to prepare, well-known in STM and electrochemistry, and one gets typically results, serving as "fingerprints", in both. In addition it allows one to work in a wide potential window, which is why we used it as substrate for the two-dimensional metal-organic coordination networks.

Figure 3.2 is a STM image of a clean Au(111) surface after Ar^+ sputtering and annealing, showing the typical thermally induced herringbone reconstruction obtained in UHV and ambient conditions [105, 106]. The double rows are a result of an average compression of the surface layer by 4 % in one of the three close-packed [$\bar{1}$ 1 0] causing a $22 \times \sqrt{3}$ reconstruction. Sets of these corrugation lines change periodically their orientation in a zig-zag pattern by ±120°, generating the herringbone superstructure.

The clean Au(111) sample was brought from UHV through the transfer chamber to the electrochemical cell to perform electrochemical experiments. Figure 3.3 shows a cyclic voltammogram (CV) of the sample in deaerated 0.05 M H_2SO_4 in the potential

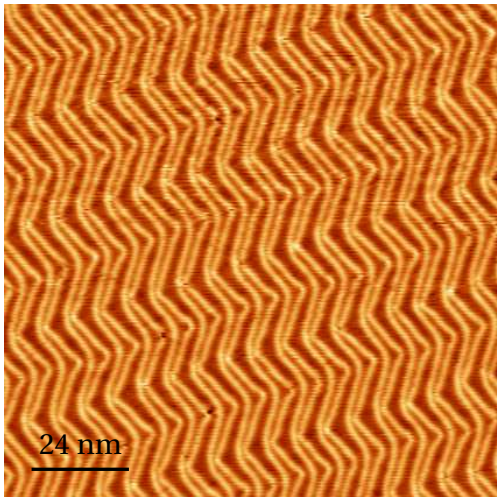

Figure 3.2: STM image of the clean Au(111) surface showing the typical thermally induced herringbone reconstruction obtained in UHV.

window from -0.1 V to 1.5 V. It shows the characteristic profile of an Au(111) surface with the oxidation above 1.2 V and the reduction around 0.9 V [107]. This CV serves as "fingerprint" of a clean Au(111) surface, just like the herringbone in STM. The CV is sensitive towards contaminations, but no additional current features can be seen.

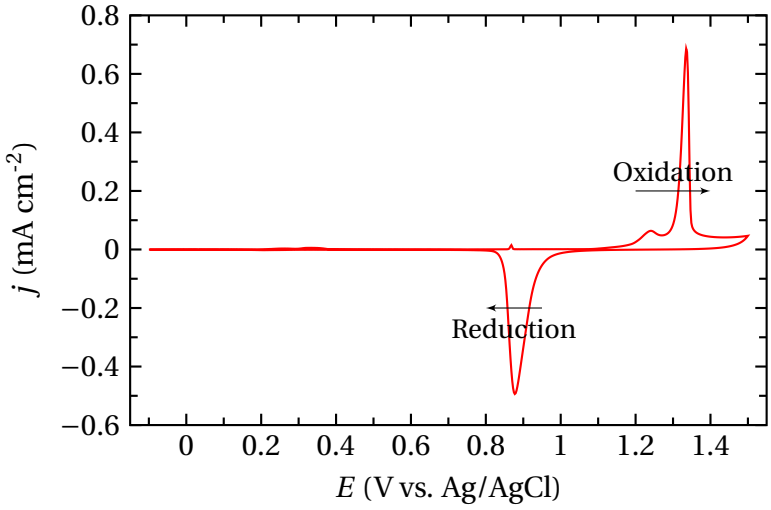

Figure 3.3: Cyclic voltammogram of Au(111) showing the oxidation/reduction of the surface in deaerated 0.05 M H_2SO_4, scan rate 50 mV s^{-1}.

Figure 3.4 shows a CV of the sample in a smaller potential window. The upper potential is reduced to a value before the oxidation of the surfaces occurs, thus only the double layer is present. The anodic/cathodic peaks between 0.1–0.4 V correspond to the lifting/recovering of the reconstruction and around 0.8–0.9 V a disorder/order

transition takes place within the layer of adsorbed (hydrogen-) sulfate ions [108]. At negative potentials the reconstruction is still present, but during the anodic scan the reconstruction is lifted between 0.2–0.4 V. In the cathodic scan the reconstruction is recovered around 0.2 V. This potential-induced reconstruction differs from the initial thermally induced reconstruction and can be seen in Figure 3.5.

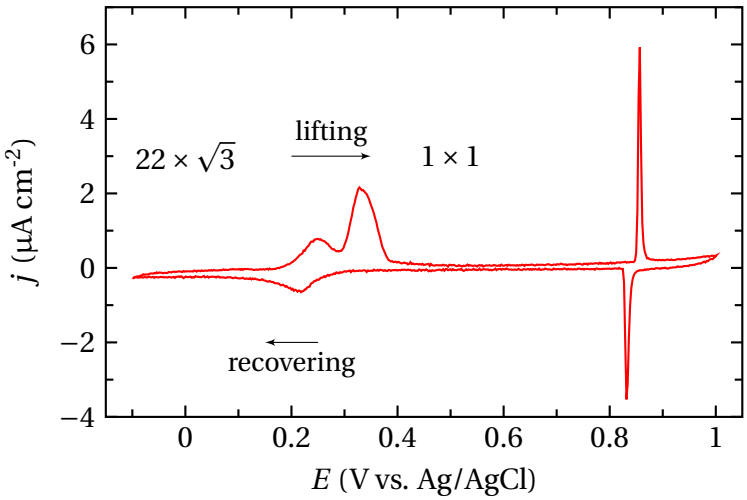

Figure 3.4: Cyclic voltammogram of Au(111) in the double layer region in deaerated 0.05 M H_2SO_4, scan rate 50 mV s^{-1}. The peaks between 0.1–0.4 V correspond to the lifting/recovering of the reconstruction and around 0.8–0.9 V a disorder/order transition takes place within the layer of adsorbed (hydrogen-) sulfate ions.

After lifting and recovering the reconstruction the sample is retracted under potential control, at a potential where the reconstruction is present. The surface is rinsed with milliQ water and the sample transferred back to UHV. Figure 3.5 shows an STM image of the Au(111) after the EC experiment. The double rows run no longer in a regular zigzag pattern as in the case of the initial thermally induced reconstruction (Fig. 3.2). The pattern of the potential-induced reconstruction is more irregular and the double rows tend to align with the step edges. In the STM no contamination of the surface can be seen after the EC experiment. The STM image is a bit more noisy than before; the step edges are diffuse and horizontal lines in the fast scan direction appear. This could be due to adsorbed mobile water molecules.

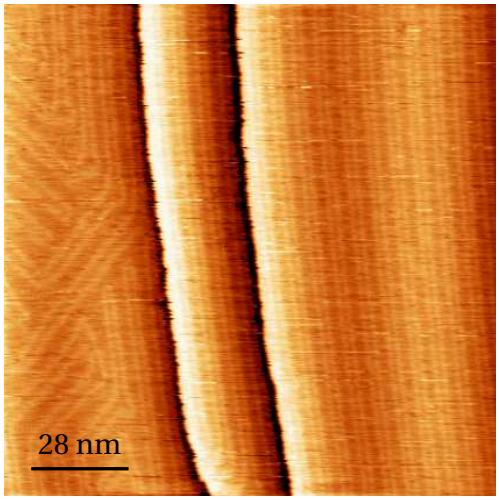

Figure 3.5: STM image of the Au(111) surface after the electrochemical experiments showing a potential-induced reconstruction.

The STM image in Figure 3.2 presents the successful UHV preparation of a clean Au(111) surface with the typical thermally induced herringbone reconstruction. A clean transfer to the EC environment is demonstrated by the characteristic CVs in Figure 3.3 and 3.4. The STM image in Figure 3.5 shows the Au(111) surface with a potential-induced reconstruction, presenting a successful transfer back to UHV after electrochemistry.

3.2.2 STM of PBP-Fe after Electrochemistry

STM characterization of the PBP–Fe network on Au(111) was performed after electrochemistry. Details of the network are given in section 5.2.

In the EC experiment the electrocatalytic activity of the network towards oxygen reduction was studied. The measurements were performed in oxygen saturated 0.1 M NaOH solution. After the EC experiment the sample was removed from the EC cell under potential control at 0.15 V, rinsed with milliQ water and transferred back to UHV in the preparation chamber. Before the STM measurements it was heated to remove most of the residual adsorbates originating from the electrolyte and then cooled down before introducing it in the STM chamber.

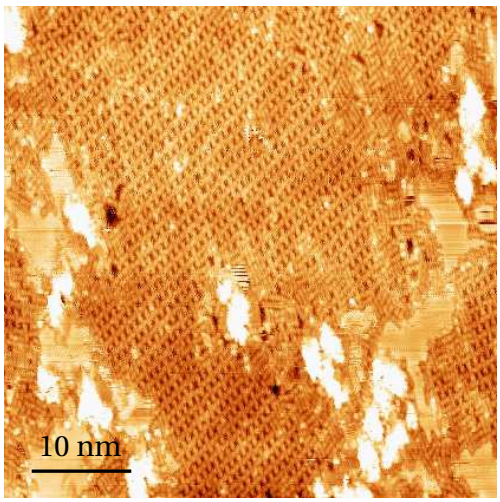

Figure 3.6: STM image of the PBP–Fe network on Au(111) after the electrochemical experiments.

Figure 3.6 shows a large scale STM image of PBP-Fe after EC experiment and is highly representative of the condition of the system. Some agglomerates are present, which are associated with residual adsorbates from the electrolyte. The important point is the presence of long-range two dimensional network domains after the EC experiments. Figure 3.7 compares the structure of the network before the EC experiment to the structure obtained afterwards. The original UHV prepared structure and the one after the liquid environment are nearly identical. This shows that the network not only survives alkaline media but also an electrocatalytic reaction with oxygen.

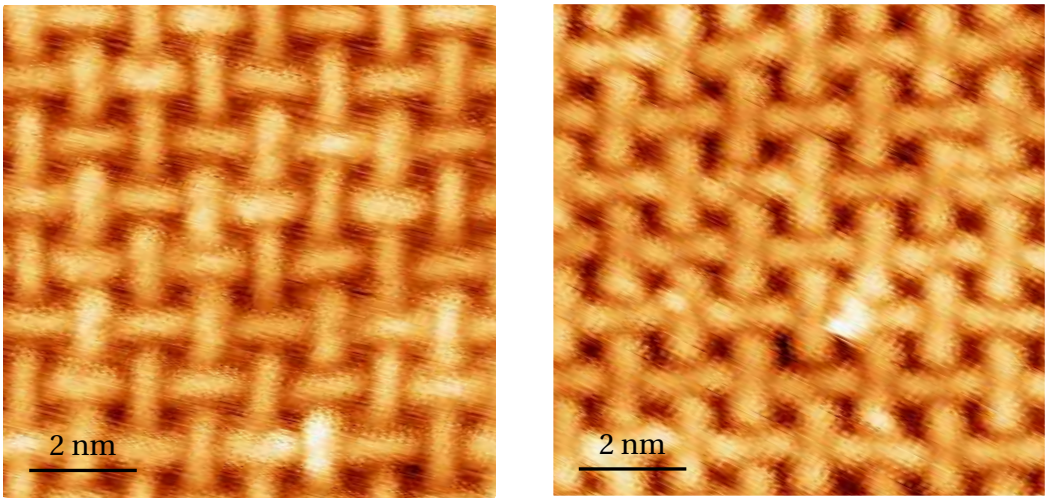

(a) before electrochemistry **(b)** after electrochemistry

Figure 3.7: STM images of the PBP–Fe network on Au(111) showing the network structure (a) before and (b) after the electrochemical experiments.

Chapter 4

Influence on the Catalytic Activity by the Type of the Metal Center

In the first part of this chapter the preparation and STM characterization of a 2D-MOCN composed of benzene-tricarboxylic acid (TMA) and Fe atoms on Au(111) is presented. For this TMA–Fe network, the electrocatalytic activity towards ORR in alkaline media is demonstrated. In the second part the influence on the catalytic activity by the type of the metal center is shown. By replacing Fe with Mn the mechanism of the reduction can be changed.[1]

4.1 TMA–Fe

The network presented in this section consists of TMA and Fe atoms self-assembled on Au(111). Fe atoms coordinated by carboxyl groups were selected to mimic both biological and inorganic catalysts for ORR [60,109]. TMA was chosen because two-dimensional networks of it were previously studied on different single crystal surfaces by STM in UHV and liquid environment [110–114].

The chemical structure of TMA is shown in Figure 4.1a and a ball-and-stick model in Figure 4.1b. TMA adsorbs on Au(111) lying flat with the aromatic ring oriented parallel to the surface and individual molecules appear as triangular features in the

[1] This chapter is based on the paper "Bio-inspired nanocatalysts for the oxygen reduction reaction" given in the publications list.

STM images. The carboxyl groups are located at the corners of the triangles and form intermolecular hydrogen bonds to the neighboring TMA molecules. The result is a porous network with a honeycomb structure, which is shown in Figure 4.1c.

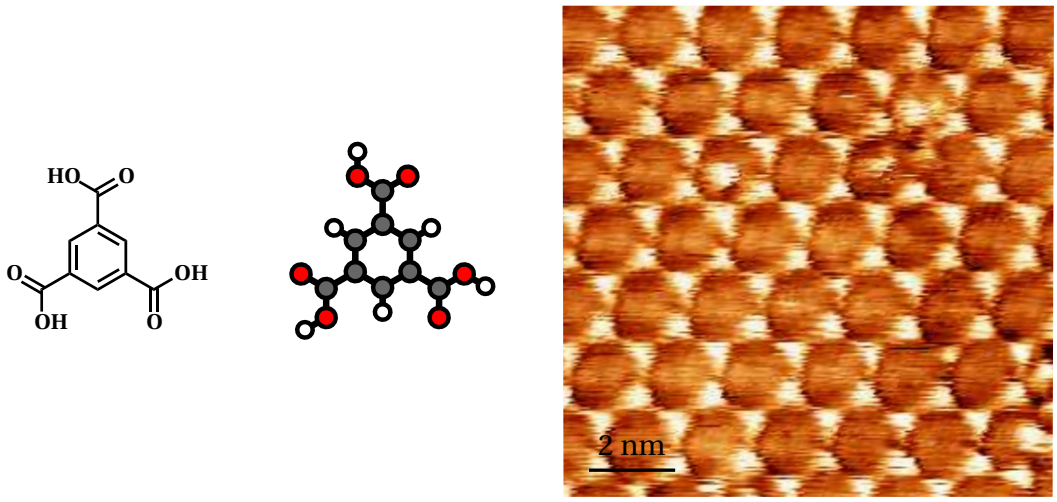

Figure 4.1: (a) chemical structure and (b) ball-and-stick model of TMA. (c) STM image of the honeycomb structure of TMA on Au(111).

To create TMA-Fe networks first TMA was evaporated on the surface held at room temperature and then Fe atoms were deposited on top of the molecular layer. The sample was subsequently annealed to 525 K, favoring deprotonation and binding of the carboxylate groups to the deposited Fe atoms [115]. In contrast, pure TMA layers cannot be annealed higher than 353 K because of desorption of the molecule.

A STM image of the TMA–Fe network on Au(111) is shown in Figure 4.2a. The motif clearly has changed after the incorporation of the Fe atoms; the molecules align in rows with alternating directions. Through comparison to similar system, a structural model has been adapted. The proposed model is overlayed with the high-resolution STM image in Figure 4.2b. Particular regions between the double rows appear brighter and are assigned as the positions of the Fe atoms (cyan circles in Fig. 4.2b). Coordination chains are created where, in each segment, metal dimers are coordinated to four molecules. TMA–Fe networks on other substrates show different arrangements [16, 115, 116]. Here the metal dimers are bridged by two carboxylate groups and each metal atom is coordinated by three oxygen atoms. Adjacent coordination chains are potentially interlinked by carboxyl hydrogen bonds, which require only partial deprotonation of TMA.

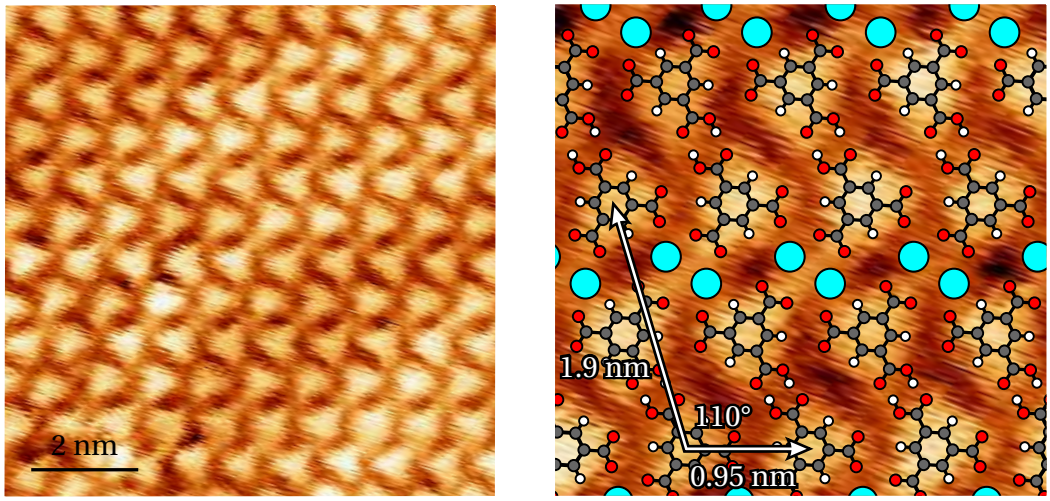

(a) (b)

Figure 4.2: (a) STM image of TMA–Fe network on Au(111). (b) High-resolution STM image of TMA–Fe superimposed with the proposed model (cyan circles represent iron atoms).

Linear sweep voltammetry experiments in O_2 saturated 0.1 M NaOH solution were performed to explore the ability of the networks to reduce O_2 in alkaline media. Figure 4.3 shows the polarization curves for different samples acquired under the same conditions. On bare Au(111) (Fig. 4.3 gray line), a weak shoulder around –0.2 V can be seen corresponding to the reduction of O_2 to H_2O_2 [117, 118]. The reduction occurs on a $2e^-$ pathway according to equation 1.11.

The polarization curve of TMA–Fe (Fig. 4.3 red line) shows a different behavior compared to bare Au(111). The shoulder at –0.2 V has an onset shifted around 0.05 V to lower overpotentials and has a much higher current density (inset Fig. 4.3). More striking is the presence of a second peak around –0.8 V with a large current density. By comparison other Fe-containing systems [119], the second shoulder can be assigned to the electroreduction of H_2O_2 to H_2O according to equation 1.13.

To test this hypothesis, H_2O_2 is added to the solution. In Figure 4.3 the polarization curve of TMA–Fe in presence of 10 mM H_2O_2 (red dotted line) is shown. Two well defined waves at –0.2 and –0.8 V are present, thus confirming the hypothesis. The increase in the current density by adding H_2O_2 can be traced back to an increase of the surface concentration of O_2 due to disproportionation of H_2O_2 in alkaline media [120].

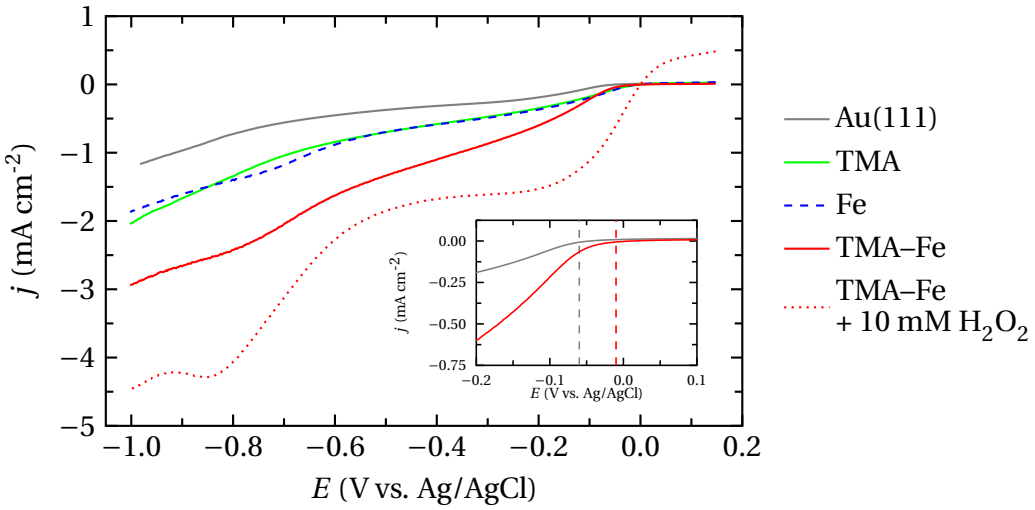

Figure 4.3: Polarization curves in O_2 saturated 0.1 M NaOH solution for different samples, scan rate 50 mV s^{-1}. The inset shows the different onset potentials.

The ability of Fe to reduce O_2 is widely explored in the literature, and several mechanisms were identified yielding H_2O_2 or H_2O as the final product [119, 121–123]. We propose that the first wave around –0.2 V in the polarization curve of TMA–Fe is related to reduction of O_2 to H_2O_2 mediated by both exposed Au surface areas and oxygen atoms present in the network. In fact, the polarization curve of of pure TMA on Au(111) (Fig. 4.3 green line) shows a small enhancement of the current density compared with bare Au(111). In UHV conditions the Fe centers in the network assume an oxidation state close to Fe(II) [54, 124], and Fe(II) can readily bind O_2. However, we do not expect the Fe atoms to participate in the reaction because in the potential window of the first wave between –0.2 and –0.4 V, we assume trivalent metal centers present in the network. It is well established that Fe(III) is not favored as an active site for O_2 reduction [122]. Analyzing the second wave, we consider that Fe(II) species become predominant at potentials more negative than –0.6/–0.7 V. At this potential, Fe(II) can bind both O_2 and H_2O_2 to form OHOH adducts. The strong bonding of H_2O_2 to Fe(II) prevents it from leaving as a two-electron reduction product and provides a path for final reduction to H_2O. The presence of Fe in the TMA networks explains the second wave, and a mechanism combining equations 1.11 and 1.13 is proposed. Blank experiments using the same amount of Fe contained in the networks deposited on Au(111) at room temperature show a similar behaviour as TMA–Fe networks but with substantially reduced catalytic activity (Fig. 4.3 blue dashed line). The Fe is present as small clusters at the elbow sites of the Au(111) herringbone reconstruction.

4.2 TMA–Mn

To study the influence of the metal centers on the catalytic activity Fe was replaced in the network by Mn. The TMA–Mn networks were prepared in the same way as the TMA–Fe except that Mn instead of Fe was evaporated. The structure of the TMA–Mn network, shown in Figure 4.4, is indistinguishable from TMA–Fe. The high-resolution STM image in Figure 4.4b is superimposed with the same model as for TMA–Fe (cf. Fig. 4.2b).

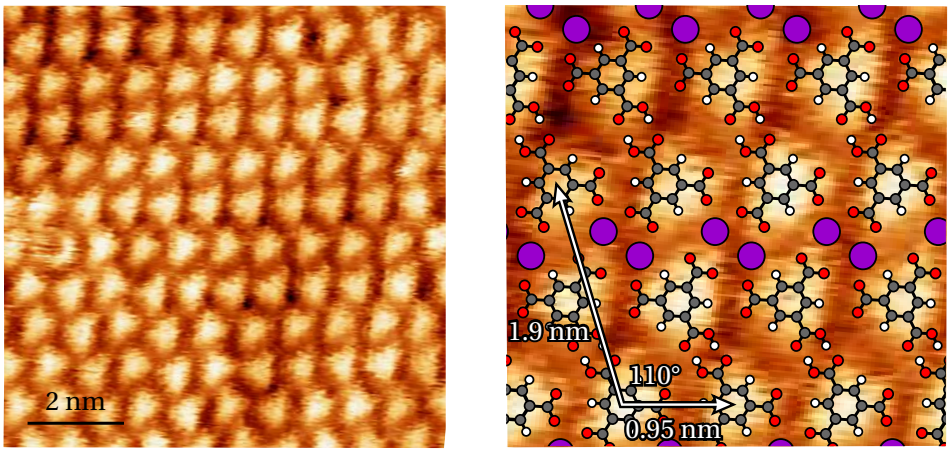

Figure 4.4: (a) STM image of TMA–Mn network on Au(111). (b) High-resolution STM image of TMA–Mn superimposed with the proposed model (purple circles represent manganese atoms).

Despite the structural similarity, the electrochemical signal differs significantly between both networks, showing the key role of the unsaturated metal centers in the electrocatalytic reduction of O_2. Figure 4.5 shows the polarization curve for TMA-Mn (orange line) in O_2 saturated 0.1 M NaOH solution. The first wave is better defined, shifted to a lower potential of –0.15 V and presents a higher current density. Additionally the onset potential is shifted around 0.1 V (compared to Au(111)) to even lower overpotentials (inset Fig. 4.5). Moreover, the wave at –0.8 V found in TMA–Fe ORR polarization curve is not present for the TMA–Mn network. A possible reason could be that the potential reduction of small amounts of the generated H_2O_2 is obscured by the onset of the hydrogen evolution reaction. However, adding H_2O_2 to the solution does not produce any change in the shape of the polarization curve (Fig. 4.5 orange dotted line), indicating that no H_2O_2electroreduction occurs. Again we find an increase in the current density by adding H_2O_2 due to disproportionation of H_2O_2

in alkaline media [120], as in the case of TMA–Fe. Hence, we conclude that TMA–Mn reduces O_2 directly to H_2O through a $4e^-$ pathway ,according to equation 1.10. It is important to point out that Mn oxides catalyze the O_2 reduction mainly via a $(2+2)e^-$ pathway [125], while Mn coordination compounds directly reduce O_2 to H_2O via a $4e^-$ mechanism [126]. Similar to Fe on Au(111), the polarization curves for Mn clusters on Au(111) (Fig. 4.5 violet line) show a similar profile as TMA–Mn with clearly lower catalytic current density. This result emphasizes the importance of the complexation of the metal atoms and hints at the tremendous potential of this approach. The chemical activity of the metal centers is determined by both the nature of the metal ion and its coordination shell. In addition, the ligation separates the unsaturated metal atoms preventing catalytic deactivation [52].

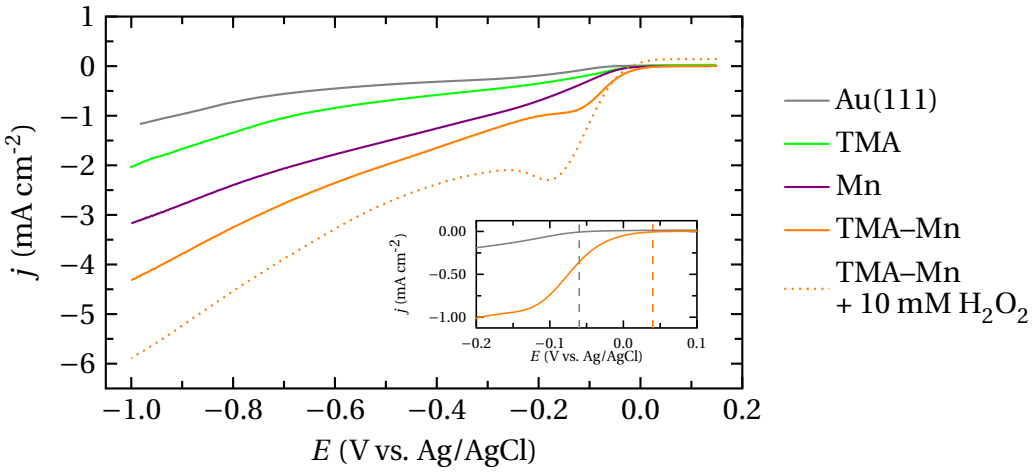

Figure 4.5: Polarization curves in O_2 saturated 0.1 M NaOH solution for different samples, scan rate 50 mV s^{-1}. The inset shows the different onset potentials.

4.3 Conclusions

Catalytic activity of UHV prepared 2D-MOCNs was demonstrated for the first time. TMA–Fe and TMA–Mn on Au(111) catalyze the complete O_2 reduction towards H_2O and moreover that the mechanism can be influenced by the choice of the metal center. While TMA–Fe exhibit an indirect $(2+2)e^-$ pathway with intermediate H_2O_2, TMA–Mn reduces O_2 directly to H_2O on a $4e^-$ pathway. This provides a proof of concept that surface-engineered metal–organic complexes and networks that display structural resemblance to enzyme active sites have a high potential for heterogeneous catalytic chemical conversions.

Chapter 5

Ligand Effect on the Electrocatalytic Response

In this chapter the electrocatalytic response in the ORR of single Fe atoms coordinated by either tetracyanoquinodimethane (TCNQ), bis-pyridyl-bipyrimidine (PBP) or phythalocyanine (Pc) on Au(111) is presented. Linear sweep voltammetry experiments in alkaline media demonstrate that the final product and the mechanism of the reduction of O_2 can be changed by the specific coordination environment of Fe. In all three cases the coordination environment of Fe is formed by nitrogen atoms, but different ligands with distinct functional groups are used.[1]

5.1 TCNQ–Fe

The chemical structure of TCNQ and a ball-and-stick model is shown in Figure 5.1. TCNQ was evaporated on the Au(111) surface held at room temperature. The molecules physisorb on Au(111) ina flat lying geometry with the aromatic ring parallel to the surface and form highly ordered self-assembled domains by intermolecular C≡N···H−C hydrogen bonds [127]. A STM image of the molecular phase is shown in Figure 5.2.

[1] Parts of this chapter are based on the paper "Bio-inspired nanocatalysts for the oxygen reduction reaction" given in the publications list.

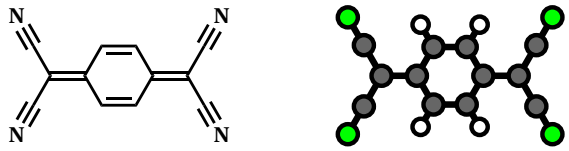

Figure 5.1: (a) Chemical structure of 7,7,8,8-tetracyanoquinodimethane and (b) ball-and-stick model.

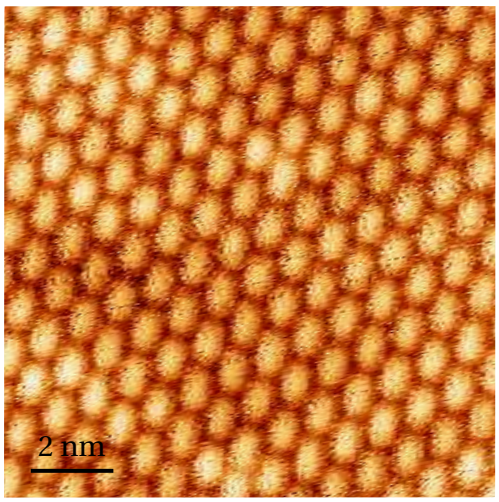

Figure 5.2: STM image of the self-assembled molecular layer of TCNQ on Au(111).

TCNQ is well known to from coordination structures with different metal atoms in 3D [128–130] and 2D [131–133]. Fe atoms were deposited on top of the molecular layer with the substrate held at room temperature and subsequently the sample was annealed to 353 K. A STM image of the resulting TCNQ–Fe network is shown in Figure 5.3a. In the observed network the stoichiometry of TCNQ:Fe is 1:1 and the structure is similar to networks of TCNQ with Mn or Ni on Au(111) [133]. Each TNCQ molecule binds with the cyano groups to four Fe atoms and each Fe atom is four-fold coordinated by cyano groups. The proposed model is overlayed with the high-resolution STM image in Figure 5.3b.

The ability of this network to reduce O_2 in alkaline media was explored by performing linear sweep voltammetry experiments in O_2 saturated 0.1 M NaOH solution. The obtained polarization curves are shown in Figure 5.4. As discussed in Section 4.1 for bare Au(111) (Fig. 5.4 gray line) a weak shoulder around –0.2 V can be seen, corresponding to the reduction of O_2 to H_2O_2 on a $2e^-$ pathway (Eq. 1.11) [117, 118]. TCNQ–Fe (Fig. 5.4 red line) shows a similar profile as bare Au(111) with the same

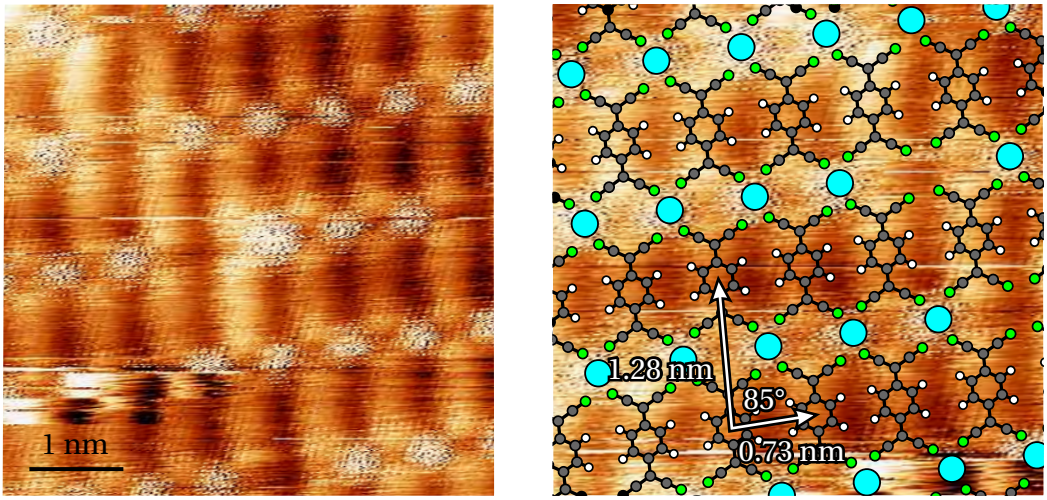

Figure 5.3: (a) STM image of TCNQ–Fe on Au(111). (b) High-resolution STM image of TCNQ–Fe superimposed with the proposed model (cyan circles represent iron atoms).

onset potential (inset Fig. 5.4). The current density is somewhat higher, showing a slightly increased catalytic activity. Unlike TMA–Fe (Sec. 4.1) and PBP–Fe (Sec. 5.2) no second peak is observed, which leads to the conclusion that no reduction of the generated H_2O_2 occurs in the examined potential window. Thus TCNQ–Fe reduces O_2 to H_2O_2 on a $2e^-$ pathway according to equation 1.11.

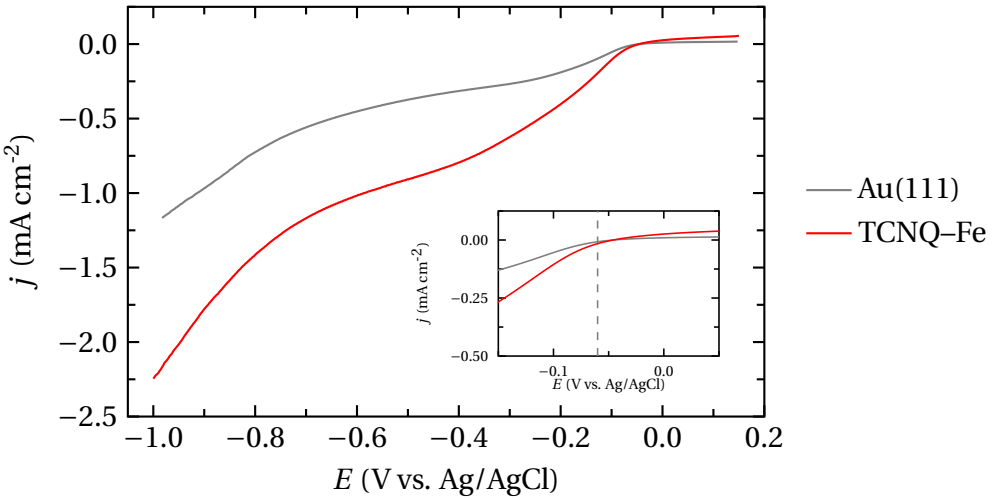

Figure 5.4: Polarization curves in O_2 saturated 0.1 M NaOH solution for TCNQ–Fe, scan rate 50 mV s^{-1}. The inset shows the onset potential.

In enzymatic ORR catalysts nature uses molecules with electron donating functional groups that prevent the formation and release of detrimental partially reduced oxy-

gen by-products and intermediates [134]. The cyano groups of TCNQ, in contrast, are strong electron withdrawing groups and TCNQ is a well-known electron acceptor. Charge transfer from the metal center to TCNQ is observed for the TCNQ–Ni network on Au(111) [133]. In the TCNQ–Fe network the cyano groups withdraw so much electron density from the Fe centers, that Fe(III) is most likely the dominant species even at negative potentials. As discussed in section 4.1 Fe(III) is not favored as an active site for O_2 reduction [122]. H_2O_2 binds weakly to Fe(III) and leaves as the two-electron reduction product [122]. In contrast to TMA–Fe and PBP–Fe no path for final reduction to H_2O is provided and, thus, the second wave in the polarization curve is absent.

5.2 PBP–Fe

The chemical structure and a ball-and-stick model of PBP is shown in Figure 5.5. 2D metal-organic networks of PBP have been reported on Ag and Cu surfaces but not on Au(111) [135]. PBP was evaporated on the Au(111) surface held at room temperature. A STM image of the molecular phase of PBP on Au(111) is shown in Figure 5.6. On Au(111), PBP adsorbs in a flat geometry with the aromatic rings parallel to the surface. A lamellar structure is observed with the molecules oriented parallel and aligned in rows. The pyrimidine groups are adjacent to each other and the pyridyl end groups form hydrogen bonds resulting in a skewed structure. The molecular tilt results in a closer proximity and better alignment of the N-functional groups. Similar structures were observed with the pyridyl benzoic acid molecule assembled on Ag(111) [18] and PBP on Ag(100) [135].

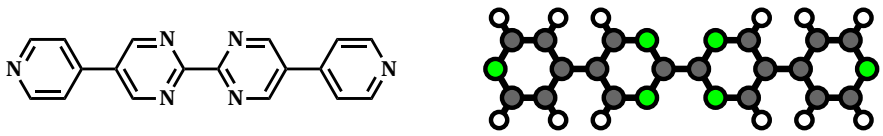

(a) **(b)**

Figure 5.5: (a) Chemical structure of 5,5'-bis(4-pyridyl)(2,2'-bipyrimidine) and (b) ball-and-stick model.

The sample was heated up to 413 K and then Fe atoms were deposited on top of the molecular layer at elevated temperature. The incorporation of Fe leads to a network structure, which is comparable to the networks formed on Cu and Ag surfaces

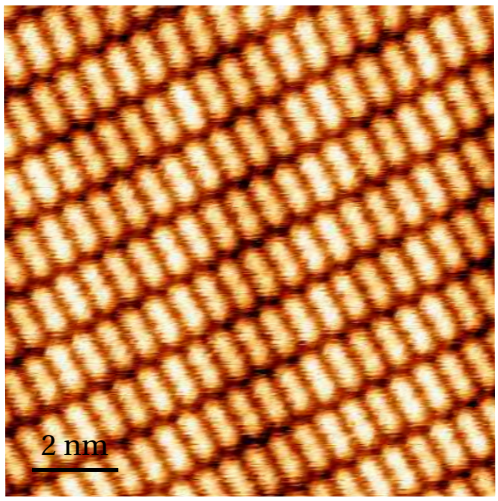

Figure 5.6: STM image of the self-assembled molecular layer of PBP on Au(111).

using Cu adatoms [135]. Figure 5.7a shows a STM image of PBP–Fe on Au(111). A high-resolution STM image and the proposed model are presented in Figure 5.7b. In this network, each molecule coordinates to four Fe adatoms via the pyrimidine and pyridyl groups fully saturating the molecule's binding sites. Hence, each Fe adatom binds to three nitrogen atoms of the two central pyrimidine units of a PBP molecule and to the pyridyl moiety of a neighbouring PBP ligand.

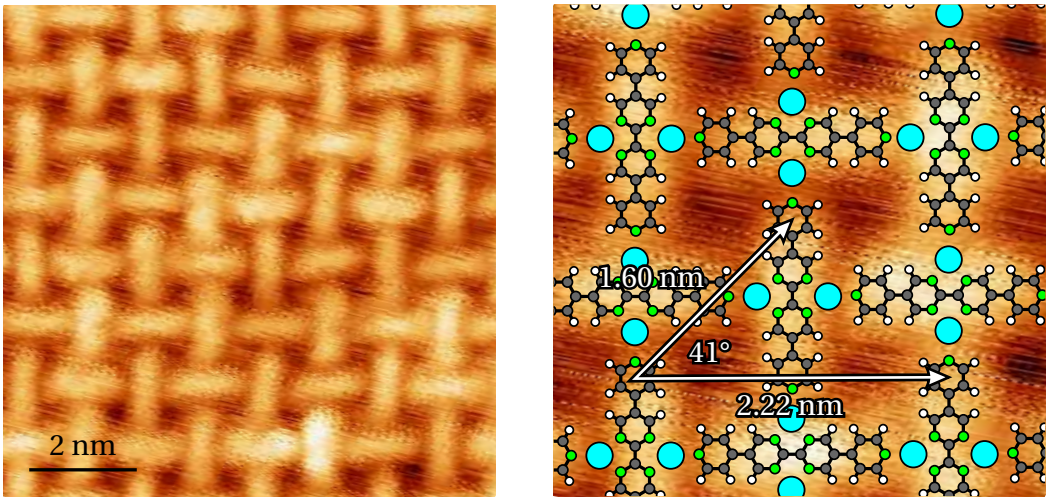

(a) **(b)**

Figure 5.7: (a) STM image of PBP–Fe on Au(111). (b) High-resolution STM image of PBP–Fe superimposed with the proposed model (cyan circles represent iron atoms).

The polarization curve for PBP–Fe in a O_2 saturated 0.1 M NaOH solution is shown in Figure 5.8. The electrocatalytic response differs from bare Au(111) and TCNQ–Fe

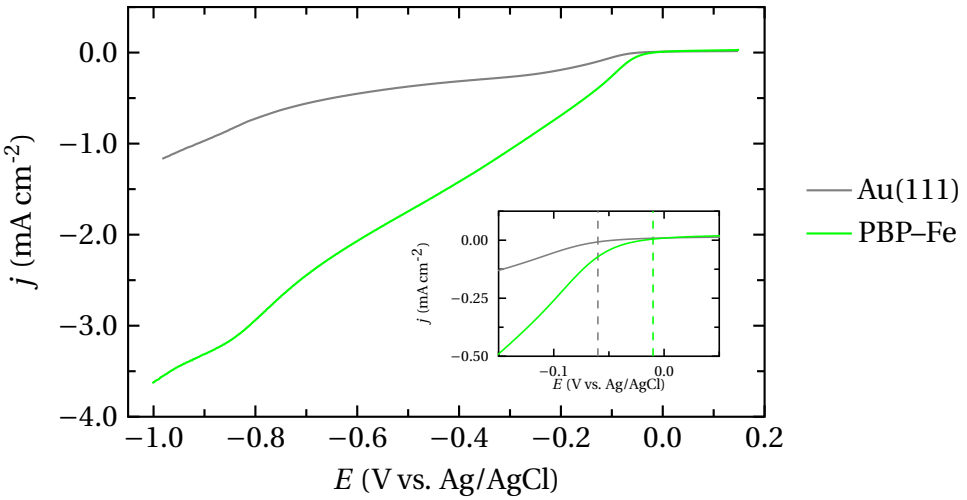

Figure 5.8: Polarization curves in O_2 saturated 0.1 M NaOH solution for PBP–Fe, scan rate 50 mV s^{-1}. The inset shows the different onset potentials.

(Fig. 5.4); the current density is higher, the onset of the shoulder at –0.2 V is shifted around 0.05 V to lower overpotentials (inset Fig. 5.8) and a second peak around –0.85 V is present. This profile is similar to TMA–Fe (Fig. 4.3) but with a somewhat larger catalytic current. By comparison with the TMA–Fe and other Fe-containing systems [119], the second shoulder can be assigned to the electroreduction of H_2O_2 to H_2O according to equation 1.13. Hence we conclude PBP–Fe catalyzes the complete reduction of O_2 to H_2O via an indirect $(2+2)e^-$ mechanism with intermediate H_2O_2 combining equations 1.11 and 1.13.

Compared to TCNQ the pyrimidine and pyridyl groups of PBP provide much more electron density to the Fe atoms. However, we assume in the potential window of the first wave trivalent metal centers present in the network. At potential more negative than –0.65/–0.75 V the Fe(II) species become predominant. The strong bonding of H_2O_2 to Fe(II) prevents it from leaving as a two-electron reduction product and provides a path for final reduction to H_2O. This behavior is really similar to TMA–Fe (Section 4.1), but the position of the second peak is shifted to more negative potentials for PBP–Fe (–0.85 V) compared to TMA–Fe (–0.80 V). This could be a result of the distinct coordination environment shifting the Fe(II)/(III) redox potential towards more negative potentials.

STM images of the PBP-Fe network after the electrochemical experiments are shown in section 3.2.2. A nearly identical structure was found after the liquid environment compared to the UHV-prepared network (Fig. 3.7).

5.3 FePc

The chemical structure and a ball-and-stick model of iron(II) phthalocyanine (FePc) is shown in Figure 5.9. FePc was evaporated onto the Au(111) surface held at room temperature and subsequently annealed to 353 K. The resulting FePc monolayer on Au(111) is shown in Figure 5.10. FePc adsorbs flat lying on the surface and individual molecules are imaged by STM as a four-lobed shape with a protrusion at the center, corresponding to the aromatic macrocycle and central metal atom, respectively. At monolayer coverage, FePc forms a densely packed ordered layer with an almost quadratic unit cell on Au(111) (Fig. 5.10b) [136–138]. In Figure 5.10a a domain boundary between two orientation-domains in the FePc monolayer can be seen. In Figure 5.10b the STM image is overlayed with the model.

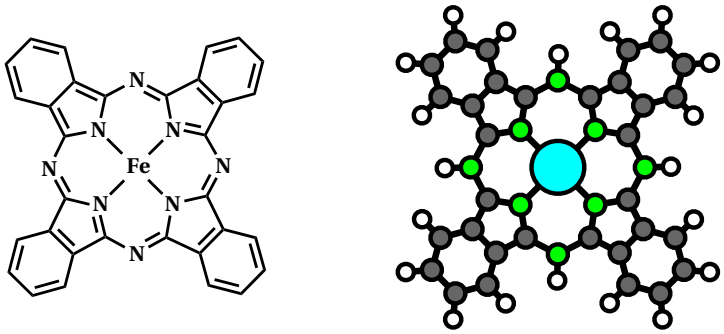

Figure 5.9: (a) Chemical structure and (b) ball-and-stick model of iron(II) phthalocyanine.

Figure 5.11 shows the polarization curve for FePc in an O_2 saturated 0.1 M NaOH solution, which also shows a different behavior compared to bare Au(111), TCNQ–Fe and PBP–Fe. The first wave is much more defined, shifted to a lower potential of –0.06 V and presents a higher current density. The onset potential of the first wave is shifted around 0.08 V (compared to Au(111)) to lower overpotentials. Like in the case of TMA–Mn (Sec. 4.2) we assign this peak to the direct reduction of O_2 to H_2O on a $4e^-$ mechanism according to equation 1.10. FePc is well known to catalyze the ORR in alkaline media via a $4e^-$ pathway on different supports [139–142].

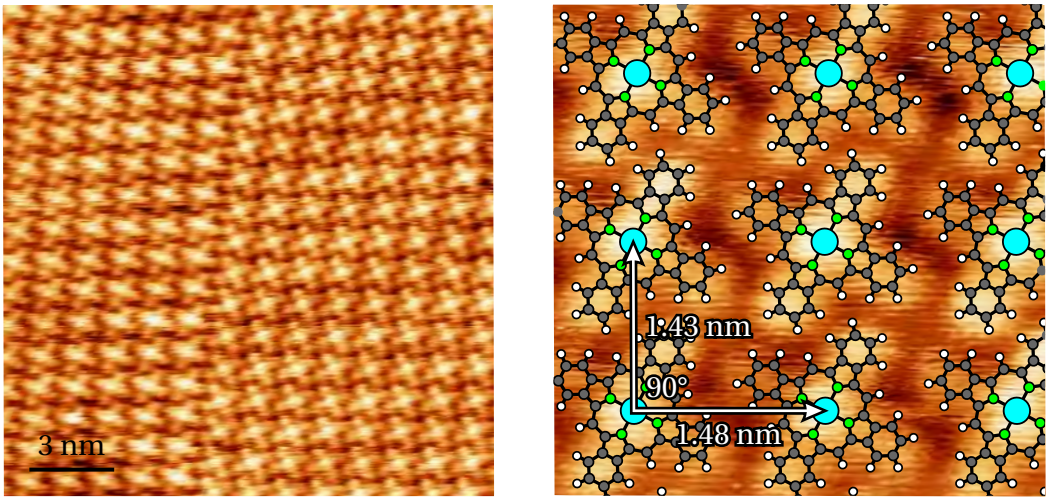

Figure 5.10: (a) STM image of FePc on Au(111). (b) High-resolution STM image of FePc superimposed with model.

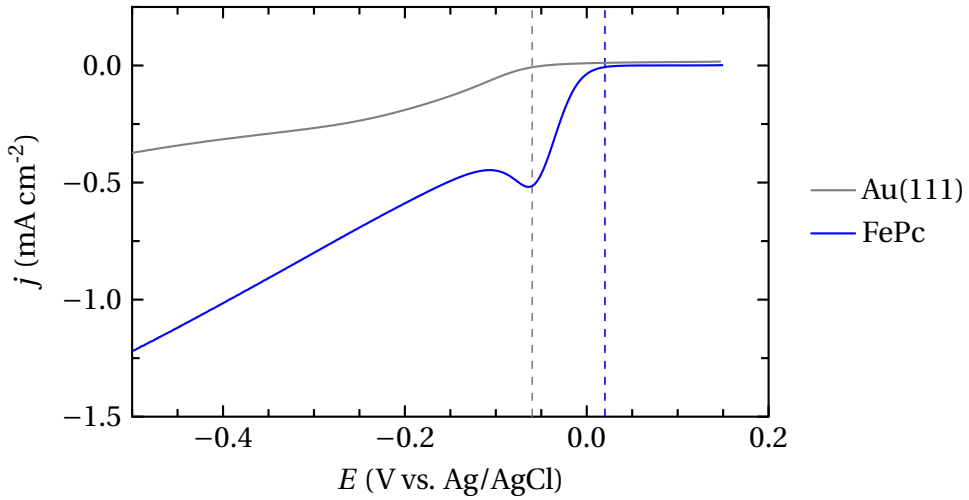

Figure 5.11: Polarization curves in oxygen saturated 0.1 M NaOH solution for FePc, scan rate 50 mV s^{-1}.

FePc shows the highest catalytic activity and the lowest onset potential, compared to TCNQ–Fe and PBP–Fe. This could be due to a much higher electron density on the Fe centers provided by the π-electron rich macrocycle favoring the catalytic active Fe(II) species. The Fe(III)/Fe(II) transition for FePc is very close to the onset potential of O_2 reduction [143, 144]. In PBP–Fe and FePc different functional groups are utilized; in PBP–Fe pyridyl and pyrimidine (pyridyl related) groups coordinate Fe, in FePc the metal atoms are embedded in a porphyrazin ring. Pyridinic and porphyrazin-type

species are both important coordination groups in the formation of active sites in Fe/N/C materials [66]. Porphyrazines form a square planar coordination environment. For pyridinic species in Fe/N/C materials also a fourfold planar coordination geometry is proposed and the direct $4e^-$ ORR pathway is observed in alkaline media [69, 145, 146]. In contrast PBP–Fe has a threefold coordination environment and shows a $(2+2)e^-$ pathway. This might be a result of the different ligand geometries; the ligand field can alter the energetic arrangement of the d-orbitals of the Fe centers [147], which could modify the interaction with oxygen and reaction intermediates. To evaluate this geometric aspect, a MOCN with a fourfold pyridinic coordination environment for Fe could be studied. Moreover, density functional theory (DFT) calculations are needed to get further insight in the electronic configuration of the metal centers and to evaluate binding energies with oxygen and reaction intermediates.

5.4 Conclusions

The electrocatalytic response in the ORR for three iron-based two-dimensional metal-organic structures on Au(111) was shown. The differences in the electrocatalytic activity might be a result of the electron density on the Fe centers in the distinct coordination environment and its geometry. TCNQ is a strong electron acceptor and withdraws electron density from the Fe atoms. For TCNQ–Fe, only the reduction towards H_2O_2 on a $2e^-$ pathway is observed. In PBP–Fe and FePc the coordinating groups provide much more electron density to the Fe centers and the complete reduction to H_2O is observed. PBP–Fe catalyzes the reduction of O_2 via an indirect $(2+2)e^-$ pathway with intermediate H_2O_2, while FePc catalyzes directly to H_2O by a $4e^-$ pathway. The π-electron rich macrocycle favors the catalytic active Fe(II) species. For the catalytic activity also the geometry of the coordination environment might play a role, since the ligand field can alter the energetic arrangement of the d-orbitals of the Fe centers.

These results emphasize how the catalytic activity can be influenced by the specific coordination environment of the Fe atoms. In all three cases, Fe is coordinated to nitrogen atoms, but the distinct ligands, functional groups and coordination geometry change the final product and the mechanism of the reduction. This shows the power of our approach; engineering of the metal-organic complexes and networks

by choosing different ligands and functional groups allows the complete control of the coordination environment and, by this, the tuning of the catalytic activity of the embedded metal centers.

Chapter 6

Cooperative Bimetallic Effect

In this chapter the two metal-binding sites of 5,10,15,20-tetra(4-pyridyl)porphyrin (TPyP) are used to selectively incorporate different metal centers in a fixed organic environment and create homo- and hetero-bimetallic networks. In section 6.1 the STM characterization of the prepared samples is shown. The effect on the ORR from combining different metals is presented in section 6.2. A non-lineary increased catalytic activity towards the evolution of oxygen is demonstrated in section 6.3. [1]

6.1 Scanning tunneling microscopy

The samples were prepared by sublimation of TPyP containing either no or one metal atom (M^1) in the porphyrin macrocycle onto Au(111) with the sample held at 520 K (Figure 6.2 and 6.3). A chlorine ligand is present at the central metal in the cases of Fe and Co. At this substrate temperature, the chlorine atom on FeTPyP and CoTPyP likely detaches from the molecule and desorbs, converting M(III) into catalytically active M(II) [148]. The second metal (M^2) was sublimed in an additional step and is coordinated by the pyridyl groups in a four-fold geometry (Figure 6.1a). This method allows the preparation of highly ordered layers of M^1TPyP(-M^2) and provides control over the exact position of the different metal centers within the network.

[1] Parts of this chapter are based on the paper "Driving the oxygen evolution reaction by nonlinear cooperativety in bimetallic coordination networks" given in the publications list.

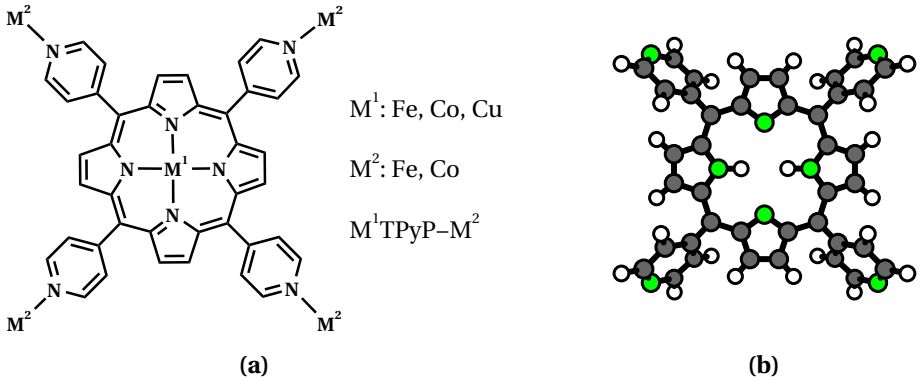

Figure 6.1: (a) Chemical structure of 5,10,15,20-tetra(4-pyridyl)porphyrin (TPyP) with the two different metal binding sites and (b) ball-and-stick model of the free-base porphyrin (H_2TPyP).

The chemical structure of TPyP with the two different metal binding sites and a ball-and-stick model of the free-base porphyrin (H_2TPyP) is shown in Figure 6.1. STM images of H_2TPyP on Au(111) (Fig.6.2) were initially used to analyze the changes due to the presence of the central and then periphery metal centers M^1 (Fig. 6.3) and M^2 (Fig. 6.5) respectively.

Figure 6.2a shows an STM image of a highly ordered layer of H_2TPyP on Au(111). H_2TPyP absorbs with the porphyrin macrocycle parallel to the surface and the pyridyl groups are rotated out of the porphyrin plane [149]. The porphyrin core is clearly visible with a depression in the center due to the absence of a central metal atom, and the four terminal pyridyl groups appear as bright protrusions in a rectangular arrangement. These intramolecular features make it possible to determine the orientation of the molecules, allowing the development of a meaningful model, which is overlayed with the STM picture in Figure6.2b. The molecules arrange in rows whereby adjacent rows are slightly shifted with respect to each other forming an oblique lattice. Neighboring molecules are rotated by 90° against each other.

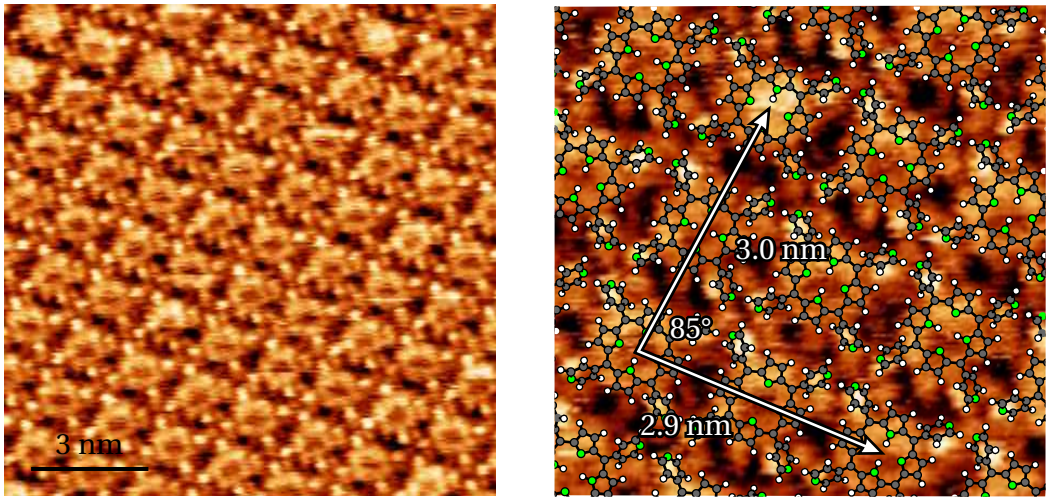

Figure 6.2: (a) STM image of H_2TPyP on Au(111). (b) High-resolution STM image of H_2TPyP superimposed with the proposed model.

STM images of FeTPyP, CoTPyP and CuTPyP adsorbed on Au(111) are shown in Figure 6.3 and slight differences in the metallo-porphyrin monolayers compared to the metal free porphyrin are apparent. The presence of M^1 does not affect the molecular packing on the surface, which is similarly reported for TPyP and FeTPyP on Ag(111) [150]. The dark depression within the macrocycle of H_2TPyP is replaced by a bright protrusion for FeTPyP and CoTPyP (Fig. 6.3a and 6.3c), which is attributed to the central metal atom M^1. The tunneling enhancement through the half-filled metal d_{z2} orbital is known for cobalt tetraphenylporphyrin (CoTPP) [151] and for FePc and CoPc [152, 153]. In the case of CuTPyP (Fig.6.3e) the metal center can be imaged as a depression in STM, which is also reported for CuPc [153], NiPc [152] and NiTPP [151] and due to the filled d_{z^2} orbital of Cu and Ni.

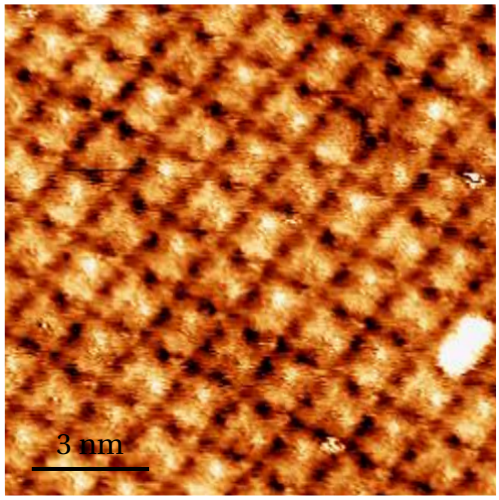

(a) FeTPyP

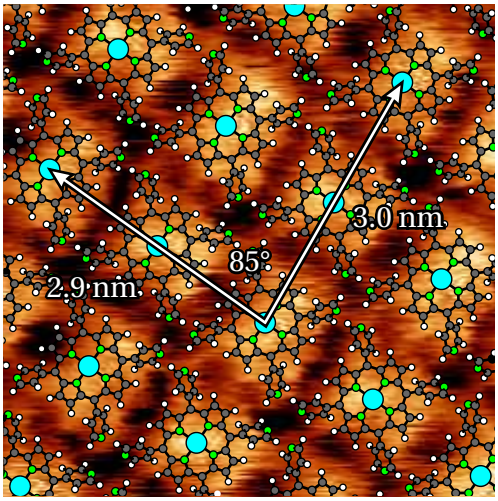

(b) FeTPyP

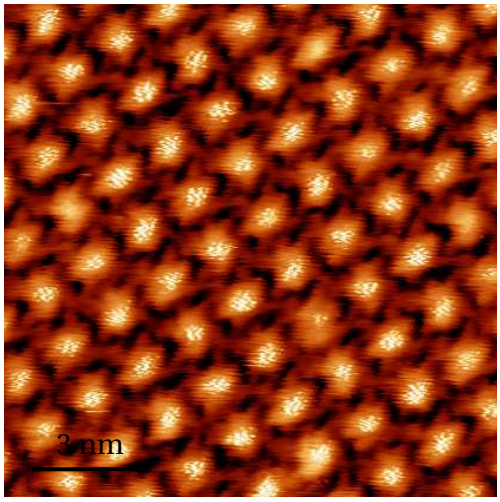

(c) CoTPyP

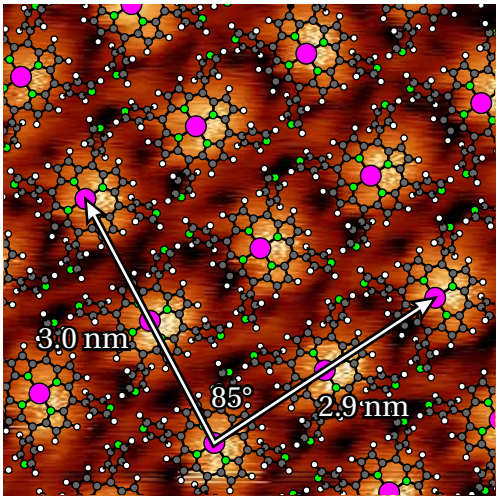

(d) CoTPyP

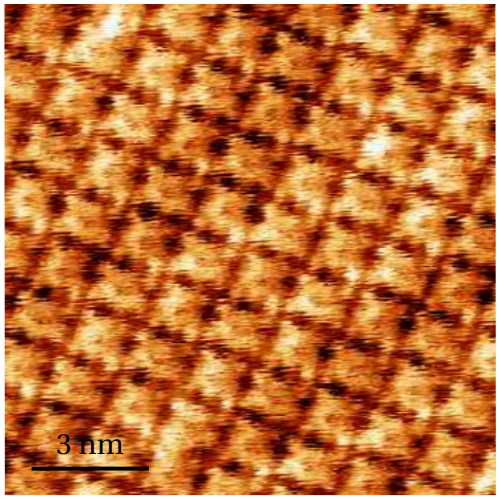

(e) CuTPyP

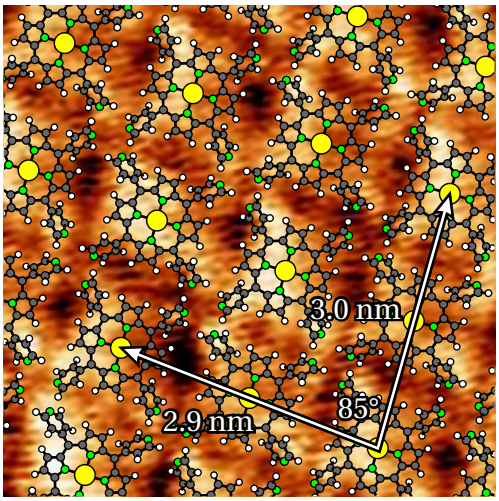

(f) CuTPyP

Figure 6.3: STM images of highly ordered layers of M[1]TPyP on Au(111). (b), (d) and (f) superimposed with the proposed model. Fe (cyan), Co (magenta), Cu (yellow).

After incorporation of the second metal M^2 the molecular packing slightly changes. The second metal is coordinated by four pyridyl groups between the molecules, which leads to a rectangular arrangement of the molecular rows. The position of M^2 can be revealed with a modified tip (Fig.6.4a). The STM image in Figure 6.4b is overlayed with the proposed model. All bimetallic networks (M^1TPyP–M^2) with different metal combinations show the same arrangement of the molecules, which is shown in the STM pictures in Figure 6.5 and indicats the negligible influence of the type of metal on the self-assembly process.

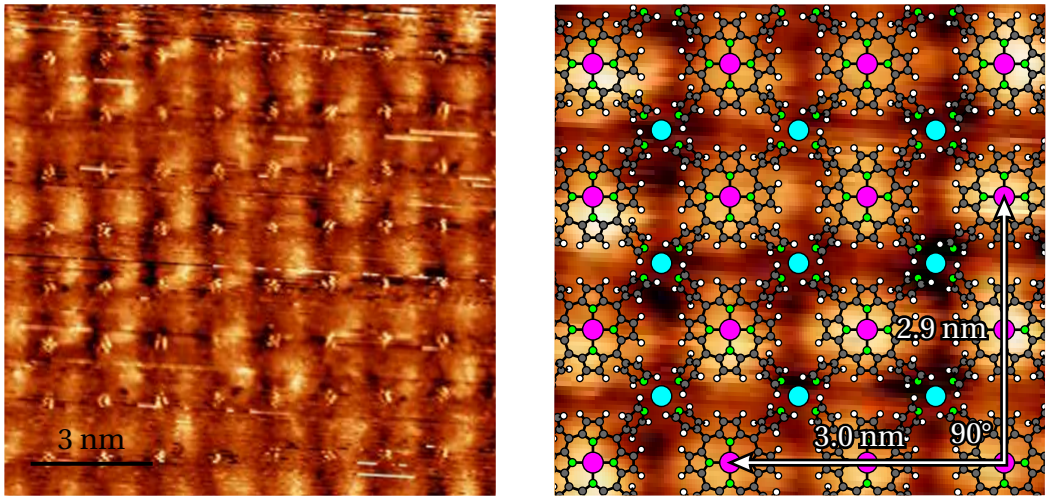

(a) CoTPyP–Fe **(b)** CoTPyP–Fe

Figure 6.4: (a) STM image of CoTPyP–Fe on Au(111) with a modified tip revealing the position of M^2. (b) High-resolution STM image of CoTPyP–Fe superimposed with the proposed model. Color legend: Fe (cyan), Co (magenta).

Distances between metal centers were found to be 14.5 Å for M^1–M^1 and M^2–M^2, and 10.4 Å for M^1–M^2. In biological catalyst systems and analogues inorganic catalysts, the distances between bimetallic centers varying from 2 to 20 Å, enabling cooperative effects in catalysis through geometric proximity or changes in the coordination sphere [154, 155]. In the following, the catalytic properties towards ORR and OER of the 2D bimetallic structures are investigated with focus on the influence of the combination of two different metal centers.

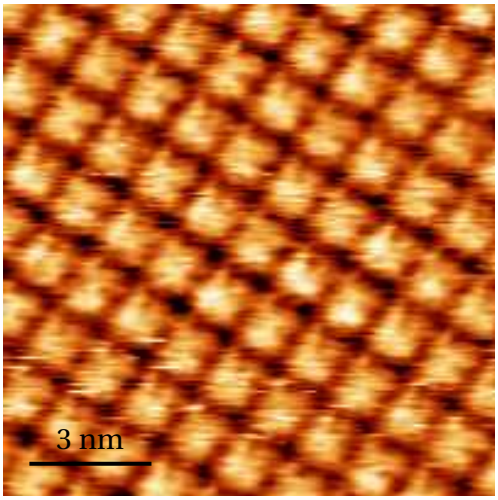

(a) FeTPyP–Fe

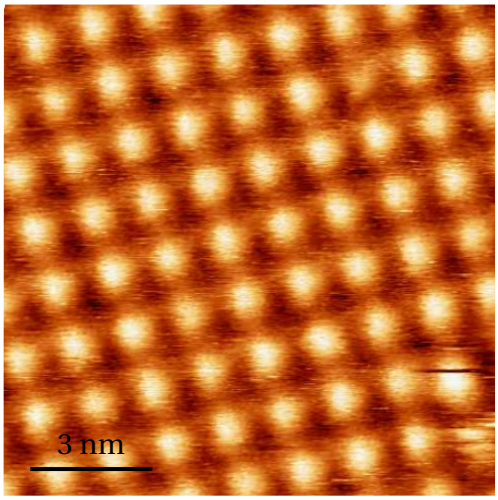

(b) FeTPyP–Co

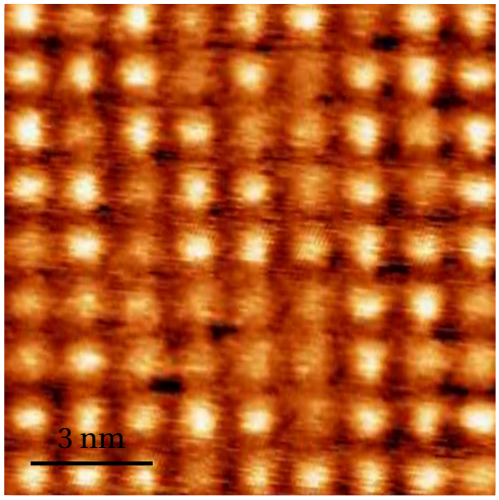

(c) CoTPyP–Fe

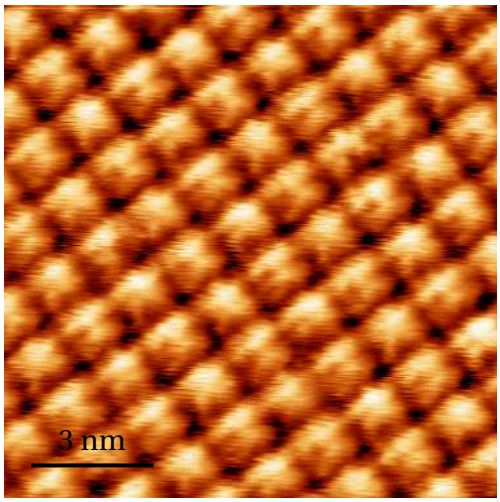

(d) CoTPyP–Co

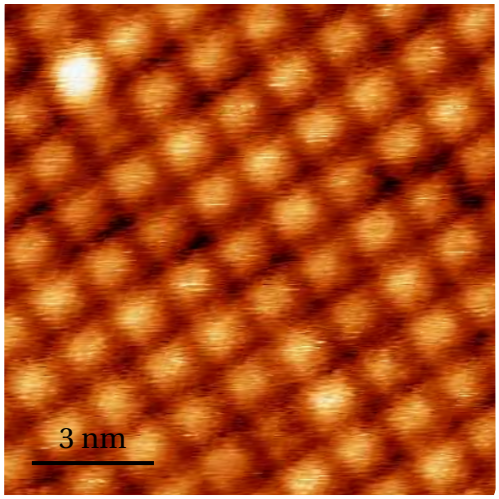

(e) CuTPyP–Fe

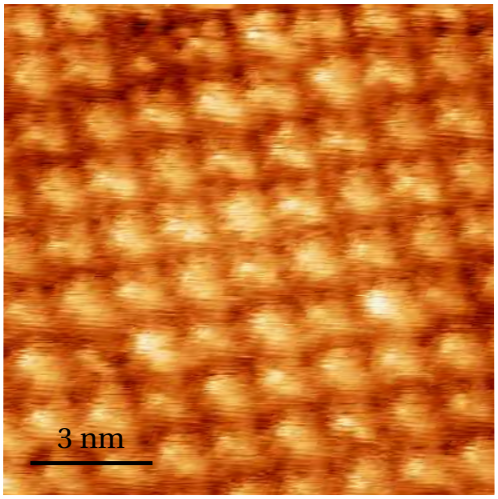

(f) CuTPyP–Co

Figure 6.5: STM images of highly ordered homo- and hetero-bimetallic networks M^1TPyP–M^2 on Au(111) showing all the same arrangement of molecules.

6.2 Oxygen Reduction Reaction

The catalytic activities towards the ORR of the different molecular networks were studied. Figure 6.6 shows the polarization curves in oxygen saturated 0.1 M NaOH solution. For bare Au(111) (Fig. 6.6 gray line) a weak shoulder around –0.2 V can be seen corresponding to the reduction of O_2 to H_2O_2 [117,118]. The polarization curve of the metal-free porphyrin H_2TPyP (Fig. 6.6 dashed line) and CuTPyP (Fig. 6.6a green line) have similar profiles to the Au(111) case, but for H_2TPyP it is shifted towards more negative potentials. All other networks show an enhanced catalytic activity. The po-

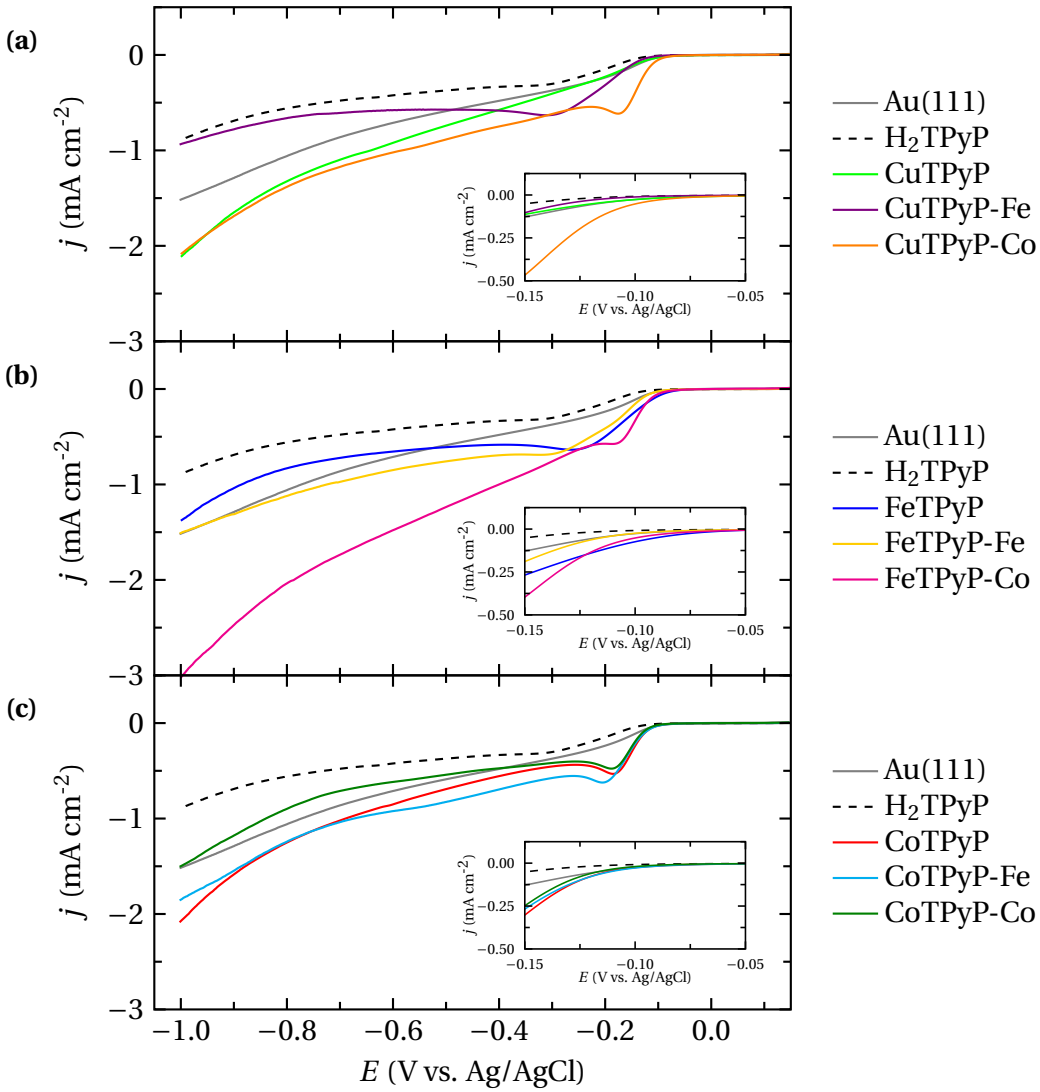

Figure 6.6: Polarization curves in oxygen saturated 0.1 M NaOH solution for different networks, scan rate 50 mV s^{-1}.

larization curve of FeTPyP (Fig.6.6b blue line) has a broad peak around –0.26 V and the lowest onset potential of all samples. In case of CoTPyP (Fig. 6.6c red line) the peak is much more defined and located at a lower overpotential (–0.18 V), but compared to FeTPyP the onset is shifted to a larger overpotential. The presence of a second metal alters the peak position and the onset potential. The maximum change in the onset potential is below 0.05 V, whereas the peak potential is varied in a range of around 0.15 V. The incorporation of Fe as the second metal leads to an adverse shift of the peak position towards more negative potentials. Compared to FeTPyP in the polarization curve of FeTPyP–Fe (Fig. 6.6b yellow line) and CuTPyP–Fe (Fig. 6.6a violet line) the peak potential and the onset potential are shifted to higher overpotentials. Co as the second metal, on the other hand, leads for FeTPyP–Co (Fig. 6.6b magenta line) and CuTPyP–Co (Fig. 6.6a orange line) to a beneficial shift of the peak position towards lower overpotentials and the onset potential is only slightly higher compared to FeTPyP. The effect of the second metal for CoTPyP is comparatively small. The onset potentials of CoTPyP–Fe (Fig. 6.6c cyan line) and CoTPyP–Co (Fig. 6.6c dark green line) are negligibly lower or higher compared to CoTPyP. The peak position of CoTPyP-Co is almost equal to CoTPyP, but for CoTPyP–Fe it is slightly more negative
.

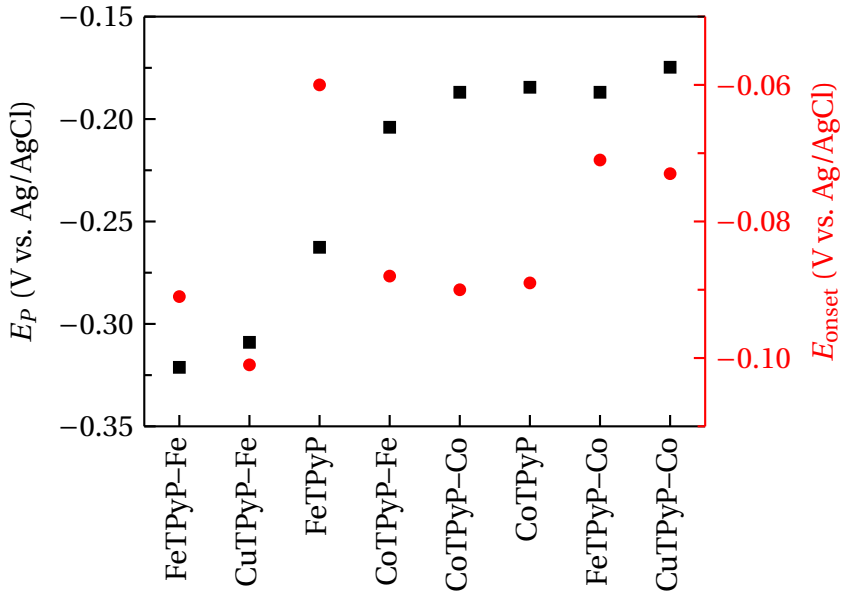

Figure 6.7: Comparison of the peak potential E_P (black squares) and onset potential E_{onset} (red circles) for different samples extracted from Figure 6.6. CuTPyP is omitted since it showed a clearly different catalytic behavior.

For easier comparison of the catalytic activities, the peak potential and the onset potential of the different samples are extracted from Figure 6.6 and presented in Figure 6.7. The samples are ordered from most to least negative peak potentials. FeTPyP–Fe and CuTPyP–Fe shows the lowest catalytic activity, with the most negative peak position and highest onset potential. FeTPyP shows the lowest onset potential, but the peak potential has a higher overpotential than the Co containing samples. The catalytic activities of CoTPyP–Co and CoTPyP are nearly identical and slightly superior to CoTPyP–Fe, which has a somewhat higher peak potential. The best catalytic activities are observed for FeTPyP–Co and CuTPyP–Co. FeTPyP–Co has a peak potential similar to CoTPyP and the second lowest onset potential. The onset potential of CuTPyP–Co is only slightly higher and has the smallest peak potential of all samples. Sorting by increasing catalytic activity leads to the sequence:

$$\text{Fe/CuTPyP–Fe} < \text{FeTPyP} < \text{CoTPyP–Fe} < \text{CoTPyP(–Co)} < \text{Fe/CuTPyP–Co}$$

This allows one to draw several conclusions; Incorporation of Fe as the second metal leads to a reduced catalytic activity (Except for CuTPyP–Fe compared to CuTPyP). Using Co is advantageous for ORR, since all Co containing samples show a higher catalytic activity than Co free samples. The position of the metal within the networks plays an important role; even though CoTPyP shows a better catalytic activity than FeTPyP, the best performance is observed for hetero-bimetallic networks (FeTPyP–Co and CuTPyP–Co) where Co is located in the peripheral positions and not within the central macrocycle. This is a remarkable result since FeTPyP and CuTPyP (without Co in the peripheral positions) have comparatively low catalytic activities. CoTPyP and CoTPyP–Co, on the other hand, show almost identical catalytic properties. It is not one metal alone that makes an efficient catalyst, but rather the correct metal combination in the right positioning is enhancing the catalytic activity. It is noteworthy that the combination Fe–Co and Cu–Co show the best catalytic activity, but exchanging Co with Fe leads to the combination with the lowest performance (Fe–Fe and Cu–Fe). The important role of the exact positioning within the networks becomes evident by comparing CoTPyP–Fe with FeTPyP–Co; this permutation modifies the peak position and the onset potential.

The catalytic activity of Co- [156–160] and Fe-porphyrins [161–163] towards the ORR is well known and is influenced by the substituents at the porphyrin ring and the substrate. Furthermore the catalytic activity towards the ORR of FeTPyP and CoTPyP can be enhanced by pyridyl-N coordination to Ru- or Os-complexes [164–166].

The activation is ascribed to π-backbonding of the pyridyl groups to the Ru or Os complexes, which transfers electron density to the porphyrin ring and modulates its electron transfer capability. Enhanced electrocatalytic oxygen reduction was also reported for a Co-porphyrin bonding with two pyridyl groups to Pt-complexes [167] and for FeTPyPCl coordinating with pyridyl-N to transition metal ions [168]. Even though the experimental conditions of the latter study are completely different FeTPyPCl and the transition metal ions are absorbed from solution on the basal plane of highly oriented pyrolytic graphite and the ORR is performed in 0.1 M perchloric acid similarities to our results can be found. Coordination of FeTPyP to Fe leads to a small decrease in the catalytic activity, whereas coordination to Co shifts the peak position to lower overpotentials and enhances the catalytic activity [168]. These observations are in accordance with our results. The enhanced catalytic activity is ascribed by an electronic interaction between the metal center in the porphyrin and the additional peripheral metal through the coordination bonds and the conjugated bonds in the porphyrin. From biological and synthetic bimetallic systems the synergistic effect of two proximate metal ions is known [70]. In our case, the electronic structure of the metal centers is also influenced by the surface trans effect, which modifies their ability to stabilize different reaction intermediates [169]. Insight into the electronic structure could be obtained by XPS measurements. In addition, theoretical calculations are needed for a better understanding of the complex interplay between metal centers and their effect on redox and catalytic properties.

6.3 Oxygen Evolution Reaction

The catalytic activities towards the OER of the different molecular networks were studied. Figure 6.8 shows the anodic branch of cyclic voltammetry experiments in argon saturated 0.1 M NaOH solution. For bare Au(111) (Fig. 6.8 gray line) and the metal-fee H_2TPyP monolayer (Fig. 6.8 dashed line) no catalytic activity is observed. The metallo-porphyrins show different behaviors; CuTPyP (Fig. 6.8a green line) shows no catalytic activity, but FeTPyP and CoTPyP (Fig.6.8b blue and Fig.6.8c red line, respectively) show an increase in the current density above 0.65 V is associated with

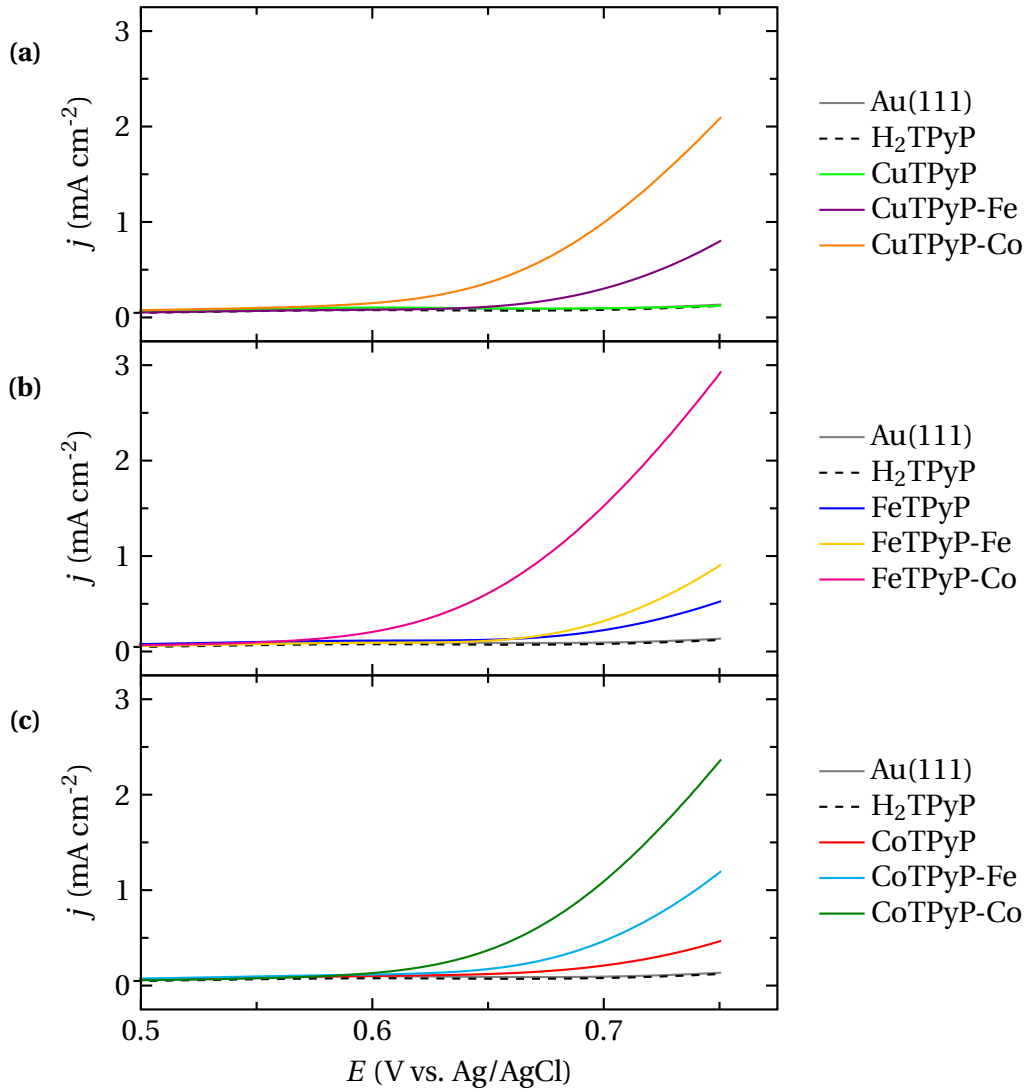

Figure 6.8: Anodic branch of cyclic voltammetry experiments in argon saturated 0.1 M NaOH solution for different networks, scan rate 50 mV s^{-1}.

the evolution of oxygen [170]. The incorporation of Fe as the second metal in the structures leads to noticeable higher catalytic activities. The polarization curves of FeTPyP-Fe and CoTPyP–Fe (Fig. 6.8b yellow and Fig. 6.8c cyan line, respectively) are shifted to lower overpotentials and a larger slope leads to a larger current density at 0.75 V compared to single metals FeTPyP and CoTPyP. It is remarkable that CuTPyP–Fe (Fig. 6.8a violet line) shows a really similar profile like FeTPyP-Fe and CoTPyP–Fe, even though no catalytic activity was observed for CuTPyP. These results are in agreement with the predicted enhancement of electrocatalytic activities due to a cooperative effect of a second metal in the structure [71, 72]. Taking advantage of the versatility of our preparation method, we prepared the same bimetallic networks with Co as the second metal. The onset potentials of CuTPyP–Co, FeTPyP–Co and CoTPyP–Co (Fig. 6.8a orange, Fig. 6.8b magenta, and Fig. 6.8c dark green line) are likewise shifted to lower overpotentials with increased current densities at 0.75 V compared with the M^{1}TPyP−Fe networks.

For easier comparison of the catalytic activities, the current density at 0.75 V and the onset potential of the different samples are extracted from Figure 6.8 and presented in Figure 6.9. The current density as a measure of catalytic activity has its lowest value (≈0.5 mA cm^{-2}) for the two monometallic networks with Fe or Co incor-

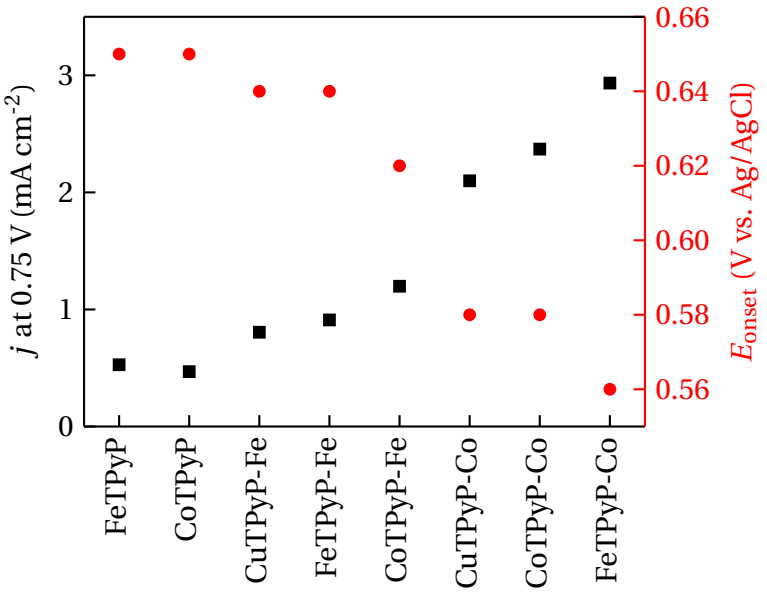

Figure 6.9: Comparison of current density at 0.75 V (black squares) and onset potentials (red circles) for different samples extracted from Figure 6.8. CuTPyP is omitted since it showed no catalytic activity.

porated in the TPyP macrocycle. An increase in activity is observed for the bimetallic networks, beginning with CuTPyP–Fe and ending with FeTPyP–Co with the highest activity (≈3 mA cm^{-2}). The inverse trend is observed for the onset potential, which is highest for the monometallic networks and smallest for FeTPyP–Co. These two parameters showcase the superiority of the bimetallic network FeTPyP–Co over the other networks, leading to an increased O_2 production (current density) and faster reaction kinetics (onset potential). It is noteworthy that the exact position of the metal centers within the network crucially influence its catalytic properties. The networks in which Co is coordinated by the pyridine groups of M^1TPyP outperform the networks with Fe as secondary metal atom. However, FeTPyP–Co is a better catalyst than CoTPyP–Co, while CoTPyP–Fe outperforms FeTPyP–Fe. The increased activity can thus not solely be traced back to the monodisperse Co on the surface, but its combination with the metal in the macrocycle makes the efficient catalyst.

Direct evidence that water splitting takes place is the presence of a cathodic peak in the cyclic voltammetry curves, shown in Figure 6.10. This peak located around –0.25 V corresponds to the reduction of O_2, whose origin rests in the previous OER during the anodic scan. No O_2 is present in solution prior to OER in the Ar saturated solution. The area of the peak around –0.3 V for each network (Table 6.1) is thus a direct measure of the O_2 produced during OER. The values are in complete agreement with the catalytic activity presented in Figure 6.9 following the sequence of increasing catalytic activity:

$$M^1\text{TPyP} < M^1\text{TPyP-Fe} < M^1\text{TPyP-Co}$$

Adding Fe as the secondary metal to the FeTPyP and CoTPyP networks increases the amount of generated O_2 by a factor of about 13 and 4, respectively. Adding Co to both networks increases O_2 generation by factors of 86 and 20. The amount of generated O_2 by CuTPyP–Fe and CuTPyP–Co cannot be compared to the corresponding monometallic network since CuTPyP showed no catalytic activity. Taking FeTPyP as reference leads to increased O_2 generation by factors of about 11 and 45 for CuTPyP–Fe and CuTPyP–Co, respectively. The number of catalytically active sites, assuming each metal atom on the surface contributes as redox center, increases two-fold after addition of the second metal. The increased catalytic activity is thus not merely a consequence of the increased number of catalytic centers, but stems from more fundamental properties such as changes in the electronic structure of the metals in mono- vs. bimetallic networks [71, 72].

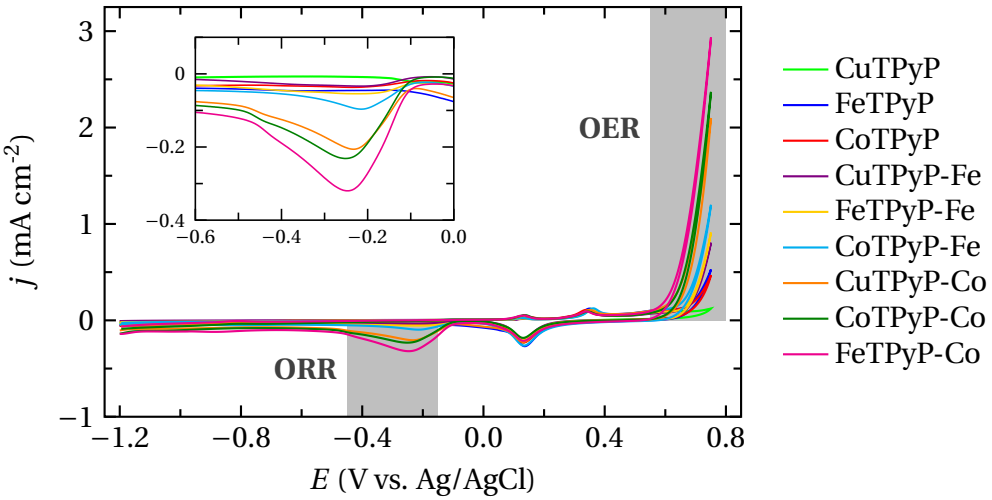

Figure 6.10: Cyclic voltammetry in argon saturated 0.1 M NaOH solution for all molecular networks, scan rate 50 mV s^{-1}. The Oxygen evolution reaction (OER) and oxygen reduction reaction (ORR) are highlighted. Inset: Zoomed cathodic branch.

The major components contributing to the catalytic activity are the Fe and Co metal centers, since the metal-free H_2TPyP and CuTPyP monolayers show the same current-potential behavior as the bare Au(111) surface and no catalytic activity. The d^9 configuration of Cu(II) hinders the binding of hydroxide as an axial ligand and thus OER will not occur at copper ion porphyrins [170]. The better catalytic activity of CoTPyP with respect to FeTPyP is in agreement with literature [144, 170] and has its origins in the similar orbital energy of Co and oxygen, generating a strong interaction of the Co centers with the oxygen of the hydroxide ions [170]. For the bimetallic networks two distinctive trends are observed: (i) all bimetallic networks present a substantial increase in the catalytic activity compared with the single metal networks, and (ii) bimetallic networks containing Co coordinated in the peripheral positions show the best performance. In particular, the hetero-bimetallic network FeTPyP–Co outperforms all other networks. The synergistic effect of two proximate metal ions is widely observed in both biological and synthetic bimetallic systems [70]. The second observation might be due to an optimal adjustment of the oxidation state of Co suitable for efficient OER, favoring improved interactions with reaction intermediates. This adjustment of the oxidation state is governed by (i) by the coordination environment, i. e. the pyridine nitrogen, (ii) by the neighboring metal within the molecular macrocycle, and (iii) by the interaction with the surface. The extended π-electron system of TPyP might be able to promote weak coupling of the two metal centers, and the surface trans effect will influence the electronic structure of the metal centers and their

Network	O_2 (nmol/cm^{-2})	relative to FeTPyP	relative to CoTPyP
FeTPyP	0.037	1	
CoTPyP	0.138	4	1
CuTPyP–Fe	0.409	*11*	3
FeTPyP–Fe	0.501	13	4
CoTPyP–Fe	0.539	14	4
CuTPyP–Co	1.690	*45*	12
CoTPyP–Co	2.823	76	20
FeTPyP–Co	3.193	86	23

Table 6.1: Amount of electrochemically evolved O_2 during OER for each network. Numbers are calculated from the area of the reduction peak at –0.25 V in Figure 6.10 considering a full reduction of O_2 ($4\,e^-$ mechanism) and normalizing to the electrochemical area of the Au(111) surface.

ability to stabilize different reaction intermediates [169]. Organic scaffold-induced cooperative effects on the active metal centers are also observed in the functional activation in enzymes galactose oxidase and hydrogenases [171–180]. Geometric factors favor the adequate accommodation of the two metal centers in an appropriate distance [154] allowing the adsorption, desorption and/or weakening of the bond to be broken, and electronic effects through an electron density redistribution in both metal centers promoted by the organic environment [169] can lead to a specific charge state in the active sites, which facilitate the (de)stabilization of the reaction intermediates. For these results, this means that additional experiments and a theoretical treatment are needed for a complete understanding of the complex interplay between metal centers and its effect on redox and catalytic properties.

6.4 Conclusions

The preparation of two-dimensional homo- and hetero-bimetallic has been shown and their influence on the catalytic activity towards the ORR and OER was studied. The right metal combination leads to an increased catalytic activity and the exact positioning within the network plays an important role. A non-linearly increased catalytic activity towards the evolution of oxygen compared to monometallic networks has been demonstrated. The hetero-bimetallic network FeTPyP–Co showed high catalytic activity for both reactions.

The combinatorial approach allows for the exact positioning of different metal centers at defined positions within the network, tuning the catalytic properties of this material. This unprecedented regular distribution of single-atom catalytic homo and/or hetero metal centers opens the way towards a class of catalysts that will grant insight into the interplay of different metals, as Fe, Co, and Cu can be replaced by many different types of atoms. Electronic coupling through the organic framework can be addressed through tailoring the porphyrin's functional groups or by switching to other organic molecules altogether, and changing the supporting substrate offers yet another parameter for adjusting catalytic activity. We expect that this approach will yield valuable new insight into bi- and multimetallic catalysts.

Summary and Outlook

In view of the growing worldwide demand for energy and climate change, novel catalytic materials for applications in energy conversion and fuel production are needed. In metallo-enzymes, transition metal atoms are embedded in an organic matrix to catalyze important processes. These catalytically active sites can be effectively mimicked in 2D-MOCNs self-assembled on electrode surfaces. The activity of the metal centers is determined by their type of the metal and their coordination environment. Both parameters can be carefully adjusted in 2D-MOCNs by combining several transition metals with different organic ligands with varying functional groups.

In the present thesis, electrocatalytic properties of 2D-MOCNs were studied and the catalytic activity of 2D-MOCNs was demonstrated for the first time. Several MOCNs with different metals and various ligands were prepared and electrochemically investigated to study their influence on the catalytic activity.

In order to study and correlate electrocatalytic properties with the atomic structure of 2D-MOCNs, a STM operating in UHV was combined with an EC setup. Sample preparation and STM characterization were conducted under UHV conditions. By STM, the composition and structure of the networks were controlled and characterized prior to electrochemical experiments. A transfer system between UHV and EC instrumentation was constructed to keep the sample in a clean and controlled environment at all times. In the realized system the design of the EC cell is quite close to conventional cells, which allows one to work with the usual volumes of liquid in a well-established configuration. Moreover, the system gives one maximum control of the transfer between UHV and EC environments and *vice versa*. To demonstrate the efficacy and cleanliness of the transfer, STM and EC measurements of a bare Au(111) surface were performed and typical results were obtained in both. In addition, STM measurements after EC experiments were shown for the PBP–Fe network.

The mechanism of the ORR can be influenced by the type of the metal center in the network. The catalytic activity towards ORR in alkaline media was demonstrated for the TMA–Fe network. It catalyzes the reduction of O_2 to H_2O via an indirect $(2+2)e^-$ pathway with an H_2O_2 intermediate. The key role of the unsaturated metal centers in the electrocatalytic reduction of O_2 becomes evident when going from Fe- to Mn-based MOCNs. The structure of the TMA–Mn network is identical to that of TMA–Fe, but the EC behavior differs significantly; TMA–Mn reduces O_2 directly to H_2O through a $4e^-$ pathway. Control experiments using the same amount of metal adatoms contained in the networks show a similar behavior as the corresponding networks but with substantially reduced catalytic activity. This result emphasizes the importance of the complexation of the metal atoms; the chemical activity of the metal centers is determined by both the nature of the metal ion and its coordination shell. In addition, the ligation separates the unsaturated metal atoms preventing catalytic deactivation.

To study the effect of the coordination environment, three different Fe-based nitrogen-coordinated metal-organic structures were compared: TCNQ–Fe, PBP–Fe and FePc. The distinct coordination environment of the Fe in each network influences the final product and the mechanism of the ORR. TCNQ–Fe catalyzes the reduction of O_2 only to H_2O_2 on a $2e^-$ pathway. For PBP–Fe and FePc the complete reduction to H_2O is observed. PBP–Fe catalyzes the reduction of O_2 via an indirect $(2+2)e^-$ pathway with intermediate H_2O_2, while FePc catalyzes directly to H_2O by a $4e^-$ pathway. The differences in the electrocatalytic response might be a result of the electron density on the Fe centers within the metal-organic structures. TCNQ withdraws significant electron density from the Fe centers, such that Fe(III) is most likely the dominant species. Fe(III) is not favored as an active site for O_2 reduction and H_2O_2 leaves as the two-electron reduction product. In the case of PBP–Fe, the Fe(II) species become predominant at potentials more negative than –0.65/–0.75 V. The strong bonding of H_2O_2 to Fe(II) prevents it from leaving as a two-electron reduction product and provides a path for final reduction to H_2O. In FePc, the π-electron rich macrocycle favors the catalytic active Fe(II) species and the Fe(III)/Fe(II) transition is positively shifted to less negative potentials very close to the onset potential of O_2 reduction. Also, the geometry of the coordination environment might play a role for the catalytic activity, since the ligand field can alter the energetic arrangement of the d-orbitals of the Fe centers, modifying their interaction with oxygen and reaction intermediates. In FePc the Fe atoms is coordinated by four N atoms, while PBP–Fe has a threefold

coordination environment.

In the last part of this thesis, the two metal binding sites of TPyP were used to selectively incorporate different metal centers in a fixed organic environment and create homo- and hetero-bimetallic networks. The influence of the second metal on the catalytic activity towards the ORR and OER was studied. For the ORR, the incorporation of Fe in the peripheral position leads to an decrease in the catalytic activity compared to the single metal networks, with the exception of CuTPyP–Fe which outperforms CuTPyP. The incorporation of Co, on the contrary, enhances the catalytic activity, except for CoTPyP–Co, which shows almost identical catalytic properties like CoTPyP. The best performance is observed for the hetero-bimetallic networks FeTPyP–Co and CuTPyP–Co. The correct combination of two metal centers in the right positions makes an efficient catalyst. In the case of the OER, two distinctive trends are observed (i) all bimetallic networks present a substantial increase in the catalytic activity compared to single metal networks, and (ii) bimetallic networks containing Co coordinated in the peripheral positions show the best performances. In particular, the hetero-bimetallic network FeTPyP–Co outperforms all other networks; the amount of generated O_2 is increased by a factor of 86 compared to FeTPyP.

To summarize, it was demonstrated that the mechanism and the final product of the ORR can be influenced by the choice of the metal center and by altering the coordination environment. Moreover, coupling of two metals centers promoted by the organic environment modifies the electrocatalytic response. A non-linearly increased catalytic activity towards the evolution of oxygen has been observed, demonstrating the cooperative bimetallic effect.

The presented results give rise for several future investigations. As mentioned different before ligand geometries can change the energetic arrangement of the d-orbitals of the metal centers [147]. A threefold coordination environment could show a different catalytic activity than a fourfold. To study this geometric aspect, different networks could be prepared in which the metal center is coordinated each to a different number of the same functional group. These investigations may also contribute in the determination of the active sites of pyrolyzed Fe–N_x/C materials. As the subscript x indicates, the number of coordinating N is unknown. One proposed structure of the active site consists of pyridinic species coordinating Fe in a fourfold planar geometry [145]. A similar coordination geometry can be obtained in MOCNs.

In the case of the bimetallic networks, the electronic coupling through the organic framework can be studied through tailoring the porphyrin's functional groups. By replacing the pyridyl groups with the more strongly π-accepting 4-cyanophenyl groups, a stronger coupling of the two metal centers could be obtained [164]. The extent to which electron density from π-backbonding is transmitted to the porphyrin ring is also influenced by the angle between the planes of the porphyrin ring and the 4-cyanophenyl rings attached to it. Increasing the angle by methylation of the phenyl ring at the 2 and 6 positions leads to a reduced electron transfer and, therefore, lower catalytic activity [164]. For tetraphenylporphyrin it is known that annealing on more reactive substrates, like Cu(111) and Ag(111), can lead to a dehydrogenation and formation of new C–C bonds between the phenyl rings and the porphyrin ring, which results in a highly conjugated flat configuration [181, 182]. In case of TPyP-based bimetallic networks this planar geometry could lead to a stronger interaction between the two metal center. Another approach would be to switch to other organic molecules. Phthalocyanines are related macrocycles, which have a flat configuration and a fully conjugated π-electron system. With the addition of suitable functional groups they can also used as building blocks for bimetallic networks.

The EC experiments in this thesis were performed in a three-electrode conventional EC cell. For a deeper understanding of the electron transfer characteristics and to overcome kinetic limitations in the EC measurements, the development and implementation of a flow-cell system in the experimental setup is necessary. Working with hydrodynamic methods allows one to obtain kinetic data and gain further insight in the processes and mechanism of the reactions. By measuring the mass-transfer limited currents for different flow rates the number of transferred electrons and rate constants can be obtained.

A vast number of alternative networks can be prepared by using different organic ligands with varying functional groups and combining them with several transition metals. Changing the supporting substrate offers another parameter for adjusting catalytic activity. Furthermore, the electrochemical investigations can be extended to other important reactions, like CO_2 reduction, which generate valuable hydrocarbons. For a more targeted design of new networks a better understanding of the underlying effects influencing the catalytic activity is necessary and additional experimental and theoretical treatments are needed. The electronic structure and state of the metal centers could be investigated by X-ray absorption spectroscopy and XPS. DFT based calculations could be performed to obtain further insight into the elec-

tronic structure and to evaluate binding energies of the metal centers with reaction intermediates. These considerations could help to develop networks with further improved properties.

In conclusion, the results presented in this thesis demonstrate that 2D-MOCNs with structural resemblance to enzyme active sites have a high potential for heterogeneous catalytic chemical conversions. Engineering of the network structure and the distinct coordination environment of the metal centers offers the possibility to tune their catalytic activity and to create tailor-made 2D-MOCNs for specific applications. This opens up a new route for the design of a new class of nanocatalyst materials.

Bibliography

[1] G. M. Whitesides and G. W. Crabtree. *Don't Forget Long-Term Fundamental Research in Energy.* Science, **315**(5813):796–798, 2007. doi:10.1126/science.1140362.

[2] A. J. Bard. *Inner-Sphere Heterogeneous Electrode Reactions. Electrocatalysis and Photocatalysis: The Challenge.* Journal of the American Chemical Society, **132**(22):7559–7567, 2010. doi:10.1021/ja101578m.

[3] H. A. Gasteiger and N. M. Marković. *Just a Dream—or Future Reality?* Science, **324**(5923):48–49, 2009. doi:10.1126/science.1172083.

[4] R. Cao, W. Lai, and P. Du. *Catalytic water oxidation at single metal sites.* Energy Environ. Sci., **5**:8134–8157, 2012. doi:10.1039/C2EE21494F.

[5] M. G. Walter, E. L. Warren, J. R. McKone, S. W. Boettcher, Q. Mi, E. A. Santori, and N. S. Lewis. *Solar Water Splitting Cells.* Chemical Reviews, **110**(11):6446–6473, 2010. doi:10.1021/cr1002326.

[6] I. Katsounaros, S. Cherevko, A. R. Zeradjanin, and K. J. J. Mayrhofer. *Oxygen Electrochemistry as a Cornerstone for Sustainable Energy Conversion.* Angewandte Chemie International Edition, **53**(1):102–121, 2014. doi:10.1002/anie.201306588.

[7] G. Binnig and H. Rohrer. *Scanning tunneling microscopy.* IBM Journal of Research and Development, **44**(1.2):279–293, 2000. doi:10.1147/rd.441.0279.

[8] D. M. Eigler and E. K. Schweizer. *Positioning single atoms with a scanning tunnelling microscope.* Nature, **344**:524–526, 1990. doi:10.1038/344524a0.

[9] W. Ho. *Single-molecule chemistry.* The Journal of Chemical Physics, **117**(24):11033–11061, 2002. doi:10.1063/1.1521153.

[10] H. J. Zandvliet and A. van Houselt. *Scanning Tunneling Spectroscopy.* Annual Review of Analytical Chemistry, **2**(1):37–55, 2009. doi:10.1146/annurev-anchem-060908-155213.

[11] T. A. Jung, R. R. Schlittler, and J. K. Gimzewski. *Conformational identification of individual adsorbed molecules with the STM.* Nature, **386**:696–698, 1997. doi:10.1038/386696a0.

[12] A. Dmitriev, H. Spillmann, N. Lin, J. V. Barth, and K. Kern. *Modular Assembly of Two-Dimensional Metal–Organic Coordination Networks at a Metal Surface.* Angewandte Chemie International Edition, **42**(23):2670–2673, 2003. doi:10.1002/anie.200250610.

[13] T. Yokoyama, S. Yokoyama, T. Kamikado, Y. Okuno, and S. Mashiko. *Selective assembly on a surface of supramolecular aggregates with controlled size and shape.* Nature, **413**:619–621, 2001. doi:10.1038/35098059.

[14] F. Rosei, M. Schunack, P. Jiang, A. Gourdon, E. Lægsgaard, I. Stensgaard, C. Joachim, and F. Besenbacher. *Organic Molecules Acting as Templates on Metal Surfaces.* Science, **296**(5566):328–331, 2002. doi:10.1126/science.1069157.

[15] J. A. Theobald, N. S. Oxtoby, M. A. Phillips, N. R. Champness, and P. H. Beton. *Controlling molecular deposition and layer structure with supramolecular surface assemblies.* Nature, **424**:1029–1031, 2003. doi:10.1038/nature01915.

[16] H. Spillmann, A. Dmitriev, N. Lin, P. Messina, J. V. Barth, and K. Kern. *Hierarchical Assembly of Two-Dimensional Homochiral Nanocavity Arrays.* Journal of the American Chemical Society, **125**(35):10725–10728, 2003. doi:10.1021/ja0362353.

[17] G. P. Lopinski, D. J. Moffatt, D. D. M. Wayner, and R. A. Wolkow. *Determination of the absolute chirality of individual adsorbed molecules using the scanning tunnelling microscope.* Nature, **392**:909–911, 1998. doi:10.1038/31913.

[18] J. V. Barth, J. Weckesser, G. Trimarchi, M. Vladimirova, A. De Vita, C. Cai, H. Brune, P. Günter, and K. Kern. *Stereochemical Effects in Supramolecular Self-Assembly at Surfaces: 1-D versus 2-D Enantiomorphic Ordering for PVBA and*

PEBA on Ag(111). Journal of the American Chemical Society, **124**(27):7991–8000, 2002. doi:10.1021/ja0256764.

[19] T. Zambelli, J. V. Barth, J. Wintterlin, and G. Ertl. *Complex pathways in dissociative adsorption of oxygen on platinum*. Nature, **390**:495–497, 1997. doi:10.1038/37329.

[20] M. Dürr, A. Biedermann, Z. Hu, U. Höfer, and T. F. Heinz. *Probing High-Barrier Pathways of Surface Reactions by Scanning Tunneling Microscopy*. Science, **296**(5574):1838–1841, 2002. doi:10.1126/science.1070859.

[21] X.-C. Guo and R. J. Madix. *Imaging Surface Reactions at Atomic Resolution: A Wealth of Behavior on the Nanoscale*. The Journal of Physical Chemistry B, **107**(14):3105–3116, 2003. doi:10.1021/jp0219799.

[22] M. O. Lorenzo, S. Haq, T. Bertrams, P. Murray, R. Raval, and C. J. Baddeley. *Creating Chiral Surfaces for Enantioselective Heterogeneous Catalysis: R,R-Tartaric Acid on Cu(110)*. The Journal of Physical Chemistry B, **103**(48):10661–10669, 1999. doi:10.1021/jp992188i.

[23] J. Wintterlin. *Scanning tunneling microscopy studies of catalytic reactions*. In: *Impact of Surface Science on Catalysis*. Advances in Catalysis **45**:131–206, 2000. doi:10.1007/128_2008_152.

[24] F. Besenbacher, I. Chorkendorff, B. S. Clausen, B. Hammer, A. M. Molenbroek, J. K. Nørskov, and I. Stensgaard. *Design of a surface alloy catalyst for steam reforming*. Science, **279**(5358):1913–1915, 1998. doi:10.1126/science.279.5358.1913.

[25] B. D. Gates, Q. Xu, M. Stewart, D. Ryan, C. G. Willson, and G. M. Whitesides. *New Approaches to Nanofabrication: Molding, Printing, and Other Techniques*. Chemical Reviews, **105**(4):1171–1196, 2005. doi:10.1021/cr030076o.

[26] J. V. Barth, G. Costantini, and K. Kern. *Engineering atomic and molecular nanostructures at surfaces*. Nature, **437**:671–679, 2005. doi:10.1038/nature04166.

[27] J.-M. Lehn. *Supramolecular Chemistry: Concepts and Perspectives*. Wiley-VCH, Weinheim, 1995.

[28] M. J. Wiester, P. A. Ulmann, and C. A. Mirkin. *Enzyme Mimics Based Upon Supramolecular Coordination Chemistry*. Angewandte Chemie International Edition, **50**(1):114–137, 2011. doi:10.1002/anie.201000380.

[29] J. W. Steed and J. L. Atwood. *Supramolecular Chemistry*. Wiley-VCH, Weinheim, 2nd edition, 2009.

[30] B. J. Holliday and C. A. Mirkin. *Strategies for the Construction of Supramolecular Compounds through Coordination Chemistry*. Angewandte Chemie International Edition, **40**(11):2022–2043, 2001. doi:10.1002/1521-3773(20010601)40:11<2022::AID-ANIE2022>3.0.CO;2-D.

[31] A. Werner. *Beitrag zur Konstitution anorganischer Verbindungen*. Zeitschrift für anorganische Chemie, **3**(1):267–330, 1893. doi:10.1002/zaac.18930030136.

[32] A. L. Feig and S. J. Lippard. *Reactions of Non-Heme Iron(II) Centers with Dioxygen in Biology and Chemistry*. Chemical Reviews, **94**(3):759–805, 1994. doi:10.1021/cr00027a011.

[33] E. I. Solomon, T. C. Brunold, M. I. Davis, J. N. Kemsley, S.-K. Lee, N. Lehnert, F. Neese, A. J. Skulan, Y.-S. Yang, and J. Zhou. *Geometric and Electronic Structure/Function Correlations in Non-Heme Iron Enzymes*. Chemical Reviews, **100**(1):235–350, 2000. doi:10.1021/cr9900275.

[34] J. Lee, O. K. Farha, J. Roberts, K. A. Scheidt, S. T. Nguyen, and J. T. Hupp. *Metal-organic framework materials as catalysts*. Chemical Society Reviews, **38**:1450–1459, 2009. doi:10.1039/B807080F.

[35] J. Liu, L. Chen, H. Cui, J. Zhang, L. Zhang, and C.-Y. Su. *Applications of metal-organic frameworks in heterogeneous supramolecular catalysis*. Chemical Society Reviews, **43**:6011–6061, 2014. doi:10.1039/C4CS00094C.

[36] J. Gascon, A. Corma, F. Kapteijn, and F. X. Llabrés i Xamena. *Metal Organic Framework Catalysis: Quo vadis?* ACS Catalysis, **4**(2):361–378, 2014. doi:10.1021/cs400959k.

[37] Z. Zhang, H. Yoshikawa, and K. Awaga. *Monitoring the Solid-State Electrochemistry of Cu(2,7-AQDC) (AQDC = Anthraquinone Dicarboxylate) in a Lithium Battery: Coexistence of Metal and Ligand Redox Activities in a Metal–Organic*

Framework. Journal of the American Chemical Society, **136**(46):16112–16115, 2014. doi:10.1021/ja508197w.

[38] B. Nohra, H. El Moll, L. M. Rodriguez Albelo, P. Mialane, J. Marrot, C. Mellot-Draznieks, M. O'Keeffe, R. Ngo Biboum, J. Lemaire, B. Keita, L. Nadjo, and A. Dolbecq. *Polyoxometalate-Based Metal Organic Frameworks (POMOFs): Structural Trends, Energetics, and High Electrocatalytic Efficiency for Hydrogen Evolution Reaction*. Journal of the American Chemical Society, **133**(34):13363–13374, 2011. doi:10.1021/ja201165c.

[39] J. Mao, L. Yang, P. Yu, X. Wei, and L. Mao. *Electrocatalytic four-electron reduction of oxygen with Copper (II)-based metal-organic frameworks*. Electrochemistry Communications, **19**(0):29–31, 2012. doi:10.1016/j.elecom.2012.02.025.

[40] S. S. Park, E. R. Hontz, L. Sun, C. H. Hendon, A. Walsh, T. Van Voorhis, and M. Dincă. *Cation-Dependent Intrinsic Electrical Conductivity in Isostructural Tetrathiafulvalene-Based Microporous Metal–Organic Frameworks*. Journal of the American Chemical Society, **137**(5):1774–1777, 2015. doi:10.1021/ja512437u.

[41] L. Sun, C. H. Hendon, M. A. Minier, A. Walsh, and M. Dincă. *Million-Fold Electrical Conductivity Enhancement in Fe2(DEBDC) versus Mn2(DEBDC) (E = S, O)*. Journal of the American Chemical Society, **137**(19):6164–6167, 2015. doi:10.1021/jacs.5b02897.

[42] S. R. Ahrenholtz, C. C. Epley, and A. J. Morris. *Solvothermal Preparation of an Electrocatalytic Metalloporphyrin MOF Thin Film and its Redox Hopping Charge-Transfer Mechanism*. Journal of the American Chemical Society, **136**(6):2464–2472, 2014. doi:10.1021/ja410684q.

[43] M. Jahan, Q. Bao, and K. P. Loh. *Electrocatalytically Active Graphene–Porphyrin MOF Composite for Oxygen Reduction Reaction*. Journal of the American Chemical Society, **134**(15):6707–6713, 2012. doi:10.1021/ja211433h.

[44] J. V. Barth. *Fresh perspectives for surface coordination chemistry*. Surface Science, **603**(10–12):1533–1541, 2009. doi:http://dx.doi.org/10.1016/j.susc.2008.09.049.

[45] J. K. Norskov, T. Bligaard, J. Rossmeisl, and C. H. Christensen. *Towards the computational design of solid catalysts.* Nature Chemistry, **1**:37–46, 2009. doi:dx.doi.org/10.1038/nchem.121.

[46] C. E. Valdez, Q. A. Smith, M. R. Nechay, and A. N. Alexandrova. *Mysteries of Metals in Metalloenzymes.* Accounts of Chemical Research, **47**(10):3110–3117, 2014. doi:10.1021/ar500227u.

[47] Y. Lu, N. Yeung, N. Sieracki, and N. M. Marshall. *Design of functional metalloproteins.* Nature, **460**:855–862, 2009. doi:10.1038/nature08304.

[48] A. Messerschmidt. *Handbook of Metalloproteins.* John Wiley & Sons, Ltd, Chichester, 2001. doi:10.1002/0470028637.

[49] L. Que and W. B. Tolman. *Biologically inspired oxidation catalysis.* Nature, **455**:333–340, 2008. doi:10.1038/nature07371.

[50] J. Liu, S. Chakraborty, P. Hosseinzadeh, Y. Yu, S. Tian, I. Petrik, A. Bhagi, and Y. Lu. *Metalloproteins Containing Cytochrome, Iron–Sulfur, or Copper Redox Centers.* Chemical Reviews, **114**(8):4366–4469, 2014. doi:10.1021/cr400479b.

[51] W. Lubitz, H. Ogata, O. Rüdiger, and E. Reijerse. *Hydrogenases.* Chemical Reviews, **114**(8):4081–4148, 2014. doi:10.1021/cr4005814.

[52] W. Li, A. Yu, D. C. Higgins, B. G. Llanos, and Z. Chen. *Biologically Inspired Highly Durable Iron Phthalocyanine Catalysts for Oxygen Reduction Reaction in Polymer Electrolyte Membrane Fuel Cells.* Journal of the American Chemical Society, **132**(48):17056–17058, 2010. doi:10.1021/ja106217u.

[53] S. Stepanow, N. Lin, J. V. Barth, and K. Kern. *Surface-Template Assembly of Two-Dimensional Metal-Organic Coordination Networks.* The Journal of Physical Chemistry B, **110**(46):23472–23477, 2006. doi:10.1021/jp065066g.

[54] P. Gambardella, S. Stepanow, A. Dmitriev, J. Honolka, F. M. F. de Groot, M. Lingenfelder, S. S. Gupta, D. D. Sarma, P. Bencok, S. Stanescu, S. Clair, S. Pons, N. Lin, A. P. Seitsonen, H. Brune, J. V. Barth, and K. Kern. *Supramolecular control of the magnetic anisotropy in two-dimensional high-spin Fe arrays at a metal interface.* Nature Materials, **8**:189–193, 2009. doi:10.1038/nmat2376.

[55] J. Elemans, S. Lei, and S. De Feyter. *Molecular and Supramolecular Networks on Surfaces: From Two-Dimensional Crystal Engineering to Reactivity*. Angewandte Chemie International Edition, **48**(40):7298–7332, 2009. doi:10.1002/anie.200806339.

[56] F. Rosei. *Nanostructured surfaces: challenges and frontiers in nanotechnology*. Journal of Physics: Condensed Matter, **16**(17):S1373, 2004. doi:10.1088/0953-8984/16/17/001.

[57] S. Stepanow, N. Lin, and J. V. Barth. *Modular assembly of low-dimensional coordination architectures on metal surfaces*. Journal of Physics: Condensed Matter, **20**(18):184002, 2008. doi:10.1088/0953-8984/20/18/184002.

[58] A. Langner, S. L. Tait, N. Lin, C. Rajadurai, M. Ruben, and K. Kern. *Self-recognition and self-selection in multicomponent supramolecular coordination networks on surfaces*. Proceedings of the National Academy of Sciences, **104**(46):17927–17930, 2007. doi:10.1073/pnas.0704882104.

[59] S. Stepanow, M. Lingenfelder, A. Dmitriev, H. Spillmann, E. Delvigne, N. Lin, X. Deng, C. Cai, J. V. Barth, and K. Kern. *Steering molecular organization and host-guest interactions using two-dimensional nanoporous coordination systems*. Nature Materials, **3**:229–233, 2004. doi:10.1038/nmat1088.

[60] S. Fabris, S. Stepanow, N. Lin, P. Gambardella, A. Dmitriev, J. Honolka, S. Baroni, and K. Kern. *Oxygen Dissociation by Concerted Action of Di-Iron Centers in Metal–Organic Coordination Networks at Surfaces: Modeling Non-Heme Iron Enzymes*. Nano Letters, **11**(12):5414–5420, 2011. doi:10.1021/nl2031713.

[61] F. Jaouen, E. Proietti, M. Lefevre, R. Chenitz, J.-P. Dodelet, G. Wu, H. T. Chung, C. M. Johnston, and P. Zelenay. *Recent advances in non-precious metal catalysis for oxygen-reduction reaction in polymer electrolyte fuel cells*. Energy & Environmental Science, **4**:114–130, 2011. doi:10.1039/C0EE00011F.

[62] M. Lefèvre, E. Proietti, F. Jaouen, and J.-P. Dodelet. *Iron-Based Catalysts with Improved Oxygen Reduction Activity in Polymer Electrolyte Fuel Cells*. Science, **324**(5923):71–74, 2009. doi:10.1126/science.1170051.

[63] G. Wu, K. L. More, C. M. Johnston, and P. Zelenay. *High-Performance Electrocatalysts for Oxygen Reduction Derived from Polyaniline, Iron, and Cobalt*. Science, **332**(6028):443–447, 2011. doi:10.1126/science.1200832.

[64] F. Jaouen, J. Herranz, M. Lefèvre, J.-P. Dodelet, U. I. Kramm, I. Herrmann, P. Bogdanoff, J. Maruyama, T. Nagaoka, A. Garsuch, J. R. Dahn, T. Olson, S. Pylypenko, P. Atanassov, and E. A. Ustinov. *Cross-Laboratory Experimental Study of Non-Noble-Metal Electrocatalysts for the Oxygen Reduction Reaction.* ACS Applied Materials & Interfaces, **1**(8):1623–1639, 2009. doi:10.1021/am900219g.

[65] G. Lalande, G. Faubert, R. Côté, D. Guay, J. Dodelet, L. Weng, and P. Bertrand. *Catalytic activity and stability of heat-treated iron phthalocyanines for the electroreduction of oxygen in polymer electrolyte fuel cells.* Journal of Power Sources, **61**(1–2):227–237, 1996. doi:10.1016/S0378-7753(96)02356-7.

[66] M. Ferrandon, A. J. Kropf, D. J. Myers, K. Artyushkova, U. Kramm, P. Bogdanoff, G. Wu, C. M. Johnston, and P. Zelenay. *Multitechnique Characterization of a Polyaniline–Iron–Carbon Oxygen Reduction Catalyst.* The Journal of Physical Chemistry C, **116**(30):16001–16013, 2012. doi:10.1021/jp302396g.

[67] W. Li, J. Wu, D. C. Higgins, J.-Y. Choi, and Z. Chen. *Determination of Iron Active Sites in Pyrolyzed Iron-Based Catalysts for the Oxygen Reduction Reaction.* ACS Catalysis, **2**(12):2761–2768, 2012. doi:10.1021/cs300579b.

[68] Q. Wang, Z.-Y. Zhou, Y.-J. Lai, Y. You, J.-G. Liu, X.-L. Wu, E. Terefe, C. Chen, L. Song, M. Rauf, N. Tian, and S.-G. Sun. *Phenylenediamine-Based FeNx/C Catalyst with High Activity for Oxygen Reduction in Acid Medium and Its Active-Site Probing.* Journal of the American Chemical Society, **136**(31):10882–10885, 2014. doi:10.1021/ja505777v.

[69] U. Tylus, Q. Jia, K. Strickland, N. Ramaswamy, A. Serov, P. Atanassov, and S. Mukerjee. *Elucidating Oxygen Reduction Active Sites in Pyrolyzed Metal-Nitrogen Coordinated Non-Precious-Metal Electrocatalyst Systems.* The Journal of Physical Chemistry C, **118**(17):8999–9008, 2014. doi:10.1021/jp500781v.

[70] B. Bosnich. *Cooperative bimetallic redox reactivity.* Inorganic Chemistry, **38**(11):2554–2562, 1999. doi:10.1021/ic990164k.

[71] H. Steinhagen and G. Helmchen. *Asymmetric Two-Center Catalysis–Learning from Nature.* Angewandte Chemie International Editionh, **35**(20):2339–2342, 1996. doi:10.1002/anie.199623391.

[72] E. K. van den Beuken and B. L. Feringa. *Bimetallic catalysis by late transition metal complexes.* Tetrahedron, **54**(43):12985–13011, 1998. doi:10.1016/S0040-4020(98)00319-6.

[73] J. I. van der Vlugt. *Cooperative Catalysis with First-Row Late Transition Metals.* European Journal of Inorganic Chemistry, **2012**(3):363–375, 2012. doi:10.1002/ejic.201100752.

[74] M. S. Burke, M. G. Kast, L. Trotochaud, A. M. Smith, and S. W. Boettcher. *Cobalt–Iron (Oxy)hydroxide Oxygen Evolution Electrocatalysts: The Role of Structure and Composition on Activity, Stability, and Mechanism.* Journal of the American Chemical Society, **137**(10):3638–3648, 2015. doi:10.1021/jacs.5b00281.

[75] Q. Lu, G. S. Hutchings, W. Yu, Y. Zhou, R. V. Forest, R. Tao, J. Rosen, B. T. Yonemoto, Z. Cao, H. Zheng, J. Q. Xiao, F. Jiao, and J. G. Chen. *Highly porous non-precious bimetallic electrocatalysts for efficient hydrogen evolution.* Nature Communications, **6**:6567, 2015. doi:10.1038/ncomms7567.

[76] L. K. Blusch, O. Mitevski, V. Martin-Diaconescu, K. Pröpper, S. DeBeer, S. Dechert, and F. Meyer. *Selective Synthesis and Redox Sequence of a Heterobimetallic Nickel/Copper Complex of the Noninnocent Siamese-Twin Porphyrin.* Inorganic Chemistry, **53**(15):7876–7885, 2014. doi:10.1021/ic500460n.

[77] A. Fuerte, A. Corma, M. Iglesias, E. Morales, and F. Sánchez. *A cooperative effect between support and the heterogenised metalloporphyrins on electrocatalytic oxygen reduction.* Catalysis Letters, **101**(1-2):99–103, 2005. doi:10.1007/s10562-004-3756-7.

[78] N. S. Porter, H. Wu, Z. Quan, and J. Fang. *Shape-Control and Electrocatalytic Activity-Enhancement of Pt-Based Bimetallic Nanocrystals.* Accounts of Chemical Research, **46**(8):1867–1877, 2013. doi:10.1021/ar3002238.

[79] V. R. Stamenkovic, N. M. Markovic. *Oxygen reduction on platinum bimetallic alloy catalysts.* In: *Handbook of Fuel Cells.* John Wiley & Sons, Ltd., 2010. doi:10.1002/9780470974001.f500002.

[80] Z. Shi and N. Lin. *Self-Assembly of a Two-Dimensional Bimetallic Coordination Framework and Dynamic Control of Reversible Conversions to*

Homo-Metallic Hydrogen-Bond Arrays. ChemPhysChem, **11**(1):97–100, 2010. doi:10.1002/cphc.200900756.

[81] J. I. Urgel, D. Ecija, W. Auwärter, D. Stassen, D. Bonifazi, and J. V. Barth. *Orthogonal Insertion of Lanthanide and Transition-Metal Atoms in Metal–Organic Networks on Surfaces*. Angewandte Chemie International Edition, **54**(21):6163–6167, 2015. doi:10.1002/anie.201410802.

[82] G. Binnig, H. Rohrer, C. Gerber, and E. Weibel. *Tunneling through a controllable vacuum gap*. Applied Physics Letters, **40**(2):178–180, 1982. doi:10.1063/1.92999.

[83] G. Binnig, H. Rohrer, C. Gerber, and E. Weibel. *Surface Studies by Scanning Tunneling Microscopy*. Physical Review Letters, **49**(1):57–61, 1982. doi:10.1103/PhysRevLett.49.57.

[84] G. Binnig, C. F. Quate, and C. Gerber. *Atomic Force Microscope*. Phys. Rev. Lett., **56**:930–933, Mar 1986. doi:10.1103/PhysRevLett.56.930.

[85] U. Dürig, D. W. Pohl, and F. Rohner. *Near-field optical-scanning microscopy*. Journal of Applied Physics, **59**(10):3318–3327, 1986. doi:http://dx.doi.org/10.1063/1.336848.

[86] H. K. Wickramasinghe. *Scanning probe microscopy: Current status and future trends*. Journal of Vacuum Science & Technology A, **8**(1):363–368, 1990. doi:http://dx.doi.org/10.1116/1.576397.

[87] J. A. Stroscio and W. J. Kaiser. *Scanning Tunneling Microscopy*. Academic Press, Inc., San Diego, 2nd edition, 1993.

[88] J. Tersoff and D. R. Hamann. *Theory and Application for the Scanning Tunneling Microscope*. Physical Review Letters, **50**(25):1998–2001, 1983. doi:10.1103/PhysRevLett.50.1998.

[89] J. Tersoff and D. R. Hamann. *Theory of the scanning tunneling microscope*. Physical Review B, **31**(2):805–813, 1985. doi:10.1103/PhysRevB.31.805.

[90] J. Bardeen. *Tunnelling from a Many-Particle Point of View*. Physical Review Letters, **6**(2):57–59, 1961. doi:10.1103/PhysRevLett.6.57.

[91] A. Selloni, P. Carnevali, E. Tosatti, and C. D. Chen. *Voltage-dependent scanning-tunneling microscopy of a crystal surface: Graphite.* Physical Review B, **31**(4):2602–2605, 1985. doi:10.1103/PhysRevB.31.2602.

[92] N. D. Lang. *Spectroscopy of single atoms in the scanning tunneling microscope.* Physical Review B, **34**(8):5947–5950, 1986. doi:10.1103/PhysRevB.34.5947.

[93] A. Volta. *On the Electricity Excited by the Mere Contact of Conducting Substances of Different Kinds. In a Letter from Mr. Alexander Volta, F. R. S. Professor of Natural Philosophy in the University of Pavia, to the Rt. Hon. Sir Joseph Banks, Bart. K. B. P. R. S.* Philosophical Transactions of the Royal Society of London, **90**:403–431, 1800. doi:10.1098/rstl.1800.0018.

[94] L. Galvani. *De Viribus Electricitatis in Motu Muscolari Commentarius.* Ex Typographia Instituti Scientiarium, Bononiae, 1791. archive.org/details/AloysiiGalvaniD00Galv.

[95] W. Schmickler and E. Santos. *Interfacial Electrochemistry.* Springer, Berlin Heidelberg, 2nd edition, 2010. doi:10.1007/978-3-642-04937-8.

[96] A. J. Bard and L. R. Faulkner. *Electrochemical Methods: Fundamentals and Applications.* John Wiley & Sons, Inc., New York, 2nd edition, 2001.

[97] D. M. Kolb. *Electrochemical Surface Science.* Angewandte Chemie International Edition, **40**(7):1162–1181, 2001. doi:10.1002/1521-3773(20010401)40:7<1162::AID-ANIE1162>3.0.CO;2-F.

[98] N. Marković and P. R. Jr. *Surface science studies of model fuel cell electrocatalysts.* Surface Science Reports, **45**(4–6):117–229, 2002. doi:10.1016/S0167-5729(01)00022-X.

[99] H. E. Hoster and H. A. Gasteiger. *Ex-situ surface preparation and analysis: transfer between UHV and electrochemical Cell.* In: *Handbook of Fuel Cells – Fundamentals, Technology and Applications.* Volume 2, Part 3, pp 236—265, John Wiley & Sons, Ltd, Chichester, 2003.

[100] F. Reniers. *The development of a transfer mechanism between UHV and electrochemistry environments.* Journal of Physics D: Applied Physics, **35**(21):R169, 2002. doi:10.1088/0022-3727/35/21/201.

[101] F. Reniers. *The development of a transfer mechanism between UHV and electrochemistry environments.* Journal of Physics D: Applied Physics, **35**(21):R169, 2002. doi:10.1088/0022-3727/35/21/201.

[102] G. Attard, R. Price, and A. Al-Akl. *Palladium adsorption on Pt(111): a combined electrochemical and ultra-high vacuum study.* Electrochimica Acta, **39**(11–12):1525–1530, 1994. doi:10.1016/0013-4686(94)85130-1.

[103] H. Hoster, T. Iwasita, H. Baumgärtner, and W. Vielstich. *Current-Time Behavior of Smooth and Porous PtRu Surfaces for Methanol Oxidation.* Journal of The Electrochemical Society, **148**(5):A496–A501, 2001. doi:10.1149/1.1365142.

[104] F. Reniers, V. Rooryck, S. Pace, and C. Buess-Herman. *UHV–liquid cell transfer system for Auger electron spectroscopy on electrodes.* Surface and Interface Analysis, **34**(1):623–627, 2002. doi:10.1002/sia.1374.

[105] C. Wöll, S. Chiang, R. J. Wilson, and P. H. Lippel. *Determination of atom positions at stacking-fault dislocations on Au(111) by scanning tunneling microscopy.* Physical Review B, **39**:7988–7991, Apr 1989. doi:10.1103/PhysRevB.39.7988.

[106] J. V. Barth, H. Brune, G. Ertl, and R. J. Behm. *Scanning tunneling microscopy observations on the reconstructed Au(111) surface: Atomic structure, long-range superstructure, rotational domains, and surface defects.* Physical Review B, **42**:9307–9318, Nov 1990. doi:10.1103/PhysRevB.42.9307.

[107] A. Hamelin. *Cyclic voltammetry at gold single-crystal surfaces. Part 1. Behaviour at low-index faces.* Journal of Electroanalytical Chemistry, **407**(1–2):1–11, 1996. doi:10.1016/0022-0728(95)04499-X.

[108] B. Han, Z. Li, C. Li, I. Pobelov, G. Su, R. Aguilar-Sanchez and T. Wandlowski. *From Self-Assembly to Charge Transport with Single Molecules — An Electrochemical Approach.* In: *Templates in Chemistry III.* Topics in Current Chemistry **287**:181–255, 2009. doi:10.1007/128_2008_152.

[109] P. Nordlund and H. Eklund. *Di-iron–carboxylate proteins.* Current Opinion in Structural Biology, **5**(6):758–766, 1995. doi:10.1016/0959-440X(95)80008-5.

[110] M. Lackinger, S. Griessl, W. M. Heckl, M. Hietschold, and G. W. Flynn. *Self-Assembly of Trimesic Acid at the Liquid-Solid Interface – a Study of Solvent-Induced Polymorphism*. Langmuir, **21**(11):4984–4988, 2005. doi:10.1021/la0467640.

[111] Z. Li, B. Han, L. J. Wan, and T. Wandlowski. *Supramolecular Nanostructures of 1,3,5-Benzene-tricarboxylic Acid at Electrified Au(111)/0.05 M H_2SO_4 Interfaces: An in Situ Scanning Tunneling Microscopy Study*. Langmuir, **21**(15):6915–6928, 2005. doi:10.1021/la0507737.

[112] N. Lin, A. Dmitriev, J. Weckesser, J. V. Barth, and K. Kern. *Real-Time Single-Molecule Imaging of the Formation and Dynamics of Coordination Compounds*. Angewandte Chemie International Edition, **41**(24):4779–4783, 2002. doi:10.1002/anie.200290046.

[113] D. Payer, A. Comisso, A. Dmitriev, T. Strunskus, N. Lin, C. Wöll, A. DeVita, J. Barth, and K. Kern. *Ionic Hydrogen Bonds Controlling Two-Dimensional Supramolecular Systems at a Metal Surface*. Chemistry – A European Journal, **13**(14):3900–3906, 2007. doi:10.1002/chem.200601325.

[114] Y. Ye, W. Sun, Y. Wang, X. Shao, X. Xu, F. Cheng, J. Li, and K. Wu. *A Unified Model: Self-Assembly of Trimesic Acid on Gold*. The Journal of Physical Chemistry C, **111**(28):10138–10141, 2007. doi:10.1021/jp072726o.

[115] N. Lin, D. Payer, A. Dmitriev, T. Strunskus, C. Wöll, J. V. Barth, and K. Kern. *Two-Dimensional Adatom Gas Bestowing Dynamic Heterogeneity on Surfaces*. Angewandte Chemie International Edition, **44**(10):1488–1491, 2005. doi:10.1002/anie.200461390.

[116] T. Classen, G. Fratesi, G. Costantini, S. Fabris, F. L. Stadler, C. Kim, S. de Gironcoli, S. Baroni, and K. Kern. *Templated Growth of Metal–Organic Coordination Chains at Surfaces*. Angewandte Chemie International Edition, **44**(38):6142–6145, 2005. URL: http://dx.doi.org/10.1002/anie.200502007, doi:10.1002/anie.200502007.

[117] J. Kim and A. A. Gewirth. *Mechanism of Oxygen Electroreduction on Gold Surfaces in Basic Media*. The Journal of Physical Chemistry B, **110**(6):2565–2571, 2006. doi:10.1021/jp0549529.

[118] M. H. Shao and R. R. Adzic. *Spectroscopic Identification of the Reaction Intermediates in Oxygen Reduction on Gold in Alkaline Solutions.* The Journal of Physical Chemistry B, **109**(35):16563–16566, 2005. doi:10.1021/jp053450s.

[119] A. G. Orive, A. H. Creus, D. Grumelli, G. A. Benitez, L. Andrini, F. G. Requejo, C. Bonazzola, and R. C. Salvarezza. *Oxygen Reduction on Iron-Melanin Granular Surfaces.* The Journal of Physical Chemistry C, **113**(39):17097–17103, 2009. doi:10.1021/jp905560d.

[120] R. Miah and T. Ohsaka. *Two-Step Four-Electron Reduction of Molecular Oxygen at Iodine-Adatoms-Modified Gold Electrode in Alkaline Media.* International Journal of Electrochemical Science, **7**:697–710, 2012.

[121] G. Wu, K. L. More, C. M. Johnston, and P. Zelenay. *High-Performance Electrocatalysts for Oxygen Reduction Derived from Polyaniline, Iron, and Cobalt.* Science, **332**(6028):443–447, 2011. doi:10.1126/science.1200832.

[122] A. B. Anderson and R. A. Sidik. *Oxygen Electroreduction on Fe^{II} and Fe^{III} Coordinated to N_4 Chelates. Reversible Potentials for the Intermediate Steps from Quantum Theory.* The Journal of Physical Chemistry B, **108**(16):5031–5035, 2004. doi:10.1021/jp037184z.

[123] C. T. Carver, B. D. Matson, and J. M. Mayer. *Electrocatalytic Oxygen Reduction by Iron Tetra-arylporphyrins Bearing Pendant Proton Relays.* Journal of the American Chemical Society, **134**(12):5444–5447, 2012. doi:10.1021/ja211987f.

[124] S. L. Tait, Y. Wang, G. Costantini, N. Lin, A. Baraldi, F. Esch, L. Petaccia, S. Lizzit, and K. Kern. *Metal-Organic Coordination Interactions in Fe-Terephthalic Acid Networks on Cu(100).* Journal of the American Chemical Society, **130**(6):2108–2113, 2008. doi:10.1021/ja0778186.

[125] F. Cheng and J. Chen. *Metal-air batteries: from oxygen reduction electrochemistry to cathode catalysts.* Chem. Soc. Rev., **41**:2172–2192, 2012. doi:10.1039/C1CS15228A.

[126] J. Guo, H. He, D. Chu, and R. Chen. *OH^--Binding Effects on Metallophthalocyanine Catalysts for O2 Reduction Reaction in Anion Exchange Membrane Fuel Cells.* Electrocatalysis, **3**(3-4):252–264, 2012. doi:10.1007/s12678-012-0106-1.

[127] I. F. Torrente, K. J. Franke, and J. I. Pascual. *Structure and electronic configuration of tetracyanoquinodimethane layers on a Au(111) surface.* International Journal of Mass Spectrometry, **277**(1—3):269–273, 2008. doi:10.1016/j.ijms.2008.07.013.

[128] E. B. Vickers, I. D. Giles, and J. S. Miller. *M[TCNQ]y-Based Magnets (M = Mn, Fe, Co, Ni; TCNQ = 7,7,8,8-tetracyano-p-quinodimethane).* Chemistry of Materials, **17**(7):1667–1672, 2005. doi:10.1021/cm047869r.

[129] E. J. Schelter, F. Karadas, C. Avendano, A. V. Prosvirin, W. Wernsdorfer, and K. R. Dunbar. *A Family of Mixed-Metal Cyanide Cubes with Alternating Octahedral and Tetrahedral Corners Exhibiting a Variety of Magnetic Behaviors Including Single Molecule Magnetism.* Journal of the American Chemical Society, **129**(26):8139–8149, 2007. doi:10.1021/ja0683281.

[130] R. Clérac, S. O'Kane, J. Cowen, X. Ouyang, R. Heintz, H. Zhao, M. J. Bazile, and K. R. Dunbar. *Glassy Magnets Composed of Metals Coordinated to 7,7,8,8-tetracyanoquinodimethane: M(TCNQ)2 (M = Mn, Fe, Co, Ni).* Chemistry of Materials, **15**(9):1840–1850, 2003. doi:10.1021/cm021053d.

[131] T.-C. Tseng, C. Lin, X. Shi, S. L. Tait, X. Liu, U. Starke, N. Lin, R. Zhang, C. Minot, M. A. Van Hove, J. I. Cerdá, and K. Kern. *Two-dimensional metal-organic coordination networks of mn-7,7,8,8-tetracyanoquinodimethane assembled on cu(100): Structural, electronic, and magnetic properties.* Phys. Rev. B, **80**:155458, Oct 2009. doi:10.1103/PhysRevB.80.155458.

[132] T.-C. Tseng, N. Abdurakhmanova, S. Stepanow, and K. Kern. *Hierarchical Assembly and Reticulation of Two-Dimensional Mn- and Ni-TCNQx (x = 1, 2, 4) Coordination Structures on a Metal Surface.* The Journal of Physical Chemistry C, **115**(20):10211–10217, 2011. doi:10.1021/jp2033643.

[133] N. Abdurakhmanova, T.-C. Tseng, A. Langner, C. S. Kley, V. Sessi, S. Stepanow, and K. Kern. *Superexchange-Mediated Ferromagnetic Coupling in Two-Dimensional Ni-TCNQ Networks on Metal Surfaces.* Phys. Rev. Lett., **110**:027202, Jan 2013. doi:10.1103/PhysRevLett.110.027202.

[134] D. A. Proshlyakov, M. A. Pressler, C. DeMaso, J. F. Leykam, D. L. DeWitt, and G. T. Babcock. *Oxygen Activation and Reduction in Respiration: Involvement of Redox-Active Tyrosine 244.* Science, **290**(5496):1588–1591, 2000. doi:10.1126/science.290.5496.1588.

[135] S. L. Tait, A. Langner, N. Lin, R. Chandrasekar, O. Fuhr, M. Ruben, and K. Kern. *Assembling Isostructural Metal-Organic Coordination Architectures on Cu(100), Ag(100) and Ag(111) Substrates.* ChemPhysChem, **9**(17):2495–2499, 2008. doi:10.1002/cphc.200800575.

[136] X. Lu and K. W. Hipps. *Scanning Tunneling Microscopy of Metal Phthalocyanines: d6 and d8 Cases.* The Journal of Physical Chemistry B, **101**(27):5391–5396, 1997. doi:10.1021/jp9707448.

[137] Z. H. Cheng, L. Gao, Z. T. Deng, Q. Liu, N. Jiang, X. Lin, X. B. He, S. X. Du, and H.-J. Gao. *Epitaxial Growth of Iron Phthalocyanine at the Initial Stage on Au(111) Surface.* The Journal of Physical Chemistry C, **111**(6):2656–2660, 2007. doi:10.1021/jp0660738.

[138] Z. H. Cheng, L. Gao, Z. T. Deng, N. Jiang, Q. Liu, D. X. Shi, S. X. Du, H. M. Guo, and H.-J. Gao. *Adsorption Behavior of Iron Phthalocyanine on Au(111) Surface at Submonolayer Coverage.* The Journal of Physical Chemistry C, **111**(26):9240–9244, 2007. doi:10.1021/jp070388l.

[139] F. V. D. Brink, W. Visscher, and E. Barendrecht. *Electrocatalysis of cathodic oxygen reduction by metal phthalocyanines: Part III. Iron phthalocyanine as electrocatalyst: experimental part.* Journal of Electroanalytical Chemistry and Interfacial Electrochemistry, **172**(1–2):301–325, 1984. doi:10.1016/0022-0728(84)80194-1.

[140] P. Vasudevan, Santosh, N. Mann, and S. Tyagi. *Transition metal complexes of porphyrins and phthalocyanines as electrocatalysts for dioxygen reduction.* Transition Metal Chemistry, **15**(2):81–90, 1990. doi:10.1007/BF01023892.

[141] A. Morozan, S. Campidelli, A. Filoramo, B. Jousselme, and S. Palacin. *Catalytic activity of cobalt and iron phthalocyanines or porphyrins supported on different carbon nanotubes towards oxygen reduction reaction.* Carbon, **49**(14):4839–4847, 2011. doi:10.1016/j.carbon.2011.07.004.

[142] R. Chen, H. Li, D. Chu, and G. Wang. *Unraveling Oxygen Reduction Reaction Mechanisms on Carbon-Supported Fe-Phthalocyanine and Co-Phthalocyanine Catalysts in Alkaline Solutions.* The Journal of Physical Chemistry C, **113**(48):20689–20697, 2009. doi:10.1021/jp906408y.

[143] J. H. Zagal. *Metallophthalocyanines as catalysts in electrochemical reactions.* Coordination Chemistry Reviews, **119**(0):89–136, 1992. doi:10.1016/0010-8545(92)80031-L.

[144] J. H. Zagal, S. Griveau, J. F. Silva, T. Nyokong, and F. Bedioui. *Metallophthalocyanine-based molecular materials as catalysts for electrochemical reactions.* Coordination Chemistry Reviews, **254**(23–24):2755–2791, 2010. doi:10.1016/j.ccr.2010.05.001.

[145] F. Charreteur, F. Jaouen, S. Ruggeri, and J.-P. Dodelet. *Fe/N/C non-precious catalysts for PEM fuel cells: Influence of the structural parameters of pristine commercial carbon blacks on their activity for oxygen reduction.* Electrochimica Acta, **53**(6):2925–2938, 2008. doi:10.1016/j.electacta.2007.11.002.

[146] N. Ramaswamy, U. Tylus, Q. Jia, and S. Mukerjee. *Activity Descriptor Identification for Oxygen Reduction on Nonprecious Electrocatalysts: Linking Surface Science to Coordination Chemistry.* Journal of the American Chemical Society, **135**(41):15443–15449, 2013. doi:10.1021/ja405149m.

[147] G. L. Miessler and D. A. Tarr. *Inorganic Chemistry.* Prentice Hall, 3rd edition, 2003.

[148] B. E. Murphy, S. A. Krasnikov, N. N. Sergeeva, A. A. Cafolla, A. B. Preobrajenski, A. N. Chaika, O. Lübben, and I. V. Shvets. *Homolytic Cleavage of Molecular Oxygen by Manganese Porphyrins Supported on Ag(111).* ACS Nano, **8**(5):5190–5198, 2014. doi:10.1021/nn501240j.

[149] W. Auwärter, A. Weber-Bargioni, A. Riemann, A. Schiffrin, O. Gröning, R. Fasel, and J. V. Barth. *Self-assembly and conformation of tetrapyridyl-porphyrin molecules on Ag(111).* The Journal of Chemical Physics, **124**(19):194708, 2006. doi:10.1063/1.2194541.

[150] W. Auwärter, A. Weber-Bargioni, S. Brink, A. Riemann, A. Schiffrin, M. Ruben, and J. V. Barth. *Controlled metalation of self-assembled porphyrin nanoarrays in two dimensions.* ChemPhysChem, **8**(2):250–254, 2007. doi:10.1002/cphc.200600675.

[151] L. Scudiero, D. E. Barlow, and K. W. Hipps. *Physical Properties and Metal Ion Specific Scanning Tunneling Microscopy Images of Metal(II) Tetraphenylpor-*

phyrins Deposited from Vapor onto Gold (111). The Journal of Physical Chemistry B, **104**(50):11899–11905, 2000. doi:10.1021/jp002292w.

[152] X. Lu and K. W. Hipps. *Scanning Tunneling Microscopy of Metal Phthalocyanines: d6 and d8 Cases.* The Journal of Physical Chemistry B, **101**(27):5391–5396, 1997. doi:10.1021/jp9707448.

[153] X. Lu, K. W. Hipps, X. D. Wang, and U. Mazur. *Scanning Tunneling Microscopy of Metal Phthalocyanines: d7 and d9 Cases.* Journal of the American Chemical Society, **118**(30):7197–7202, 1996. doi:10.1021/ja960874e.

[154] S. Prabhulkar, H. Tian, X. Wang, J.-J. Zhu, and C.-Z. Li. *Engineered Proteins: Redox Properties and Their Applications.* Antioxidants & Redox Signaling, **17**(12):1796–1822, 2012. doi:10.1089/ars.2011.4001.

[155] X.-J. Su, M. Gao, L. Jiao, R.-Z. Liao, P. E. M. Siegbahn, J.-P. Cheng, and M.-T. Zhang. *Electrocatalytic Water Oxidation by a Dinuclear Copper Complex in a Neutral Aqueous Solution.* Angewandte Chemie, **127**(16):4991–4996, 2015. doi:10.1002/ange.201411625.

[156] S. Yoshimoto, J. Inukai, A. Tada, T. Abe, T. Morimoto, A. Osuka, H. Furuta, and K. Itaya. *Adlayer Structure of and Electrochemical O_2 Reduction on Cobalt Porphine-Modified and Cobalt Octaethylporphyrin-Modified Au(111) in $HClO_4$.* The Journal of Physical Chemistry B, **108**(6):1948–1954, 2004. doi:10.1021/jp0366421.

[157] S.-I. Yamazaki, Y. Yamada, T. Ioroi, N. Fujiwara, Z. Siroma, K. Yasuda, and Y. Miyazaki. *Estimation of specific interaction between several Co porphyrins and carbon black: its influence on the electrocatalytic O_2 reduction by the porphyrins.* Journal of Electroanalytical Chemistry, **576**(2):253 – 259, 2005. doi:10.1016/j.jelechem.2004.10.022.

[158] A. Choi, H. Jeong, S. Kim, S. Jo, and S. Jeon. *Electrocatalytic reduction of dioxygen by cobalt porphyrin-modified glassy carbon electrode with single-walled carbon nanotubes and nafion in aqueous solutions.* Electrochimica Acta, **53**(5):2579–2584, 2008. doi:10.1016/j.electacta.2007.10.029.

[159] A. Morozan, S. Campidelli, A. Filoramo, B. Jousselme, and S. Palacin. *Catalytic activity of cobalt and iron phthalocyanines or porphyrins supported on different*

carbon nanotubes towards oxygen reduction reaction. Carbon, **49**(14):4839–4847, 2011. doi:10.1016/j.carbon.2011.07.004.

[160] A. Marín V., M. J. Aguirre, J. Muena, W. Dehaen, W. Maes, T. H. Ngo, G. Ramírez, and M. C. Arévalo. *Electro-reduction of Oxygen to Water Mediated by Stable Glassy Carbon Electrodes Modified by Co(II)-porphyrins with Voluminous Meso-Substituent.* International Journal of Electrochemical Science, **10**:3949–3960, 2015.

[161] C. Shi and F. C. Anson. *Catalytic pathways for the electroreduction of oxygen by iron tetrakis(4-N-methylpyridyl)porphyrin or iron tetraphenylporphyrin adsorbed on edge plane pyrolytic graphite electrodes.* Inorganic Chemistry, **29**(21):4298–4305, 1990. doi:10.1021/ic00346a027.

[162] B. D. Matson, C. T. Carver, A. Von Ruden, J. Y. Yang, S. Raugei, and J. M. Mayer. *Distant protonated pyridine groups in water-soluble iron porphyrin electrocatalysts promote selective oxygen reduction to water.* Chemical Communications, **48**:11100–11102, 2012. doi:10.1039/C2CC35576K.

[163] Q. He, T. Mugadza, X. Kang, X. Zhu, S. Chen, J. Kerr, and T. Nyokong. *Molecular catalysis of the oxygen reduction reaction by iron porphyrin catalysts tethered into Nafion layers: An electrochemical study in solution and a membrane-electrode-assembly study in fuel cells.* Journal of Power Sources, **216**(0):67–75, 2012. doi:10.1016/j.jpowsour.2012.05.043.

[164] F. C. Anson, C. Shi, and B. Steiger. *Novel Multinuclear Catalysts for the Electroreduction of Dioxygen Directly to Water.* Accounts of Chemical Research, **30**(11):437–444, 1997. doi:10.1021/ar960264j.

[165] H. E. Toma and K. Araki. *Supramolecular assemblies of ruthenium complexes and porphyrins.* Coordination Chemistry Reviews, **196**(1):307–329, 2000. doi:10.1016/S0010-8545(99)00041-7.

[166] H. Winnischofer, V. Y. Otake, S. Dovidauskas, M. Nakamura, H. E. Toma, and K. Araki. *Supramolecular tetracluster-cobalt porphyrin: a four-electron transfer catalyst for dioxygen reduction.* Electrochimica Acta, **49**(22–23):3711–3718, 2004. doi:http://dx.doi.org/10.1016/j.electacta.2003.12.052.

[167] S. Swavey and D. Fresh. *Enhanced Electrocatalytic Reduction of Oxygen at Electrodes Coated with a Multi-Metallic Co(II)/Pt(II) Porphyrin.* American Journal of Analytical Chemistry, **4**:54–59, 2013. doi:10.4236/ajac.2013.410A1007.

[168] J. Maruyama, C. Baier, H. Wolfschmidt, P. Bele, and U. Stimming. *Enhancement of oxygen reduction at Fe tetrapyridyl porphyrin by pyridyl-N coordination to transition metal ions.* Electrochimica Acta, **63**:16–21, 2012. doi:10.1016/j.electacta.2011.12.017.

[169] W. Hieringer, K. Flechtner, A. Kretschmann, K. Seufert, W. Auwärter, J. V. Barth, A. Görling, H.-P. Steinrück, and J. M. Gottfried. *The Surface Trans Effect: Influence of Axial Ligands on the Surface Chemical Bonds of Adsorbed Metalloporphyrins.* Journal of the American Chemical Society, **133**(16):6206–6222, 2011. doi:10.1021/ja1093502.

[170] K. D. Wael and A. Adriaens. *Comparison between the electrocatalytic properties of different metal ion phthalocyanines and porphyrins towards the oxidation of hydroxide.* Talanta, **74**(5):1562–1567, 2008. doi:10.1016/j.talanta.2007.09.034.

[171] N. Ito, S. E. V. Phillips, C. Stevens, Z. B. Ogel, M. J. McPherson, J. N. Keen, K. D. S. Yadav, and P. F. Knowles. *Novel thioether bond revealed by a 1.7 Å crystal structure of galactose oxidase.* Nature, **350**:87–90, 1991. doi:dx.doi.org/10.1038/350087a0.

[172] N. Ito, S. E. Phillips, K. D. Yadav, and P. F. Knowles. *Crystal Structure of a Free Radical Enzyme, Galactose Oxidase.* Journal of Molecular Biology, **238**(5):704–814, 1994. doi:10.1006/jmbi.1994.1335.

[173] Y. Wang, J. L. DuBois, B. Hedman, K. O. Hodgson, and T. D. P. Stack. *Catalytic Galactose Oxidase Models: Biomimetic Cu(II)-Phenoxyl-Radical Reactivity.* Science, **279**(5350):537–540, 1998. doi:10.1126/science.279.5350.537.

[174] J. Müller, T. Weyhermüller, E. Bill, P. Hildebrandt, L. Ould-Moussa, T. Glaser, and K. Wieghardt. *Why Does the Active Form of Galactose Oxidase Possess a Diamagnetic Ground State?* Angewandte Chemie International Edition, **37**(5):616–619, 1998. doi:10.1002/(SICI)1521-3773(19980316)37:5<616::AID-ANIE616>3.0.CO;2-4.

[175] J. W. Whittaker. *Free radical catalysis by galactose oxidase.* Chemical Reviews, **103**(6):2347–2364, 2003. doi:10.1021/cr020425z.

[176] P. M. Vignais and B. Billoud. *Occurrence, Classification, and Biological Function of Hydrogenases: An Overview.* Chemical Reviews, **107**(10):4206–4272, 2007. doi:10.1021/cr050196r.

[177] J. C. Fontecilla-Camps, A. Volbeda, C. Cavazza, and Y. Nicolet. *Structure/Function Relationships of [NiFe]- and [FeFe]-Hydrogenases.* Chemical Reviews, **107**(10):4273–4303, 2007. doi:10.1021/cr050195z.

[178] C. Mealli and T. Rauchfuss. *Models for the Hydrogenases Put the Focus Where It Should Be—Hydrogen.* Angewandte Chemie International Edition, **46**(47):8942–8944, 2007. doi:10.1002/anie.200703413.

[179] F. Gloaguen and T. B. Rauchfuss. *Small molecule mimics of hydrogenases: hydrides and redox.* Chem. Soc. Rev., **38**:100–108, 2009. doi:10.1039/B801796B.

[180] C. Tard and C. J. Pickett. *Structural and Functional Analogues of the Active Sites of the [Fe]-, [NiFe]-, and [FeFe]-Hydrogenases.* Chemical Reviews, **109**(6):2245–2274, 2009. doi:10.1021/cr800542q.

[181] G. Di Santo, S. Blankenburg, C. Castellarin-Cudia, M. Fanetti, P. Borghetti, L. Sangaletti, L. Floreano, A. Verdini, E. Magnano, F. Bondino, C. A. Pignedoli, M.-T. Nguyen, R. Gaspari, D. Passerone, and A. Goldoni. *Supramolecular Engineering through Temperature-Induced Chemical Modification of 2H-Tetraphenylporphyrin on Ag(111): Flat Phenyl Conformation and Possible Dehydrogenation Reactions.* Chemistry – A European Journal, **17**(51):14354–14359, 2011. doi:10.1002/chem.201102268.

[182] M. Röckert, M. Franke, Q. Tariq, D. Lungerich, N. Jux, M. Stark, A. Kaftan, S. Ditze, H. Marbach, M. Laurin, J. Libuda, H.-P. Steinrück, and O. Lytken. *Insights in Reaction Mechanistics: Isotopic Exchange during the Metalation of Deuterated Tetraphenyl-21,23D-porphyrin on Cu(111).* The Journal of Physical Chemistry C, **118**(46):26729–26736, 2014. doi:10.1021/jp507303h.

Acknowledgments

Many people contributed on different ways to the success of this thesis. I would like to express my gratitude to...

Prof. Klaus Kern, my thesis director, for giving me the opportunity to work in his research group on such an interesting field in nanoscience.

Prof. Michael Grätzel, PD Peter Broekmann and PD Markus Lackinger for agreeing to be in my thesis jury.

Dr. Sebastian Stepanow and Dr. Rico Gutzler, my supervisors, for giving me so much freedom and at the same time providing continuous support and guidance.

A special *gracias* goes to Dr. Doris Grumelli who has accompanied me from the beginning. Your enthusiasm for science and your optimism are really inspiring. Thanks for all the long discussions about "Why".

Dr. Nasiba White, Dr. Christopher Kley and Dr. Jan Cechal for introducing me into the world of scanning tunneling microscopy.

Dr. Sören Krotzky, Claudius Morchutti and Diana Hötger, the 6B15 crew, for the nice atmosphere in the lab.

Christian Dette and Carola Strasser, the co-founders of the *Kafferunde*, for their friendship.

Wolfgang Stiepany, Peter Andler and Marko Memmler, our technicians, for their great help to fix and improve the machine.

Many other people from our department and the institute for creating a nice atmosphere. Dr. Tobias Herden and Sabine Abb for baking many cakes. Members of the

lunch group who have not mentioned yet; Dr. Theresa Lutz, Dr. Gordon Rinke and Christoph Große. Dr. Eike Oliver Schäfer-Nolte for his postal service. Dr. Thomas White for proofreading this thesis. And many more...

Finally, I thank my parents and siblings for always being there for me. My biggest thank goes to my wife and my son for all their love. I thank Anna for encourage and motivate me throughout the last years. Without your support this would not have been possible. You complete me! Mein letztes Dankeschön geht an Amaru, der so viel in meinem Leben positiv verändert hat. Ich danke dir dafür, dass du mich immer aufmunterst und mich immer zum lächeln bringst.

Curriculum Vitae

Personal Information

Name:	Benjamin Wurster
Date of Birth:	December 20, 1985
Place of Birth:	Kassel, Germany
Nationality:	German

Education

2011 – 2015	**Doctoral Studies** Ecole Polytechnique Federale de Lausanne, Switzerland Doctoral School in Physics Max-Planck Institute for Solid State Research Stuttgart, Nanoscale Science Department, Prof. Dr. K. Kern
2010 – 2011	**Diploma Thesis** "*Zweidimensionale Adsorbatlagen schwefelfunktionalisierter Ferrocenderivate auf Goldoberflächen*" University of Kassel, Institute of Chemistry, Organometallic Chemistry, Prof. Dr. U. Siemeling
2006 – 2011	**Diploma Studies** University of Kassel, Germany Diploma in Nanostructure and Molecular Science
1996 – 2005	**Gymnasium (High School)** Wilhelmsgymnasium, Kassel, Germany

Publications

- Doris Grumelli, **Benjamin Wurster**, Sebastian Stepanow and Klaus Kern. "Bio-inspired nanocatalysts for the oxygen reduction reaction" Nature Communications, 4:2904, 2013.
- Doris Grumelli, **Benjamin Wurster**, Sebastian Stepanow, Rico Gutzler and Klaus Kern. "Ligand-controlled electrocatalytical response in the oxygen reduction reaction in iron-based 2D metal-organic structures"' *in preparation*
- **Benjamin Wurster**, Diana Hötger, Rico Gutzler, Doris Grumelli and Klaus Kern. "Driving the oxygen evolution reaction by nonlinear cooperativety in bimetallic coordination networks" *in preparation*

View publication stats